Alternative Platinum Electrocatalyst Designs for Improved Platinum Utilization

by

Brandy Kinkead

B.Sc., University of Manitoba, 2010

Thesis Submitted in Partial Fulfillment of the
Requirements for the Degree of
Doctor of Philosophy

in the
Department of Chemistry
Faculty of Science

SIMON FRASER UNIVERSITY

Fall 2014

Approval

Name:	**Brandy Kinkead**
Degree:	**Doctor of Philosophy**
Title:	***Alternative Platinum Electrocatalyst Designs for Improved Platinum Utilization***
Examining Committee:	**Chair:** Robert Britton Associate Professor

Byron Gates
Senior Supervisor
Associate Professor

Steven Holdcroft
Supervisor
Professor

Tim Storr
Supervisor
Associate Professor

Michael Eikerling
Internal Examiner
Professor

David Wilkinson
External Examiner
Professor
Department of Chemical Engineering
University of British Columbia

Date Defended/Approved: December 10, 2014

Partial Copyright Licence

The author, whose copyright is declared on the title page of this work, has granted to Simon Fraser University the non-exclusive, royalty-free right to include a digital copy of this thesis, project or extended essay[s] and associated supplemental files ("Work") (title[s] below) in Summit, the Institutional Research Repository at SFU. SFU may also make copies of the Work for purposes of a scholarly or research nature; for users of the SFU Library; or in response to a request from another library, or educational institution, on SFU's own behalf or for one of its users. Distribution may be in any form.

The author has further agreed that SFU may keep more than one copy of the Work for purposes of back-up and security; and that SFU may, without changing the content, translate, if technically possible, the Work to any medium or format for the purpose of preserving the Work and facilitating the exercise of SFU's rights under this licence.

It is understood that copying, publication, or public performance of the Work for commercial purposes shall not be allowed without the author's written permission.

While granting the above uses to SFU, the author retains copyright ownership and moral rights in the Work, and may deal with the copyright in the Work in any way consistent with the terms of this licence, including the right to change the Work for subsequent purposes, including editing and publishing the Work in whole or in part, and licensing the content to other parties as the author may desire.

The author represents and warrants that he/she has the right to grant the rights contained in this licence and that the Work does not, to the best of the author's knowledge, infringe upon anyone's copyright. The author has obtained written copyright permission, where required, for the use of any third-party copyrighted material contained in the Work. The author represents and warrants that the Work is his/her own original work and that he/she has not previously assigned or relinquished the rights conferred in this licence.

Simon Fraser University Library
Burnaby, British Columbia, Canada

revised Fall 2013

Abstract

Platinum electrocatalysts are important for a number of low and zero-emission energy technologies, including low temperature fuel cells. For reactions such as oxygen reduction at a fuel cell cathode, poor kinetics and harsh operating conditions (which lead to catalyst degradation) dictate the use of large volumes of Pt for efficient electrocatalysis. This need for a large quantity of Pt increases the cost of the fuel cell and makes the technology too expensive to compete with petroleum based energy alternatives typically used in automotive applications. Improving the effective utilization of Pt enables the same performance to be achieved with a smaller mass of Pt. A more effective use of Pt can be achieved through the use of alternative catalyst layer designs. The work presented in this thesis demonstrates three novel Pt catalyst layer designs with the aim of improving the effective utilization of Pt for electrocatalysis. These designs include pure Pt ordered porous electrodes (Pt-OP electrodes), supported Pt nanoparticle ordered porous electrodes (support@PtNP-OP electrodes) and nanobowl supported Pt NPs (support@PtNP nanobowls). These designs aim to enhance Pt utilization by improving: i) mass transport through the use of an open porous design; ii) Pt electrochemical stability via the use of stable materials throughout the electrocatalyst design and/or through support interactions; and iii) Pt catalytic activity via favorable interactions with support materials. The preparation of these new Pt electrocatalyst designs is presented through the use of sacrificial templates. The new materials were extensively characterized by electron microscopy, X-ray spectroscopy, and electrochemical methods. The alternative electrocatalyst designs demonstrated here provide new routes towards enhancing the utilization of Pt for electrocatalytic applications.

Keywords: Electrocatalysis; Platinum; Oxygen Reduction Reaction; Ordered Porous; Inverse Opal; 3DOM; Nanoparticle; Self-Assembly

I would like to dedicate this thesis to my best friend, editor, therapist, and husband Matt Pilapil, who has supported me throughout my undergraduate and graduate degree. Thank you for your everlasting support and patience.

Acknowledgements

I would like to thank my supervisor, Dr. Byron Gates, for giving me the opportunity to work with him for the past 5 years. I have truly appreciated your guidance and support.

I also thank Dr. Gregory Jerkiewicz, for his great help in performing and interpreting the electrochemical analyses in this thesis work.

I would also like to thank the many great people I have worked with, both at SFU and at Queen’s University. In addition to being colleagues, many of you have become great friends and our time talking at our desks, getting coffee or eating lunch together will not be forgotten.

I also thank my family, for their gracious love and support; my parents Cindy and Fairlie Kinkead; my sisters Jen Land and Charissa Todd; and my family in-law - Juliet, Ted, and Nicole Pilapil.

Table of Contents

List of Tables

List of Figures

List of Acronyms and Symbols

3D	Three Dimensional
1-BuOH	1-Butanol
A	Area
a.u.	Arbitrary Units
CCL	Cathodic Catalyst Layer
CE	Counter Electrode
cps	Counts Per Second
CV	Cyclic Voltammetry
DOE	Department of Energy
E_o	Thermodynamic Electrode Potential
EDS	Energy Dispersive X-ray Spectroscopy
EG	Ethylene Glycol
ECSA	Electrochemical Surface Area
EtOH	Ethanol
EM	Electron Microscopy
DCM	Dichloromethane
DL	Double Layer
DMF	Dimethylformamide
DFT	Density Functional Theory
FAAS	Flame Atomic Absorption Spectroscopy
FC	Fuel Cell
FTIR	Fourier Transform Infrared
FWHM	Full Width at Half Maximum
GDL	Gas Diffusion Layer
HAADF	High-Angle Annular Dark Field
ICP-MS	Inductively Coupled Plasma Mass Spectrometry
IR	Infrared
KL	Koutecky-Levich
LB	Langmuir Blodgett
MEA	Membrane Electrode Assembly
MeOH	Methanol

NP	Nanoparticle
NB	Nanobowl
OP	Ordered Porous
PEM	Proton Exchange Membrane
PS	Polystyrene
PS@NPs	Nanoparticles decorated polystyrene spheres
PVP	Poly(vinylpyrrolidone)
Q	Charge
q_{ad}	Charge associated with the adsorption/desorption of a known species onto the electrode surface per square area
q_m	Charge associated with adsorption/desorption of a known species onto the surface of an electrode of interest
RHE	Reversible Hydrogen Electrode
RE	Reference Electrode
RF	Roughness Factor
RT	Room Temperature
SEF	Surface Area Enhancement Factor
SEM	Scanning Electron Microscopy
SSA	Specific Surface Area
STEM	Scanning Transmission Electron Microscopy
support@PtNP	Pt Nanoparticle decorated support
TEM	Transmission Electron Microscopy
UV-Vis	Ultraviolet-Visible Spectrophotometer
WE	Working Electrode
XPS	X-ray Photoelectron Spectroscopy
XRD	X-ray Diffraction
α	Transfer Coefficient
η	Overpotential
ρ	Density
Φ	Work Function

Glossary

Agglomerate	An irreversible aggregate (nanoparticles within the aggregate are strongly bound to one another).
Aggregate	A cluster of nanoparticles.
Density Functional Theory	A quantum mechanical modeling method used to evaluate the quantum ground state energy of a many-body system.
Faradaic Process	The generation of current through interfacial charge-transfer resulting from an electrochemical reaction at an electrode surface.
Fuel Cell	A device which generate electricity from the controlled electrochemical reaction of an energy carrier gas (e.g., H_2) with oxygen.
Nanoparticle	Particles with at least one dimension between 1 and 100 nm.
Non-Faradaic Process	The generation of current due to the movement of charged species (e.g., ions) at the electrode-electrolyte interface.
Overpotential	Difference between the measured potential onset and the thermodynamic electrode potential for a particular electrochemical reaction.
Oxidation	A process that describes the loss of electrons or an increase in oxidation state of a molecule, atom, or ion.
Real or electrochemical surface area	The surface area of an electrode as measured by electrochemical methods. This value defines the area of the electrode that is accessible for electrochemical reactions, including contributions to surface area from roughness and porosity of the electrode.
Reduction	A process that describes the gain of electrons or a decrease in oxidation state of a molecule, atom, or ion.
Specific Surface Area	The ratio of real surface area to mass for a specified material
Thermodynamic Electrode Potential	The thermodynamically determined redox potential for a half-reaction of interest. This value is determined experimentally under standard conditions.

Chapter 1.

Introduction

1.1. Applications of Electrocatalysis

1.1.1. Overview

The importance of electrocatalytic materials has been highlighted in recent years due to our urgent need for alternative energy sources. Electrocatalytic materials are necessary for the implementation of a hydrogen economy, which utilizes hydrogen as an energy carrier for the conversion of renewable resources into electricity. In this hydrogen economy, electrocatalysts facilitate the electrochemical reactions that produce electrical power from hydrogen gas for applications that include automotive transportation and stationary power generation. Electrocatalysis can also be used to produce hydrogen; whereby a renewable energy source, generally water, is converted into hydrogen through electrolytic splitting. This technology is relatively well-developed and will not be discussed here in detail. The reverse process of transforming hydrogen into power using electrocatalysts within a fuel cell (FC) is by contrast under developed and is the focus of this thesis work.(Mark K Debe, 2012; Lavacchi, Miller, & Vizza, 2013c; Steele & Heinzel, 2001; Yuan & Wang, 2008)

Electricity is generated in a fuel cell through the electrochemical reaction of oxygen with an energy carrier. This method of energy generation produces less carbon emissions than petroleum combustion technology. In the case of H_2/O_2 FCs, hydrogen gas acts as an energy carrier, reacting with O_2 gas to produce electrical power. The only by-product of this reaction is water, making it an emissions-free energy source. Electrocatalysts in these FCs aim to increase the rate of this electrochemical reaction, by providing a low-energy path for the reaction to proceed. Increasing this rate also increases the potential power that can be generated by the FC. Energy carriers other than H_2 gas may also be used, including alcohols and formic acid. These carriers have the advantage of being easier to transport and store, but their use in fuel cells is less ideal due to the generation of carbon-containing emissions which are harmful to the environment.(Gregor, 2002; Lavacchi, Miller, & Vizza, 2013b; Lavacchi, et al., 2013c)

Three different FC designs can (theoretically) produce emissions-free energy from the reaction of H_2 and O_2 gas: Alkaline FCs; Solid Oxide FCs; and Proton Exchange Membrane (PEM) FCs. Solid oxide fuel cells operate at temperatures > 500°C, which limits their ability to be applied to automotive technologies. Both Alkaline and PEM FCs operate at relatively low temperatures (generally less than 100°C), making them more readily applicable for automotive applications. These FCs consist of 3 main components, a cathode, an anode and a polymer exchange membrane. Alkaline FC technology is currently limited by the development of an efficient and stable polymer exchange membrane. This thesis work focuses primarily on PEM FCs (Fig. 1.1) due to their: i) well-developed polymer exchange membrane; ii) low operating temperatures suitable for portable applications; iii) ability to use zero-emission fuels (H_2/O_2); and iv) limited commercialization due to issues pertaining to catalyst layer design.(Mark K Debe, 2012; Gregor, 2002; Lavacchi, et al., 2013b, 2013c; Nørskov et al., 2004; Shen, 2008; Yuan & Wang, 2008)

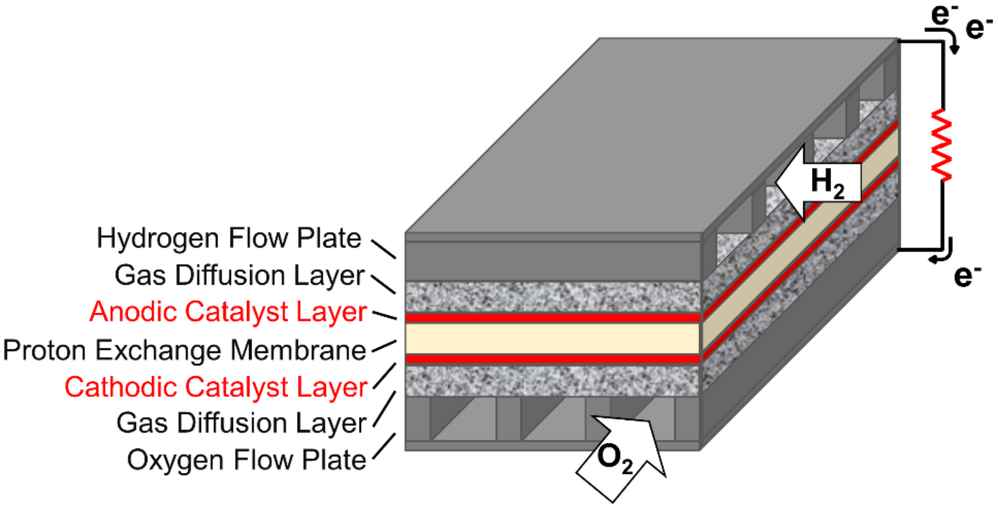

Figure 1.1 **Schematic of a proton exchange membrane fuel cell. The anode consists of the hydrogen flow plate, anodic catalyst layer and the gas diffusion layer between them. Similarly, the cathode consists of the oxygen flow plate, cathodic catalyst layer and the gas diffusion layer between them. The proton exchange membrane with the cathodic and anodic catalyst layers is referred to as a membrane electrode assembly (MEA).**

1.1.2. Proton Exchange Membrane Fuel Cells

A typical PEM FC consists of a number of components (Fig. 1.1), each vital to the controlled reaction of H_2 gas with O_2 gas to generate electrical energy. Hydrogen gas is supplied at the anode through a flow plate where it reacts at the anodic catalyst layer to produce protons (H^+) and electrons (e^-) (Eq. 1). Protons pass from the anode to the cathode via the proton exchange membrane. Electrons travel through the external circuit to the cathode, powering the attached load. Oxygen supplied at the cathode (through the cathodic flow plate) reacts with H^+ and e^- to produce water (Eq. 2), completing the overall reaction necessary to generate power (Eq. 3). For both the anode and cathode, the gas diffusion layer facilitates the diffusion of gas to the catalyst layer and conduction of electrons between the FC and the external circuit.(David, 2002; Debe, 2012; Lavacchi, et al., 2013c; Nørskov, et al., 2004; Shen, 2008; Song & Zhang, 2008; Yuan & Wang, 2008)

Anode, Hydrogen Oxidation Reaction (HOR): $H_2 \rightarrow 2H^+ + 2e^-$ (1)

$$\text{Cathode, Oxygen Reduction Reaction (ORR):} \quad 2H^{+} + 2\,e^{-} + \tfrac{1}{2}O_2 \rightarrow H_2O \qquad (2)$$

$$\text{Overall Fuel Cell Reaction:} \quad H_2 + \tfrac{1}{2}\,O_2 \rightarrow H_2O \qquad (3)$$

The low rate of the cathodic oxygen reduction reaction (ORR) relative to the hydrogen oxidation reaction (HOR) continues to be a major hurdle in commercializing PEM FC technology. The ORR is plagued by very sluggish kinetics, as defined by a low exchange current density (j_o). These poor kinetics result in a large reduction overpotential (η, difference between the thermodynamic and experimental reduction potential) associated with a large energy barrier in the reaction pathway. An electrocatalyst, similar to any other catalytic system, is sought to lower this energy barrier and to increase the rate of the electrochemical reaction. The anodic hydrogen oxidation reaction (HOR) has much faster kinetics (j_o for HOR is approximately 1 million times higher than for ORR) and a correspondingly lower overpotential.

At present, platinum is most commonly used to catalyze both the ORR and HOR in PEM FCs. A larger mass of Pt is required at the cathode than at the anode, so that the ORR can proceed at a fast enough rate to generate the electricity necessary to power an external load. This high mass of Pt drives up the cost of fuel cells and limits their commercialization. Much research has focused on improving the cathodic catalyst layer (CCL). This research is generally divided into two branches: i) finding an alternative, cheaper material to catalyze the ORR (e.g., metal oxides/nitrides); ii) developing catalyst layer designs that improve the effective utilization of Pt in order to minimize the mass of Pt required. Although both routes have merit for improving the economic viability of PEM FCs, the research described herein focuses on the latter. Research in the area of enhanced Pt utilization needs further assistance for improvement through understanding more about the fundamental utilization and distribution of Pt in fuel cells and through development of new catalyst designs, which build upon this knowledge.(David, 2002; Mark K Debe, 2012; Lavacchi, et al., 2013c; Nørskov, et al., 2004; Shen, 2008; C. Song & Zhang, 2008; Yuan & Wang, 2008)

1.2. Catalyst Layer Design Considerations

1.2.1. Mechanism of Oxygen Reduction Reaction on Platinum Catalysts

The thermodynamic potential of the ORR (Eq. 4) is positive, such that the reaction is thermodynamically favorable. The origin of the overpotential, therefore, is kinetic in nature. An understanding of the ORR mechanism is required to better understand the kinetic losses occurring during ORR and to appreciate the issues that plague the CCL. Oxygen reduction is a multi-electron reaction that can proceed through a number of routes and intermediates. The mechanism of this reaction depends, in part, on the surface upon which the catalytic reaction takes place. Properties of the surface that can impact the reaction route and/or rate include chemical composition, surface structure (e.g., faceting), and chemical environment.(Lavacchi, Miller, & Vizza, 2013a; Nørskov, et al., 2004; C. Song & Zhang, 2008) Since Pt-based catalysts are the focus of this thesis work, the mechanism of ORR on metal surfaces will be discussed in detail below.

$$O_2 + 4\,H^+ + 4\,e^- \rightarrow 2\,H_2O \quad (E_o = 1.23\text{ V vs. RHE}) \tag{4}$$

Oxygen reduction requires that protons and electrons combine with oxygen to produce water. On a Pt surface, this reaction is believed to take place via two different routes, the dissociative and associative mechanisms, depending on the applied overpotential (may occur in parallel in some overpotential regions).(Nørskov, et al., 2004) Equations 5 to 7 describe the steps for the dissociative mechanism; equations 8 to 12 describe the steps for the associate mechanism, where * denotes a surface site:

Dissociative:

$$\tfrac{1}{2}\,O_2 + * \rightarrow O^* \tag{5}$$

$$O^* + H^+ + e^- \rightarrow HO^* \tag{6}$$

$$HO^* + H^+ + e^- \rightarrow H_2O + * \tag{7}$$

Associative:

$$O_2 + * \rightarrow O_2^* \tag{8}$$

$$O_2^* + H^+ + e^- \rightarrow HO_2^* \tag{9}$$

$$HO_2^* + H^+ + e^- \rightarrow H_2O + O^* \tag{10}$$

$$O^* + H^+ + e^- \rightarrow HO^* \tag{11}$$

$$HO^* + H^+ + e^- \rightarrow H_2O + * \tag{12}$$

In both mechanisms, protons and electrons must transfer to adsorbed oxygen or hydroxide species, eventually producing water that dissociates from the surfaces. The stability of these oxygen containing adsorbed species, O*, HO* and HO_2*, is important in determining the rate of these proton and electron transfers. If the adsorbates are too stable, it will not be energetically favorable for the proton or electron transfer steps to proceed. If the species are not stable enough, then the lifetime of the adsorbed species will be short and limit the proton and electron transfer steps. This relation can be better understood through density functional theory (DFT) calculations. Using DFT, the energies of the O* surface intermediate as a function of the electrode potential of Pt was calculated. At zero cell potential, Pt was bound too strongly with O resulting in a higher energy barrier for the next step. This scenario corresponds to the reaction conditions for ORR on Pt surfaces in the absence of an applied potential. This reaction would proceed at only a very slow rate. To push this reaction forward, a potential is applied to the Pt surfaces. This applied potential alters the binding of O to the Pt surfaces, such that the reaction can now proceed at a considerable rate (overcome energy barrier).(Nørskov, et al., 2004)

The stability of the oxide and hydroxide species will vary depending on the surface on which they are bound, resulting in different overpotentials (and reaction rates) for different metals.(Marković, Schmidt, Stamenković, & Ross, 2001; Nørskov, et al., 2004; C. Song & Zhang, 2008; V. Stamenkovic et al., 2006). For example, Au binds so poorly with O that proton and electron transfers cannot occur during the short residence time. Plotting the energies of the O* surface intermediate versus the ORR activity for a number of different metal surfaces (as calculated by DFT at a defined surface coverage) can be used to visualize the relation between O adsorption energy and ORR reaction overpotential. These plots, referred to as volcano plots, have been generated for a series of different metal surfaces.(Nørskov, et al., 2004) and different Pt alloy surfaces.(V. Stamenkovic, et al., 2006). This plot highlights the importance of oxygen binding energy to the ORR.

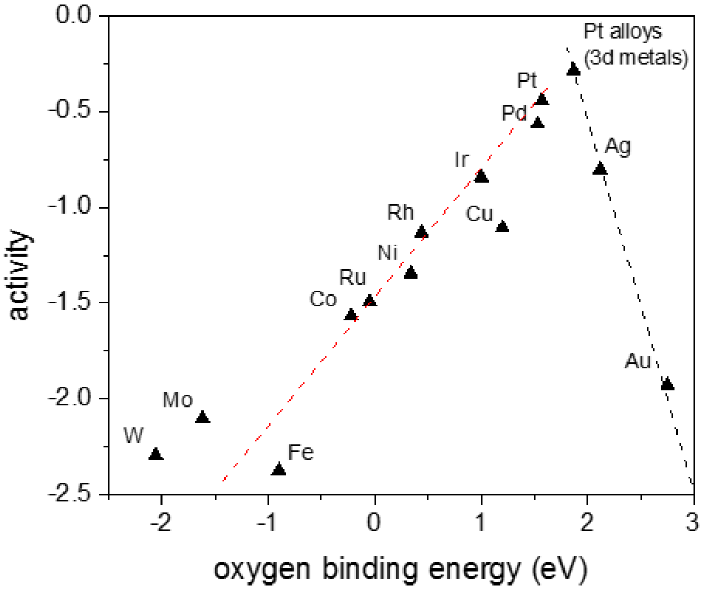

Figure 1.2 **Oxygen reduction reaction volcano plots. Activity (ORR, measured based on a microkinetic model) is plotted as a function of oxygen binding energy for a series of metal surfaces (using the facet with most close-packed atomic lattice arrangement). On the left side of the volcano plots are metal surfaces that bind too strongly to adsorbed oxygen species and the rate of ORR is limited by dissociation (surface is oxidized and reactivity is limited). On the right side of the volcano plots are metal surfaces that bind oxygen species too poorly. That rate of ORR on this side is most likely limited by the transfer of electrons and protons to adsorbed O_2. The rate limiting steps are different for each side of the volcano plot, giving rise to a different slope on the left versus the right side of the volcano.**

Note: Image adapted from works published by Nørskov et al. ((Nørskov, et al., 2004; V. Stamenkovic, et al., 2006)).

The trend observed for these volcano plots show that Pt catalysts are nearly optimal for ORR. This binding strength, though, can be altered through small modifications to Pt such as alloying with 3d metals (Fig. 1.2). To better understand this phenomena, the electronic structure of Pt must be considered. The electronic configuration of Pt is $[Xe]4f^{14}5d^{9}6s^{1}$. These electrons, as per molecular orbital/band theory, will be contained in bands for bulk Pt. The energy of interaction between the metal and incoming oxygen species largely depends on the overlap between the partially filled Pt d-band and the O 2p electrons, which results in the formation of bonding and antibonding states. The bonding states of Pt are filled and so the filling of the antibonding state defines the overall binding strength of the oxygen species to the metal surface. A shift to higher energy of the metal d-band results in an upward shift for the antibonding states. This leads to less filling of the antibonding states and a corresponding increase in oxygen binding energy. Alloying of Pt can induce changes to the d-band through an electronic effect (shifting the d-band up or down), a strain effect (changing the width of the Pt d-band), or a geometric effect (changing the bonding characteristics of the surfaces).(Hammer & Nørskov, 2000; Nørskov, et al., 2004; Santos & Schmickler, 2006; V. Stamenkovic, et al., 2006)

1.2.2. Mass Transfer of Reactants and Products

The rate of ORR at the CCL in a PEM FC is defined by the properties of the electrode surfaces, as discussed in the previous section, as well as the transport of reactants/products to/from these surfaces. There are three types of electrochemical mass transfer processes: diffusion, convection and migration. Diffusion is the movement of a species due to a chemical potential gradient (e.g., concentration gradient). Convection is a collective mass transfer process occurring due to fluid flow that may be natural (caused by density gradients across the fluid) or forced (e.g., stirring). Migration is the movement of a charged species in the presence of an electric field. Each of these processes are important to the overall performance of a PEM FC. For example, convective properties of the CCL are important for water management. Water management is a key issue in PEM FC design, since water tends to accumulate at the cathode due to electro-osmotic-drag from the anode and water production at the cathode. This accumulation of water can limit the rate of ORR at the cathode, since the effective diffusivity of gases through liquid water is low, which limits the amount of reactants that can reach the surfaces of the reactive catalyst layer. Designing catalyst layers with improved water management properties is, therefore, important to improve the overall performance of the CCL.(Bard & Faulkner, 2000; Chan & Eikerling, 2014; Ji & Wei, 2009; Yuan & Wang, 2008)

1.2.3. A Brief History of Pt-Based Cathodic Catalyst Layer Designs

Designing an effective CCL for ORR presents a great challenge to PEM FC technology. The CCL must have good mass transfer properties (as to enable efficient flow of reactants/products), stability under FC operating conditions, efficient proton transport, large Pt surface area, and good electrical conductivity. These requirements would ensure that the FC can generate electricity at a suitable rate throughout its lifetime. Additionally, the cost of the CCL should be kept low. This means that the mass of Pt in the CCL must be kept to a minimum. Preliminary FCs developed in the 1960s used a large mass of Pt (4 to 10 mg cm^{-2}) deposited on the current-collector (electrode). Massive research efforts aimed at finding CCL designs that could show increased performance (power generation) while minimizing Pt mass have since been undertaken. The development of catalyst inks (Fig. 1.3) in the 1990s greatly improved Pt utilization through the use of Pt nanoparticles on a non-catalytic, conductive support (e.g., graphitic carbon).(Gottesfeld & Zawodzinski, 2008; Ralph et al., 1997; Srinivasan, Manko, Koch, Enayetullah, & Appleby, 1990) These Pt nanoparticles exhibit a very high surface area for a small Pt mass. The use of a non-catalytic support enables dispersion of the Pt particles while providing a conductive path for current flow. These catalyst inks also contain ionomer (proton conducting polymer), which assists in stabilizing the catalyst ink and efficiently transporting protons to the Pt catalysts.(Bagotsky, 2008; David, 2002; Mark K Debe, 2012; Shen, 2008; H. Zhang, Wang, Zhang, & Zhang, 2008) Since the development of catalyst layer inks, most research efforts in the area of Pt-based CCL design have focused on modifying the ink properties to improve stability and optimize Pt utilization. Other research has focused on the design of new catalyst layer architectures. Some of these efforts have been highlighted in Table 1.1.

One of the major challenges in the use of ink-based catalyst layers is their poor stability under fuel cell operating conditions. Many different factors contribute to the degradation of these ink-based PEM FC CCLs. The Pt particles used in most current catalyst inks are between 2 and 6 nm. These Pt nanoparticles (NPs) can be mobile during operation of the FC, allowing them to fuse with other NPs (aggregation), form clumps with other NPs (agglomeration) or be expelled from the FC with the water by-product. The strongly oxidizing conditions present at the cathode can also oxidize the C black supports, further increasing the NP mobility and leading to further CCL degradation. Corrosion of the carbon support is especially problematic on start-up and shut down of the fuel cell, when the cathode can be exposed to potentials greater than 1.5 V. Platinum may also dissolve during FC operation, via both electrochemical (dissolution of bare Pt) and chemical (dissolution of Pt via its' oxides) routes. Finally, the Pt surfaces can be poisoned by contaminants such as sulfur containing compounds and carbon monoxide.(Bagotsky, 2008; Dam & de Bruijn, 2007; Dam, Jayasayee, & de Bruijn, 2009; David, 2002; de Bruijn, Dam, & Janssen, 2008; Kocha, 2012; Rand & Woods, 1972; Rinaldo, Stumper, & Eikerling, 2010; Y. Shao, Yin, & Gao, 2007; Shen, 2008; Topalov et al., 2014; Topalov et al., 2012; H. Zhang, et al., 2008)

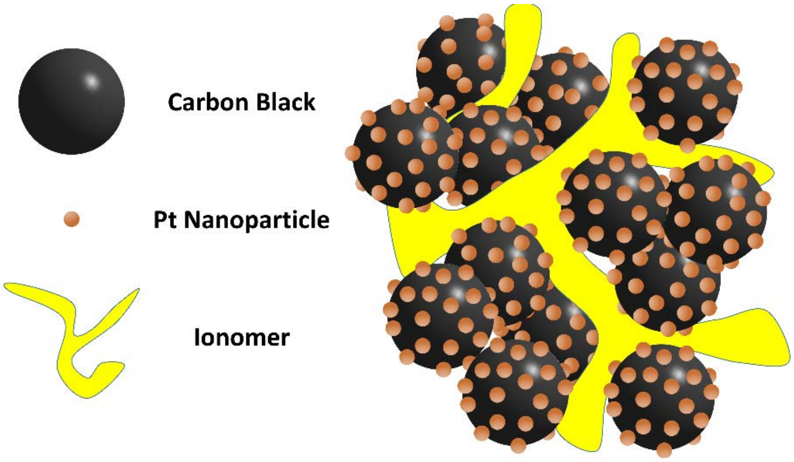

Figure 1.3 **Schematic of a catalyst ink. Spherical C black particles are coated in ionomer and Pt particle catalysts. During operation, water can swell the ionomer and be present throughout the catalyst layer.**

The mass activity of Pt (A mg_{Pt}^{-1}) is an important value in comparing the effective utilization of Pt in the CCL. Preliminary ink-based catalyst layer designs obtained mass activity values of up to 0.2 A mg_{Pt}^{-1}.(Ralph, et al., 1997) To put this in context, the DOE target for 2017 is > 0.44 A mg_{Pt}^{-1}. (Rabis, Rodriguez, & Schmidt, 2012; Satyapal, 2012) Much improvements have been made to ink-based catalyst layers in order to improve their stability and mass activity, as indicated in Table 1.1. These studies have also greatly improved our understanding of the CCL. However, the high cost of the CCL continues to hinder the commercialization of PEM FCs, driving research in the area of alternative CCL designs. To my current knowledge, the only industrially developed alternative catalyst layer design is the 3M nanostructured thin film (NSTF) CCL.

Table 1.1 Highlights of modifications made to catalyst ink designs for improvement of Pt mass activity and/or stability.

Modification Made to Catalyst Ink	Brief Summary of Findings	Example Reference(s)
Shape/size control of Pt NPs	• decreased size of Pt NPs results in increase surface area for less mass, but also leads to greater instability due to the large reactive surface area • greater mass activity for 111 faceted NPs (e.g., nanocubes) in comparison to other facets due to better interfacial properties	(C. Wang, Daimon, Onodera, Koda, & Sun, 2008), (Sheng, Chen, Vescovo, & Shao-Horn, 2011)
Substitute Pt NPs with Pt alloys or core/shell Pt particles	• homogeneous Pt alloys improve ORR activity by a factor of ~ 2 • de-alloyed Pt NPs (Pt skin over NP core) show further improvements	(Greeley et al., 2009), (V. R. Stamenkovic, Mun, Mayrhofer, Ross, & Markovic, 2006; Vojislav et al., 2007; J. X. Wang et al., 2009)
Substitute C black with more graphitic C nanostructures (e.g., C nanotubes or graphene)	• improved stability due to decrease in oxidative damage of support and stronger interaction between Pt catalysts and support • increased difficulty of Pt metal deposition	(Park et al., 2011; Y. Shao, Yin, Zhang, & Gao, 2006; Stevens, Hicks, Haugen, & Dahn, 2005)
Alternative supports/additives	• addition of metals (e.g., gold) or metal oxides (e.g., ceria, niobium oxides) as co-supports or catalyst modifiers can improve CO tolerance, stability and/or activity	(Chlistunoff, Wilson, & Garzón, 2011; Sasaki, Zhang, & Adzic, 2008; Y.-J. Wang, Wilkinson, & Zhang, 2011; J. Zhang, Sasaki, Sutter, & Adzic, 2007)

Note: Several references were used to help compile the information found in this table.(David, 2002; Mark K Debe, 2012; Gasteiger, Kocha, Sompalli, & Wagner, 2005; Rabis, et al., 2012; Y. Shao, et al., 2007; Wagner, Lakshmanan, & Mathias, 2010)

The 3M NSTF CCL consists of a thin layer of Pt sputter deposited onto the surface of an array of organic nanowhiskers to produce a high surface area Pt thin film. The final structures resemble a forest of whiskers with the dimensions of each whisker being ~ 50-nm x 25-nm x 1 to 2-µm (length x width x height). This design has a relatively low specific surface area (SSA) of 5 to 17 m^2 g_{-1} ($\boldsymbol{A}_{ecsa,Pt}$) in comparison to catalyst ink designs that can achieve greater than 40 m^2 g_{-1} ($\boldsymbol{A}_{ecsa,Pt}$). Despite this lower SSA, the 3M NSTF design shows improved ORR activity per mg of Pt due to a 5 to 10 fold increase in specific activity (current generated per cm^2 Pt $\boldsymbol{A}_{ecsa}$). The polycrystalline film also shows improved durability since it is already highly agglomerated, which limits the mobility of Pt (as to limit degredation via aggregation and agglomeration) and decreases the Pt surface energy (in comparison to nanoparticle catalysts, resulting in decreased Pt dissolution).(de Bruijn, et al., 2008) In addition, since this design does not utilize C supports, degradation via instability of the C support is absent. Instead, electron conduction is afforded by the continuous film of polcrystalline Pt.(Mark K Debe, 2012; Mark K. Debe, 2012)

To transfer the NSTF into a fuel cell, a roll-to-roll process is employed. This method flattens the nanowhisker array, so that the final NSTF CCL is between 200 and 600 nm. The ultrathin nature of this CCL (20 to 30 times thinner than traditional catalyst inks) enables it to be utilized without the addition of ionomer to conduct protons. Proton transportation within these ultrathin CCLs is not completely understood, but is believed to proceed through hydronium ions at the Pt surfaces, which is typically covered in hydroxyl groups. The protons may also be transported to the Pt surfaces through water, which could fill the CCL during FC operation. The ultrathin design can also improve the mass transfer properties of the CCL. For example, decreasing the thickness of the catalyst layer can improve the transport of O_2 from the GDL to the CCL, enabling it to access all regions of the CCL. This improved transport of O_2 (in conjunction with improved water management) allows for a greater amount of Pt to be used for electrocatalysis and increases the overall performance of the CCL. Several modifications have been made to the original pure Pt NSTF design in order to improve ORR activity, including the use of Pt alloys and metal oxide layer under the Pt thin film. Through these modifications, this design has achieved the 2017 DOE target for mass activity (> 0.44 A mg_{Pt}^{-1}). (Mark K. Debe, 2012; Rabis, et al., 2012; Satyapal, 2012)

Despite many performance improvements for the NSTF design (in comparison to traditional catalyst ink designs), there are still several issues that hinder the performance of this catalyst layer at the fuel cell cathode. Of particular concern is the water-management properties of these catalyst layers.(Chan & Eikerling, 2014; Kongkanand, Dioguardi, Ji, & Thompson, 2012; Kongkanand et al., 2012) At low humidity, poor performance is observed as attributed to limited proton conduction (e.g., a lack of water in the CCL limits proton transport).(Kongkanand, Dioguardi, et al., 2012; Kongkanand, Owejan, et al., 2012) Performance is also limited at low temperatures (e.g., less than ~80°C), due to flooding of the CCL (specifically the GDL).(Chan & Eikerling, 2014) Further improvements to this design are, therefore, still necessary to improve performance of these CCLs to meet necessary cost/performance requirements.(Mark K Debe, 2012; Mark K. Debe, 2012)

1.3. Evaluation of New Catalyst Layer Electrodes

1.3.1. Electron Microscopy and Related Techniques

Microscopy is a valuable technique for imaging materials at a scale smaller than the eye can see. The resolution of a microscope is generally limited by diffraction. Reducing the wavelength of the incident light decreases the diffraction limit and improves spatial resolution. For this reason, the use of an electron beam to image a nanoscale sample is advantageous. The small wavelength of the electron beam (< 1-nm) enables electron microscopes to image nanostructures and nanostructured surfaces. The images generated during electron microscopy (EM) can result from a variety of interactions between the electron beam and the sample (Fig. 1.4). In addition, the electron beam is an ionizing radiation source, producing a wide range of secondary signals with valuable chemical information.(Egerton, 2005; Watt, 1997; Williams & Carter, 2009)

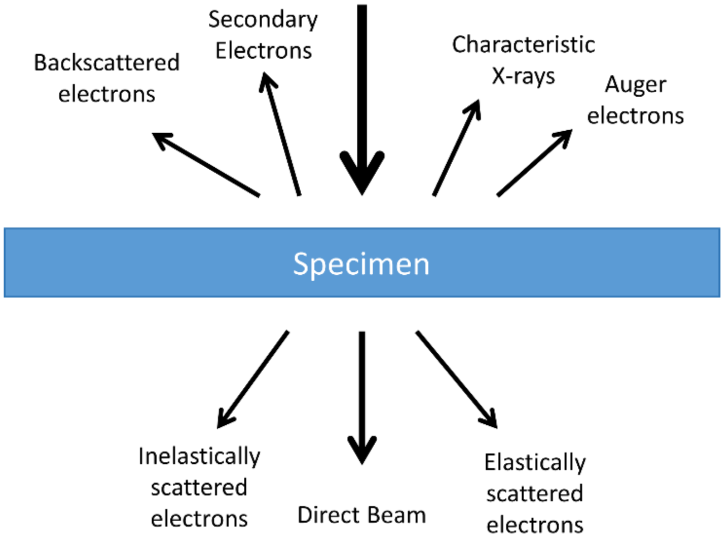

Figure 1.4 **Some of the signals generated by the interaction of a high energy electron beam with a thin sample.**

In transmission electron microscopy (TEM), a focused beam of electrons from an electron gun source pass through a thin sample (generally less than 100-nm thick). The electrons passing through the sample are focused to generate a projected image of the sample. Image contrast in the TEM image arises due to variations in electron density and thickness across the sample. In bright field mode, TEM images are formed from the incident electron beam. Regions with greater thickness or electron density are darker than those with less thickness or electron density in this mode. In dark field mode, images are formed from scattered electrons and not from the direct beam. Regions that are electron dense or thick scatter the beam more and so these areas appear bright. Regions with less thickness or electron density do not scatter the beam as much and so these areas appear dark in this mode. Scanning TEM (STEM) images are acquired by raster scanning a focused electron beam across the sample in either bright field or dark field mode. STEM mode is valuable in acquiring spatial chemical information (discussed below) and for samples that may be readily damaged by constant electron beam irradiation.(Egerton, 2005; Watt, 1997; Williams & Carter, 2009)

In scanning electron microscopy (SEM) a focused electron beam from an electron gun is raster scanned across the surface of the sample. Images in SEM are generated from the collection of backscattered, secondary and/or reflected electrons.

Contrast in an SEM image can arise from variation in composition and/or topography. The relative brightness of areas with different composition is proportional to the difference in the average atomic number (an increase in atomic number results in increased brightness), which results in a variation in the amount of backscattered, secondary and/or reflected electrons from the sample surfaces. The detection of secondary and backscattered emissions is sensitive to the angle of the surface relative to the incident electron beam, giving rise to topographical contrast.(Egerton, 2005; Watt, 1997)

Characteristic X-rays emitted from the sample can be detected by energy dispersive spectrometer in either a TEM or SEM. This technique is referred to as energy dispersive X-ray spectroscopy (EDS) and can provide valuable chemical information about the sample. During EDS analysis, all X-ray peaks are measured simultaneously and plotted as counts versus energy (eV) of the emitted X-rays. Both qualitative (e.g., elemental composition) and quantitative information can be derived from this plot. Raster scanning of the electron beam over the surface of the sample, such as for SEM or STEM analysis, provides spatial chemical information about the sample and enables the generation of elemental maps for a region of interest. (Egerton, 2005; Watt, 1997)

1.3.2. X-ray Photoelectron Spectroscopy

X-ray photoelectron spectroscopy (XPS) provides information on both the atomic composition of a material and the oxidation state of its components. In a typical XPS experiment, monochromatic X-rays (with energy h*v*) irradiate a sample causing it to eject inner shell photoelectrons. The kinetic energy (E_k) of the emitted electrons are detected by an electron energy analyzer. Analysis of the binding energy (E_b, defined by Eq. 20) and count rate (counts per second, cps) provides information on the chemical state of the surfaces (Fig. 1.5).

$$E_b = E_k - hv - \Phi_s \qquad (20)$$

In this equation, Φ_s is the work function of the spectrometer (a correction factor for the electrostatic environment in the XPS). Binding energy can be regarded as the energy required to remove the photoelectron from its orbital. This binding energy is characteristic of the element and the orbital from which the photoelectron is emitted. A survey plot of E_b versus count rate will always have a large background arising from inelastic collisions of emitted electrons with the sample. For all orbital levels, other than s levels, a doublet is observed in the XPS spectra due to spin-orbit splitting. Peaks from Auger electrons are also commonly seen in a survey spectrum plot, which results from the emission of a second electron upon relaxation of an atom after emission of an X-ray photoelectron.(Skoog, Holler, & Crouch, 2007) (Moulder, Stickle, Sobol, & Bomben, 1992)

Quantitative analysis of the surface chemical composition is calculated using the integrated area of the XPS peaks with considerations for relative sensitivity factor of the element of interest and instrument variations. Curve fitting of high-resolution XPS spectra provides further details into the chemical state of a specific element of interest at the sample surface. A number of factors must be considered for fitting of a high-resolution Pt 4f XPS spectra. First of all, we will consider the spin orbit splitting. For 4f electrons, n (the principle quantum number) is 4, l (the angular momentum quantum number) is 3 and s (the spin angular momentum quantum number) is ±½. These quantum number values gives rise to 2 different values for j (the total angular momentum quantum number, $l + s$) and results in 2 core levels observed by XPS (n^l_j) of $4f_{5/2}$ and $4f_{7/2}$. The area within the peaks corresponding to $4f_{5/2}$ and $4f_{7/2}$ will also always be at a defined 3:4 ratio due to the degeneracy of each spin state (6 electrons in the $4f_{5/2}$ level and 8 electrons in the $4f_{7/2}$ level). The next factor to consider in the fitting of the Pt 4f XPS spectra is the oxidation state of the Pt at the sample surface. Each oxidation state of Pt will have a different characteristic binding energy and will result in a doublet peak in the XPS spectra. Finally, we must consider the chemical state of the Pt at the sample surfaces. Interactions of Pt with other elements will also have a characteristic binding energy and will be associated to a doublet peak in the XPS spectra. Fitting of the Pt 4f peaks is necessary to deconvolute these components in the Pt 4f peaks. This analysis can also determine the relative contributions for each component (e.g., oxidation state, alloy) to the Pt 4f, providing details on the chemical environment of Pt within the electrocatalyst design.(Moulder, et al., 1992; Skoog, et al., 2007)

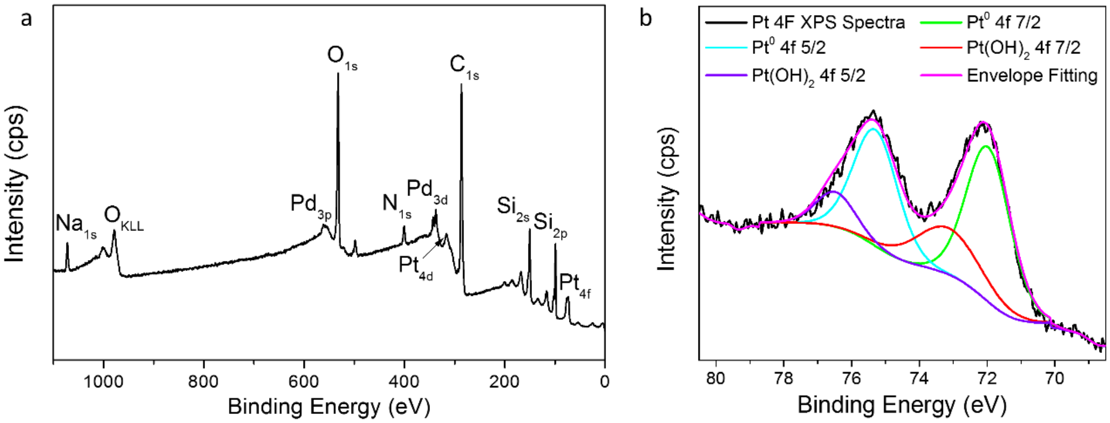

Figure 1.5 **Examples of (a) survey and (b) high-resolution XPS spectra. In the survey spectrum, photelectron peaks are marked using atomic notation (e.g., O_{1s}). Auger peaks are marked using X-ray notation (e.g., O_{KLL}). Fitting of the high-resolution Pt_{4f} peaks in the high-resolution spectra enable contributions from Pt^0 and $Pt(OH)_2$ to be distinguished.**

1.3.3. Three-Electrode Electrochemical Setup

In an electrochemical system, we are interested in the processes occurring at the electrode/electrolyte interface when an electric potential is applied and a current flows. In order to evaluate the electrochemical processes that occur at the electrode/electrolyte interface, we must have a means of accurately applying an electric potential (potentiostatic experiments) or electrical current (galvanostatic experiments) to the electrode and to measure the resulting current or potential, respectively. This can be achieved with an electrochemical cell. Herein, we use a three-electrode setup consisting of a working electrode (WE), a reference electrode (RE) and a counter electrode (CE) as depicted in Fig. 1.6. All three electrodes are immersed in electrolyte, which acts as a conductive medium (e.g., dilute H_2SO_4). The WE is the electrode of interest for the experiment being performed (e.g., an electrocatalyst material). The RE is a standard electrode with essentially a constant composition, such that a known electrochemical processes is always occurring at this electrode and the potential at this electrode is fixed. The applied electric potential is, therefore, measured with respect to the RE and all changes in the cell are attributed to changes at the WE. The CE is the primary electrode for current flow to/from the WE. In this setup, only a very small current flows from the RE to the WE in order to measure the applied potential. Electrochemical testing is carried out using a potentiostat (or galvanostat), which can apply a potential (or current) to the working electrode and measure the resulting current (or potential). This setup allows for the electrochemical properties of the WE to be accurately studied. In the following studies, iR compensation was not performed. In most cases it was found that the currents generated at the surfaces of the WE were of a small enough magnitude that iR losses were deemed insignificant. In rare cases, the current generated at the WE during cyclic voltammetry experiments was sufficiently large and artifacts of iR loss issues could be seen (e.g., “tilting” of the CV profile). In these cases, the scan rate was reduced to decrease the generated currents.(Bard & Faulkner, 2000; Sawyer, Sobkowiak, & Roberts, 1995)

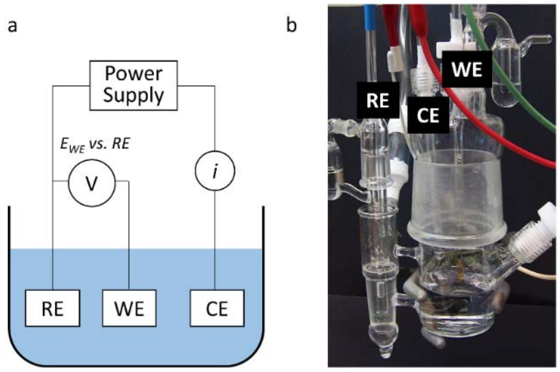

Figure 1.6 **(a) Schematic of a three-electrode electrochemical setup. The reference (RE), working (WE) and counter (CE) electrodes are immersed in electrolyte (blue). The potential between the WE and RE electrode is monitored (V) to establish the potential at the WE with respect to the constant potential at the RE. A power supply applies a potential to the WE and resulting current (*i*) between the WE and CE is monitored to detect reduction and oxidation processes occurring at the surface of the WE. (b) Photograph of the three-electrode setup employed for many of the studies in this thesis work. The RE is in a separate compartment, which is in electrical contact with the WE through a luggin capillary. This compartmentalization allows for reactive species (such as O_2 gas) to be present in the WE compartment without impacting the potential at the RE.**

1.3.4. Cyclic Voltammetry

Cyclic voltammetry (CV) is a potentiodynamic electrochemical technique whereby the electric potential of the WE is linearly scanned forward and backward between a low (E_1) and a high (E_2) applied potential at a constant sweep rate (v, mV s^{-1}) (Fig. 1.7). We employ CV to study processes that occur at the surface of our electrodes. The current measured is a result of both faradaic processes, such as oxidation and reduction, and non-faradaic processes (capacitive current), such as adsorption and desorption. This method provides an overview of the electrochemical processes occurring at our electrode/electrolyte interface.(Bard & Faulkner, 2000; Sawyer, et al., 1995) Further discussion of CV experiments are explained in the context of Pt electrodes and the interpretation of their CV profiles below.

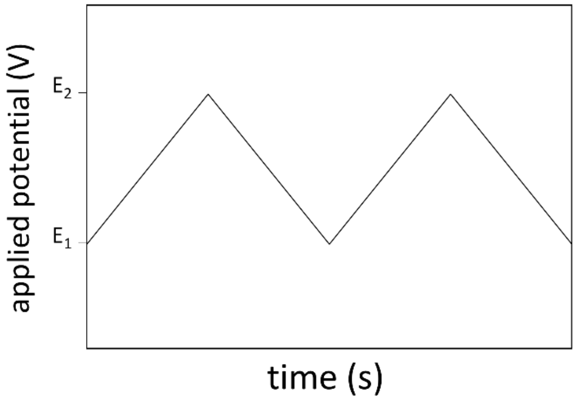

Figure 1.7 Potential-time relationship for a cyclic voltammetry measurement (the plot depicts 2 cycles).

Typical CV traces of Pt in this research are obtained between E_1=0.05V and E_2=1.25 V vs. a reversible hydrogen reference electrode (RHE) in a dilute H_2SO_4 electrolyte. Both E_1 and E_2 are defined by the potential region at which the electrolyte is stable. Below E_1 hydrogen gas is produced at the Pt WE through the hydrogen evolution reaction. Above E_2 oxygen is produced at the Pt WE through the oxygen evolution reaction. These upper and lower potential limits are also in line with potentials typically experienced by the cathode under fuel cell operation. A typical CV trace for a polycrystalline Pt electrode over this potential region is displayed in Fig. 1.8. The current measured during this CV analysis results from double layer charging (C_{DL}, non-faradaic capacitive current), underpotential deposited H (H_{upd}) and Pt oxide formation/reduction. The profile of the H_{upd} adsorption and desorption peaks (~ 0.05 to 0.4 V vs. RHE) arises from the differential adsorption energy for H_{upd} on different facets of crystalline Pt. For the forward scan, H_{upd} desorption primarily occurs on (110) facets between ~ 0.05 to 0.15 V vs. RHE, on (111) facets between ~ 0.15 to 0.25 V vs. RHE and on (100) facets between ~ 0.25 to 0.4 V vs. RHE. Pt oxide formation begins at ~ 0.85 V vs. RHE. In the region between ~ 0.4 – 0.5 V vs. RHE, double layer capacitance accounts for the slight positive (forward scan) and slight negative (reverse scan) current. This constant C_{DL} current is present throughout the CV profile due to double layer charge formation at the Pt surfaces. Pt oxide formation has an onset potential of ~ 0.85 V vs. RHE. The peaks seen in the profile in this region result from complex processes that are not yet completely understood. Between 0.85 and 1.15 V, oxygen chemisorbs onto the surfaces of the Pt. Above 1.15 V, chemisorbed oxygen undergoes a place exchange to form sub-surface Pt oxide (further discussion of sub-surface Pt oxide can be found above in the section “Platinum Dissolution”).(Angerstein-Kozlowska, Conway, & Sharp, 1973; Jerkiewicz, 2010; Jerkiewicz, Vatankhah, Lessard, Soriaga, & Park, 2004; Yamamoto, Kolb, Kötz, & Lehmpfuhl, 1979)

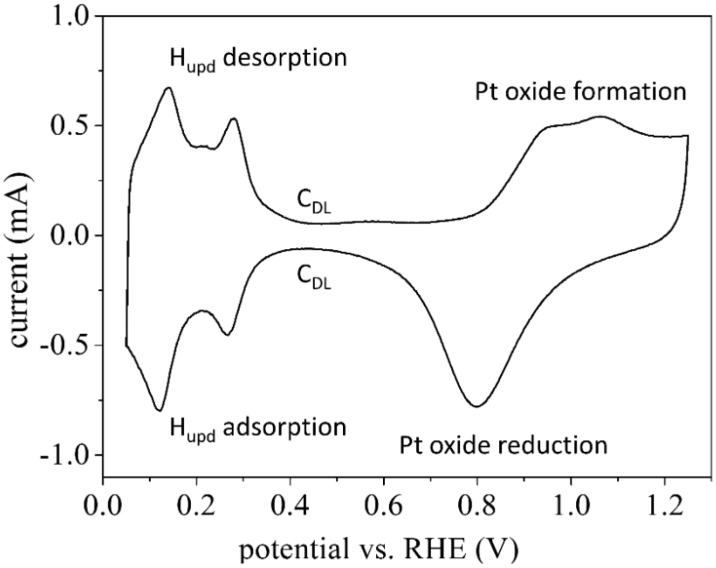

Figure 1.8 Typical CV profile of a polycrystalline Pt electrode.

Analysis of the Pt CV profile also provides key information regarding our electrochemical setup. Purity of the system is assessed by examining the overall appearance of the profile. Specifically, if the CV is not centered about 0 A or if the CV profile is tilted, the system contains impurities. These effects on the CV profile can be the result of reactive (e.g., oxygen gas) or non-reactive impurities that can oxidize or reduce at the Pt surface, altering the appearance of the CV profile. The relative intensity of the three H_{upd} desorption peaks (as discussed earlier) provides information on preferential Pt grain orientation. Platinum electrochemical (or real) surface area ($\boldsymbol{A}_{ecsa}$) can be evaluated via Eq. 13 below, where q_H ($\mu C\cdot cm^{-2}$) is the charge for stripping a monolayer of adsorbed H_{UPD} from the Pt WE and q_S is the known charge density for the stripping of a monolayer of H_{UPD} from a comparable Pt electrode (e.g., polycrystalline Pt in dilute H_2SO_4). The experimental value of q_H is determined by integrating the H_{UPD} desorption peak (minus contributions from C_{DL}) and dividing by the scan rate.(D. Chen et al., 2011; Rand & Woods, 1972) (Angerstein-Kozlowska, et al., 1973; Jerkiewicz, 2010;

Jerkiewicz, et al., 2004; Yamamoto, et al., 1979) Further details can be found in Appendix B.

$$\boldsymbol{A}_{ecsa} = \frac{q_H}{q_S} \tag{13}$$

The real surface area can be subsequently used to determine the roughness factor (**RF**) of the electrode The roughness factor is calculated by dividing $\boldsymbol{A}_{\mathrm{ecsa}}$ by the geometric area of the electrode ($\boldsymbol{A}_{\mathrm{geom}}$). This value is dependent on a number of factors, including thickness, porosity, surface roughness and/or NP size. The specific surface area (**SSA**) of Pt defines the ability of the electrode design to translate Pt mass into electrochemical accessible Pt surface area. The **SSA** of a Pt electrode is determined by dividing $\boldsymbol{A}_{\mathrm{ecsa,Pt}}$ by the mass of Pt in the electrode. Monitoring changes in Pt $\boldsymbol{A}_{\mathrm{ecsa}}$ during electrochemical treatment is also a valuable tool for evaluating the stability of new Pt-based electrocatalysts since it can provide insights into degradation of the catalyst layer via Pt dissolution, Pt NP aggregation and Pt NP agglomeration (all will result in a loss in $\boldsymbol{A}_{\mathrm{ecsa,Pt}}$).(Mark K Debe, 2012; Mark K. Debe, 2012; Kinkead et al., 2013; H. Zhang, et al., 2008)

1.3.5. Tafel Plots

Tafel plots are commonly used to evaluate key relations between the applied potential and the resulting current from an electrochemical reaction at the electrode/electrolyte interface. This relationship, between current and applied potential, is described by Butler-Volmer kinetic equations. From Tafel plot analysis, the exchange current density (j_{o},, A m^{-2}) and the transfer coefficient (α, dimensionless) of an electrochemical reaction at a defined electrode/electrolyte interface can be determined. The j_{o} of an electrochemical reaction defines how fast the reaction proceeds (or how fast a reaction comes to equilibrium) and is a measure of the kinetic rate of an electrochemical reaction. The α of a reaction defines the symmetry of the energy barrier for an anodic or cathodic process of an electrochemical reaction. For example, if α = 0.5, the anodic and cathodic reactions have the same relation between applied potential and resulting current density, but with opposite current flow. Here, we consider the Butler-Volmer equation that describes the relation between current density (j, A m^{-2}) and overpotential (ɳ = E - E_o, V, difference between the measured potential onset and the thermodynamic electrode potential for an electrochemical reaction) under conditions where mass transfer does not limit current flow and the surface concentration of the reactive species (e.g., O_2 for ORR) can be considered equal to the bulk concentration.

$$j = j_o\left[e^{-\frac{\alpha nF\eta}{RT}} - e^{\frac{(1-\alpha)nF\eta}{RT}}\right] \tag{14}$$

In this equation, n is the number of electrons transferred during the reaction, F is Faraday's constant (C mol^{-1}), R is the universal gas constant (J mol^{-1} K^{-1}), and T is temperature (K). At low ɳ (more detail on what is low/high ɳ is provided below), both the forward and reverse reaction can occur and both contribute to the resulting current density. For sufficiently large values of ɳ, only the forward (if ɳ > 0) or reverse (ɳ < 0) reaction needs to be considered. This understanding allows the bracketed term for either the forward (term containing 1 – α) or reverse (term containing only α) to be negligible at high ɳ. Equation 14 can then be re-arranged to another form, known as the Tafel equation (Eq. 15).

$$\eta = \mathrm{a}\, log j - b \tag{15}$$

$$a = \frac{2.3RT}{\alpha nF} \tag{16}$$

$$b = \frac{2.3RT}{\alpha nF} log j_o \tag{17}$$

A plot of log j vs. ɳ, also known as a Tafel plot, can be used to determine experimental values for j_o and α (assuming n is known, Eq. 16-17, Fig. 1.9). In this plot, the region near ɳ = 0 where the slope is changing with increasing ɳ defines the region of low ɳ. The region with constant slope is defined by the Tafel equation. At very high ɳ, mass transfer limits the electrochemical reaction and the slope again begins to change. A Tafel plot can be generated experimentally using steady-state polarization, whereby the potential is held at a defined ɳ and the steady-state current measured over a suitable ɳ range (or vice-versa, where current is held constant and ɳ is measured). For the ORR at the surfaces of polycrystalline Pt, j_o is ~ $1 \cdot 10^{-10}$ (A cm^{-2}) and α is ~ 0.5.(C. Song & Zhang, 2008) (Bard & Faulkner, 2000)

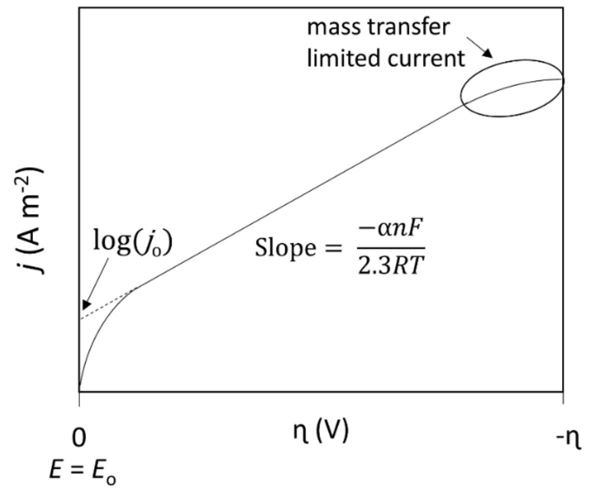

Figure 1.9 **A typical Tafel plot for a cathodic reaction.**

1.3.6. Rotating Disk Electrode Technique and Koutecky-Levich Analysis

Mass transfer in a three-electrode setup is generally limited by diffusion and convection to the WE surfaces. Forced convection through the use of hydrodynamic methods, such as rotating disk electrode (RDE) techniques, allow the convective mass transfer limitations to be overcome. These hydrodynamic methods enable a steady-state to be achieved quickly and the electron transfer kinetics to be less limited by overall mass transfer effects. The flux of the reactants to the surfaces and profile of convective flow to the electrode can be determined using transport equations and fluid dynamics as applicable to the hydrodynamic method used. For RDE technique, a cylindrical electrode is rotated at a defined angular velocity (s^{-1}) to induce a laminar flow of reactants to the electrode. Mass transfer to the electrode is now defined entirely by diffusion at the electrode surface. A plot of η vs. *i* with a profile such as that depicted in Fig. 1.9 is obtained by linear sweep voltammetry from η = 0 to negative overpotentials (for a cathodic reaction) with a RDE rotating at a defined angular velocity. At high η, current is limited by mass transport and independent of time (the limiting current region). The current in this region is controlled by the thickness of the diffusion layer as determined by the rotation speed (convective flux to the electrode surface) and is described by the Levich equation (Eq. 18).

$$i_l = 0.62nFAc_{ox}^{b}D^{2/3}v^{-1/6}\omega^{1/2} \tag{18}$$

In this equation, i_l is the Levich current, n is the number of electrons transferred, F is Faraday's constant, A is the area of the electrode (cm^2), c_{ox}^{b} is the concentration of dissolved oxygen (~ $1.1 \cdot 10^{-6}$ mol cm^{-3} in dilute H_2SO_4 at 25°C, 1 atm. O_2), D is the diffusion coefficient of oxygen (~ $1.4 \cdot 10^{-5}$ cm^2 s^{-1} in dilute H_2SO_4 at 25°C, 1 atm. O_2), v is the kinematic viscosity of the solution (~ 0.010 cm^2 s^{-1} for dilute aqueous solutions at 25°C, 1 atm. O_2) and ω is the rotational speed of the electrode (rad s^{-1}). For a Nernstian reaction, the Levich equation can be combined with the Nernst equation to yield the Koutecky-Levich (KL) equation (Eq. 19).

$$\frac{1}{i} = \frac{1}{i_k} + \frac{1}{i_l} = \frac{1}{i_k} + \frac{1}{0.62nFAc_{ox}^{b}D^{2/3}v^{-1/6}\omega^{1/2}} \tag{19}$$

In the KL equation, i_k is the kinetic current density (in the absence of any mass transport limitations). Koutechy-Levich analysis is performed using a plot of 1/i (in the limiting current region) vs. $\omega^{-1/2}$.(Bard & Faulkner, 2000; Qi, 2008; C. Song & Zhang, 2008)

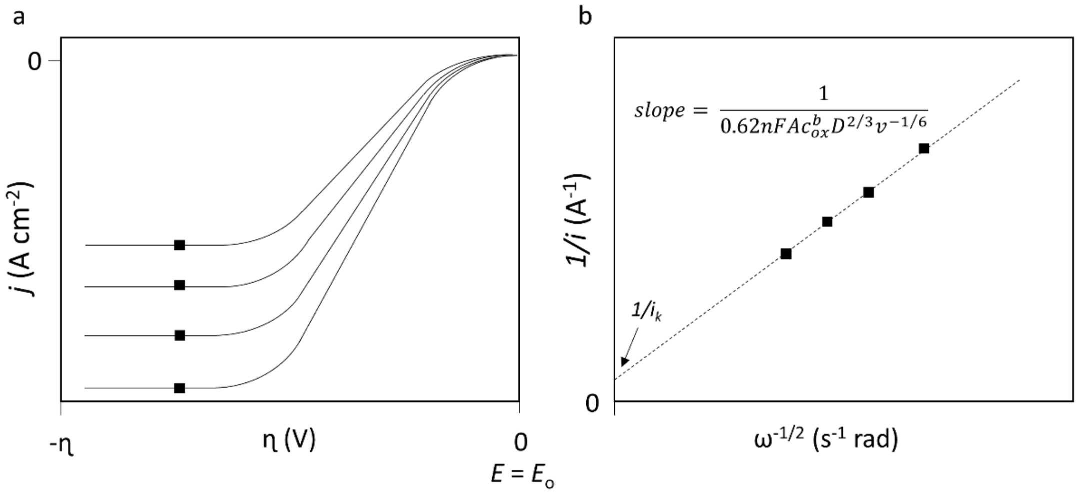

Figure 1.10 (a) Typical RDE potential-sweep voltammograms (cathodic reaction) obtained at different electrode rotation speeds. (b) A typical KL plot. Note that the data points represented by squares on the first plot are the same data points on the KL plot.

Several important parameters can be derived from the plots shown in Fig. 1.10. In order to compare the activity of different electrocatalysts towards ORR, it is common to assess the *j* (A cm^{-2}, $\boldsymbol{A}_{ecsa,Pt}$) at an applied potential of 0.9 V for an RDE potential-sweep voltammogram (such as that seen in Fig. 1.9a) obtained at a defined rotational speed. An applied potential of 0.9 V is generally chosen for this assessment since this is a desirable value of η for operation of a fuel cell (η is large enough for significant current to flow, but still small enough that the mass transfer does not present significant limitation to the current acheived). This current density is referred to as the specific activity for that electrode. Similarly, the current can be normalized by Pt mass, instead of $\boldsymbol{A}_{ecsa}$, to evaluate the mass activity of the electrode at an applied potential of 0.9 V for an RDE potential-sweep voltammogram obtained at a defined rotational speed. The values of *n* and i_k can be determined from analysis of a KL plot. The value of *n* for an electrode/electrolyte interface of interest can be determined from the slope of the KL plot (Fig 1.9b, Eq. 19). For ORR on Pt, *n* should ideally be 4 such that the reaction proceeds through the direct 4 e$^-$ transfer and not through a peroxide intermediate or some other mechanism. The value of i_k can be determined from the intercept of the KL plot (Fig. 1.9b, Eq. 19). In summary, the RDE method is a valuable tool for analysis of electrochemical reactions and the comparison of ORR electrocatalytic activity for similar electrodes under specific conditions. (Bard & Faulkner, 2000; Mayrhofer et al., 2008; Paulus, Schmidt, Gasteiger, & Behm, 2001; Qi, 2008; C. Song & Zhang, 2008; Vidal-Iglesias, Solla-Gullón, Montiel, & Aldaz, 2012)

1.4. Objectives of the Thesis

The purpose of this thesis work is to design and develop methods for the preparation of new Pt-based electrocatalysts. The designs sought in this work are motivated by a number of factors, including: i) the enhanced performance observed for ultra-thin designs; ii) continued issues with ultra-thin designs relating to water-management; iii) the pursuit of improved understanding of the effects of pore size and catalyst layer thickness on mass transport properties (e.g., water management); iv) the desire to prepare ultra-thin catalyst layers with better SSA (via the use of nanoparticles) and through a more tunable route (e.g., NP loading, support interactions).(Chan & Eikerling, 2014; de Bruijn, et al., 2008; Kongkanand, Dioguardi, et al., 2012) The utilization of Pt in the context of this thesis work is characterized by a number of conditions: i) stability of Pt within the electrocatalyst design (using *ex situ* methods); ii) specific surface area of Pt; and iii) anticipated mass transfer properties of the electrocatalyst. These terms determine how well Pt mass is translated into catalytically active surfaces for the lifetime of the intended device. The effective utilization of Pt also includes the ability of reactants to access the Pt surfaces and products to escape during fuel cell operation in order to optimize catalytic turnover at the Pt surfaces. New electrocatalyst architectures are proposed as alternatives for replacing currently used CCLs in PEM-FCs and as model designs that can provide further insight into fundamental fuel cell catalyst layer phenomena.

The electrode designs explored in this thesis work include pure Pt ordered porous (Pt-OP) electrodes, ordered porous supported Pt NP (support@PtNP-OP) electrodes and support@PtNP nanobowl catalyst inks. These electrodes have been prepared through the use of sacrificial templates composed of bare (for Pt-OP) or NP coated polystyrene spheres (Au@PtNP-OP and nanobowls). The use of these templates for the preparation of the new catalyst layer designs will be discussed in the corresponding chapters. Overall, this thesis aims to demonstrate new methods for the preparation of alternative catalyst layer designs with the potential to improve our understanding of mass transport (and water-management) issues at the cathode and enhance the performance of CCLs in low-temperature fuel cells.

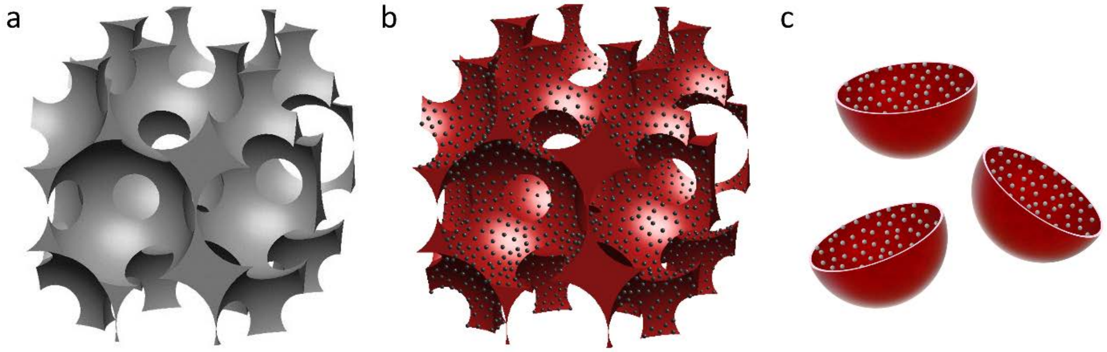

Figure 1.11 **Schematic of the three different electrocatalyst designs explored in this thesis work: (a) Pt-OP electrodes; (b) support@PtNP-OP electrodes; and (c) support@PtNP nanobowls.**

Chapter 2.

Pure Platinum Ordered Porous Electrodes

2.1. Notice of Permissions

The following chapter is based upon work previously published: Brandy Kinkead, Julia van Drunen, Michael T. Y. Paul, Katie Dowling, Gregory Jerkiewicz and Byron D. Gates, "Platinum Ordered Porous Electrodes: Developing a Platform for Fundamental Electrochemical Characterization", Electrocatalysis 2012, 4 (3), 179-186. Permission to use the following material has been granted by the publisher and all co-authors. The final publication is available at http://link.springer.com/article/10.1007%2Fs12678-013-0145-2. Most of the work presented in this paper, including data interpretation and writing, has been performed by myself. Julia van Drunen assisted in performing the electrochemical characterizations (electrochemical setup, experimental design and data interpretation). Michael T. Y. Paul and Katie Dowling helped in initial experiments towards the preparation of the ordered porous electrodes.

2.2. Introduction

Platinum electrodes with a large $\boldsymbol{A}_{\mathrm{ecsa}}$ can be prepared by a number of methods. One approach is the synthesis and subsequent deposition of Pt nanoparticles onto an electronically conductive support, such as the use of C supports as described in Chapter 1. The use of Pt nanoparticles produces a large $\boldsymbol{A}_{\mathrm{ecsa}}$ for a relatively small Pt loading, but requires that the support and electrocatalyst-support interactions remain stable during electrochemical reactions.(Aiken Iii & Finke, 1999; Steele & Heinzel, 2001) Another approach involves platinization of high surface area or sacrificial templates to produce Pt electrodes with a large $\boldsymbol{A}_{\mathrm{ecsa}}$. This type of electrode is commonly achieved by either physical vapour deposition (e.g., the 3M NSTF design described in Chapter 1) or electrodeposition techniques. Physical vapour deposition onto a high surface area support can produce large $\boldsymbol{A}_{\mathrm{ecsa}}$ Pt electrodes, but is a directional technique and is, therefore, limited in its' ability to equally control the distribution of Pt over three dimensions.(Bonakdarpour, Fleischauer, Brett, & Dahn, 2008; Mark K. Debe, 2012; Giorgi et al., 2011; Guizard & Princivalle, 2009; Hayden, Pletcher, Suchsland, & Williams, 2009) Electrodeposition through a sacrificial template (e.g., lyotropic liquid crystals(Attard, Goltner, Corker, Henke, & Templer, 1997) or polycarbonate membranes(Choi, Kim, Jung, Yoon, & Kim, 2008; Mahshid et al., 2011; M. Yang et al., 2006)) is a versatile method for creating porous Pt electrodes with a variety of pore shapes, sizes, and interconnectivity without the need for a secondary support. Depending on the sacrificial template, such prepared Pt electrodes can have a large $\boldsymbol{A}_{\mathrm{ecsa}}$. For our studies, we sought a structure and composition amenable to gaining a fundamental understanding on the effect of electrode morphology on the electrocatalytic behavior of Pt electrodes for applications in energy-generating devices.

Prior studies demonstrated the feasibility to prepare ordered porous electrodes via colloidal templates and their use in electrochemical applications.(Bai, Yang, Sun, & Sun, 2008; P. N. Bartlett, Baumberg, Birkin, Ghanem, & Netti, 2002; Philip N. Bartlett, Birkin, & Ghanem, 2000; C. Chen, Li, & Liu, 2009; Du, Lv, Su, Zhang, & Wang, 2009; Y.-J. Huang, Lai, Wu, & Chen, 2010; Y. Liu, Chen, Misoska, Sweigers, & Wallace, 2007; Mine & Shirai, 2009; T. Song et al., 2012; Y.-Y. Song, Zhang, Gao, & Xia, 2005) These studies include the preparation of nickel ordered porous electrodes for use in alkaline water electrolysis,(Y.-J. Huang, et al., 2010) hierarchical Ge ordered porous electrodes for anodes in lithium-ion batteries,(T. Song, et al., 2012) and Au and Pt ordered porous electrodes for the detection of dissolved glucose.(Bai, et al., 2008; Y.-Y. Song, et al., 2005) Platinum ordered porous and Pd modified Pt ordered porous electrodes were also prepared for applications in direct methanol fuel cells.(C. Chen, et al., 2009; Du, et al., 2009; Y. Liu, et al., 2007) In this contribution, we report on the systematic preparation of pure Pt ordered porous (Pt-OP) electrodes (Fig. 2.1) and their characterization using material science and electrochemical techniques. The aim of this research is to develop a platform for the identification and quantification of the relationship between structure and electrocatalytic activity. Therefore, these electrodes were designed with a specific pore size, interconnectivity, and thickness. Our analysis also includes assessment of reproducibility in preparing these Pt-OP electrodes, as well as their electrochemical characteristics and long-term stability.

2.3. Experimental

The Pt-OP electrodes were built upon a suitable electronically conducting support that also serves as a platform for characterizing these porous materials. We demonstrated the principles described herein using a silicon wafer supported gold film (200 nm), with a 5-nm Cr adhesion layer in between the surface and support prepared *via* thermal evaporation in a Kurt J. Lesker physical vapour deposition system. These substrates were fractured into approximately 1 cm × 2 cm rectangles. This support provided flat, conductive surfaces that did not interfere with electrochemical measurements of the Pt-OP electrodes. Polystyrene (PS) spheres with a hydrodynamic diameter of 460 nm (Polysciences, Inc.) were self-assembled at an air-water interface using an adaptation of a previously reported procedure.(Moon et al., 2011) In brief, PS spheres (1 wt% in 1-BuOH) were drop cast onto the air-water interface of heated (~40°C), freshly deionized water (18.2 MΩ cm). Drops of solution containing PS spheres were added until the droplets no longer dispersed across this interface. The resulting assemblies of PS spheres were transferred onto the conductive support (after rinsing the support with ethanol) by a dip coating process. Multiple layers of PS sphere were assembled onto these supports by repeated dip coating. Such assembled layers of close-packed PS spheres were dried overnight in a vacuum desiccator and, subsequently, rinsed with ethanol to remove any residual 1-BuOH from the self-assembly process. Platinum electrodeposition was accomplished by potential cycling of the gold substrate between -0.18 and 1.20 V vs. Ag/AgCl at a potential scan rate of 175 mV s^{-1}.(Y. Liu, et al., 2007) The aqueous electrodeposition solution contained 5 mM of H_2PtCl_6 (Sigma Aldrich, ACS Grade), 0.2 M of H_2SO_4 (Fisher Scientific, ACS Grade) and ~35 mM of polyvinylpyrrolidone (Sigma Aldrich, 55k MW). The addition of PVP is intended to improve the uniformity of the Pt deposit within the sacrificial PS template by decreasing the size of Pt nanoparticle deposits (effectively enabling more conformal Pt deposition within the sacrificial template).(Y.-J. Song, Oh, & Park, 2008) After Pt electrodeposition, the PS template was removed by Soxhlet extraction with refluxing toluene for at least 4 h. Extracted porous electrodes were immersed and sonicated in first a solution of acetone and then a solution of isopropanol to remove traces of organic material originating from the preparation of the electrode. The geometric area ($\boldsymbol{A}_{\text{geom}}$) of the prepared electrodes was determined by photographing the electrodes on grid paper (Figure 2.1d) and evaluating the area occupied by the electrode with ImageJ 1.45s software.

The solvent washed Pt-OP electrodes were imaged by using a Strata DB235 FESEM/FIB to evaluate thickness, pore shape and size, and long-range order within the Pt-OP electrodes. X-ray diffraction analysis was performed using a Rigaku Rapid-Axis Diffractometer with a Cu Kα1 radiation source (λ = 1.5406 Å) to examine the grain size of Pt crystallites within Pt-OP electrodes. Platinum mass loading was evaluated by flame atomic absorption spectroscopy (FAAS) using an Aurora Biomed TRACE AI1200 spectrometer equipped with a Pt hollow cathode lamp. After electrochemical examination, each Pt-OP electrode was digested in a solution of aqua regia for FAAS analysis. The aqua regia solution was prepared from a 3:1 (v/v) solution of hydrochloric acid (36.5 – 38.0% in water; Anachemia Canada, Inc., Richmond, BC, Canada) and nitric acid (68 – 70% in water; Anachemia Canada, Inc., Richmond, BC, Canada). CAUTION: *Aqua regia solutions are extremely corrosive. This solution should be handled with extreme care*.

Electrochemical measurements were carried out using a Princeton Applied Research model 263A potentiostat with a RHE as a reference electrode and Pt gauze with electrodeposited Pt black as a counter electrode. All electrodes and the custom-made electrochemical cell used in this study were prepared by Verrerie de Precision Enr. Platinum electrode materials were supplied by Alfa Aesar (Pt ≥ 99.9%). Glassware, counter and reference electrodes were cleaned by established methods prior to use.(Angerstein-Kozlowska, et al., 1973; Conway, Angerstein-Kozlowska, Sharp, & Criddle, 1973) Before each electrochemical experiment, working electrodes were refluxed in isopropanol to remove organic surface residues. High purity N_2 gas (Praxair, 99.998%) was bubbled through the electrolyte to expel any reactive gases prior to electrochemical measurements. The Pt-OP electrodes were characterized using CV in 0.1 or 0.2 M aqueous H_2SO_4 solution (Fisher Scientific, ACS Grade) prepared with high purity water (18.2 MΩ cm). Cyclic voltammetry profiles over a potential region of 0.05 to 1.25 V vs. RHE encompass the region of underpotential deposition of hydrogen (H_{UPD}) and oxide formation and reduction.(Jerkiewicz, 2010; Jerkiewicz, et al., 2004) Because CV features in this potential range are sensitive to trace amounts of impurities and the surface orientation of the Pt electrode, this CV analysis allowed us to evaluate the purity of the system and to identify any preferential Pt grain orientation. The $\boldsymbol{A}_{ecsa}$ of the Pt-OP electrodes was determined by integrating the H_{UPD} (~0.05 – 0.45 V vs. RHE) and dividing this by the charge density (~0.05 – 0.45 V) of 210 µC cm^{-2}, which corresponds to the adsorption of a monolayer of H_{UPD}.(D. Chen, et al., 2011; Woods, 1974)

2.4. Results and Discussion

A series of electrodes with different thicknesses were made in order to systematically evaluate their three-dimensional interconnectivity, stability and electrochemical characteristics. All samples were made in triplicate to evaluate the reproducibility of the preparation methods and their electrochemical responses. A terminology was developed to describe the Pt-OP samples, corresponding to the approximate thickness of the Pt deposit within the sacrificial template of PS spheres (Fig. 2.1). For example, a “type 1/3” Pt electrode contains a uniform deposit with a thickness of ~1/3 the height of a single PS sphere in a close packed arrangement. Due to the thickness of the deposit, the “type 1/3” structure is non-porous and simply presents an electrode with a designed roughness. A “type 3/4” sample corresponds to uniform Pt deposit with a thickness equivalent to ~3/4 the height of a PS sphere in a close packed arrangement. The three dimensional (3D) porous structure of the “type 3/4” electrode contains interconnecting pores with circular openings on top. A “type 1¾” sample corresponds to uniform Pt deposit with a thickness equivalent to ~7/4 of the height of a single PS sphere in the prepared template. The 3D porous structure of the “type 1¾" electrode contains two porous layers. The first layer consists of interconnected spherical pores. The second layer contains interconnected pores with circular openings on top. The first and second layers are also interconnected, thus facilitating both vertical and horizontal penetration and diffusion by a fluid. This series of samples were chosen in order to evaluate diffusion of electrochemically active species within the porous structure as a function of dramatic changes in RF between the sample types, as well as to demonstrate the modularity and reproducibility of this method of preparing 3D Pt-OP electrodes.

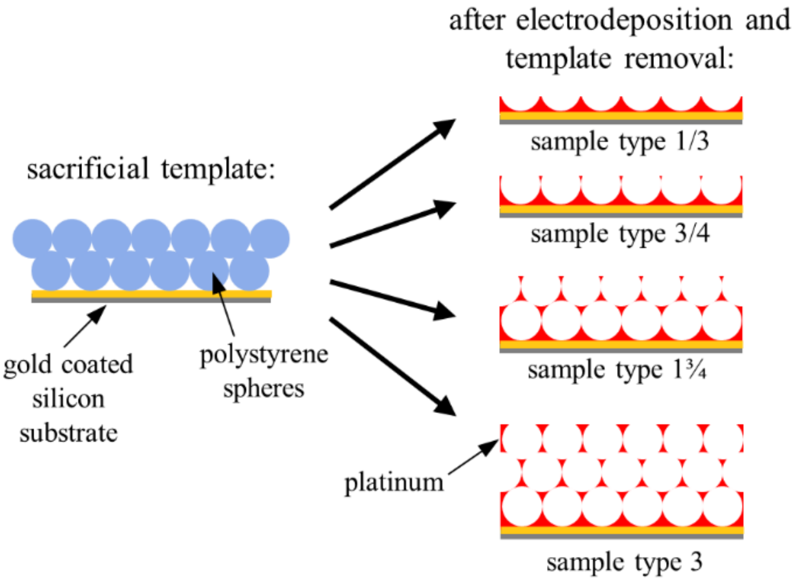

Figure 2.1 **Schematic of the process used to prepare OP-Pt electrodes of varying thickness/porosity.**

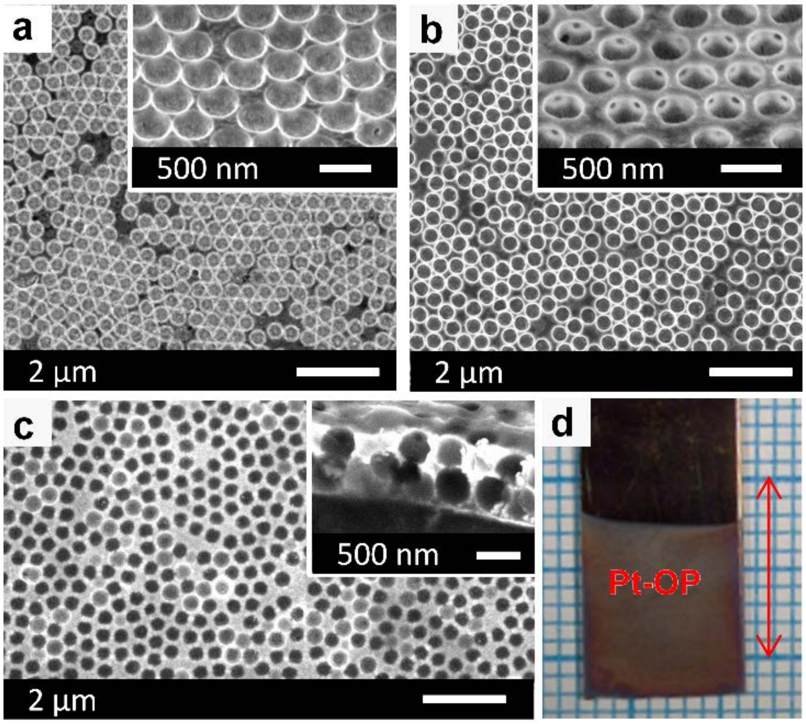

Figure 2.2 **Scanning electron microscopy (SEM) images of representative samples for each type of Pt-OP electrode: (a) sample type 1/3 (inset, viewed at a 45° tilt); (b) sample type 3/4 (inset, viewed at a 45° tilt); and (c) sample type 1¾ (inset, viewed at a 60° tilt). (d) Optical micrograph of a typical Pt-OP electrode with a length of 1 cm indicated by the arrow on the grid behind the sample.**

Dimensions and film morphology of each electrode were evaluated by SEM analysis, and typical images from this inspection are presented in Fig. 2.2. The pore size formed by selective removal of the spherical PS templates was determined by measuring the distance between the middle of two adjacent, connected pores. Several measurements were taken and an average pore diameter was found to be 444 ± 16 nm. It is important to add that the pore size can be controlled by varying the diameter of the spherical PS particles assembled in the sacrificial template. The focus of this study is, however, on the systematic comparison of varying thickness and porosity of Pt electrodes with a well-defined pore shape, size and connectivity. Our results shown in Fig. 2.2 demonstrate that our PS sphere templates are non-perfect and contain structural defects. In some regions, we observe a perfect hexagonal close-packed arrangement with each PS sphere having a point contact with 6 others. In other regions there are, however, spheres in contact with fewer neighbouring spheres. A lack of contact with neighbouring spheres can result in a lack of interconnectivity, which can translate into a decrease in RF and limitations in the horizontal fluid flow between adjacent pores. The interconnection size (the degree of overlap of adjacent PS spheres) is generally determined by the hardness and degree of close packing of the spherical PS templates.(Xia, Gates, Yin, & Lu, 2000) The average diameter of the circular interconnection between adjacent pores in our Pt-OP electrodes was found to be 120 ± 10 nm, as determined from cross-sectional SEM measurements of openings between adjacent pores. This interconnection size could limit penetration of the electrolyte into underlying porous layers, which is considered later in our discussion. To evaluate bulk interconnectivity we have counted the number of pores in an as-prepared single layer electrode (e.g., the number of pores per cm^2) and compared it to the theoretical number of pores per cm^2 for a homogeneously close-packed single layer structure. From this comparison, we have determined that <4% of spheres were missing from the total number of spheres that could be assembled into a single layer with a hexagonal close packed structure. Based on this information, further improvements to the assembly of PS spheres could only increase the observed RF by <4%. Furthermore, the interconnectivity was evaluated by counting the average number of neighboring pores connected to an individual pore (as visible in SEM imaging). In a uniformly close-packed structure of assembled PS spheres each pore is connected to six adjacent pores arranged in a hexagonal array within the OP electrode. For our samples, we found that each pore in the Pt-OP electrodes is, on average, connected to four adjacent spherical pores. Therefore, these structures have a considerably high density of connected pores and we believe that horizontal fluid flow should not be significantly limited. Overall, the OP-electrodes were determined to have suitable pore sizes, density and connectivity for our electrochemical studies.

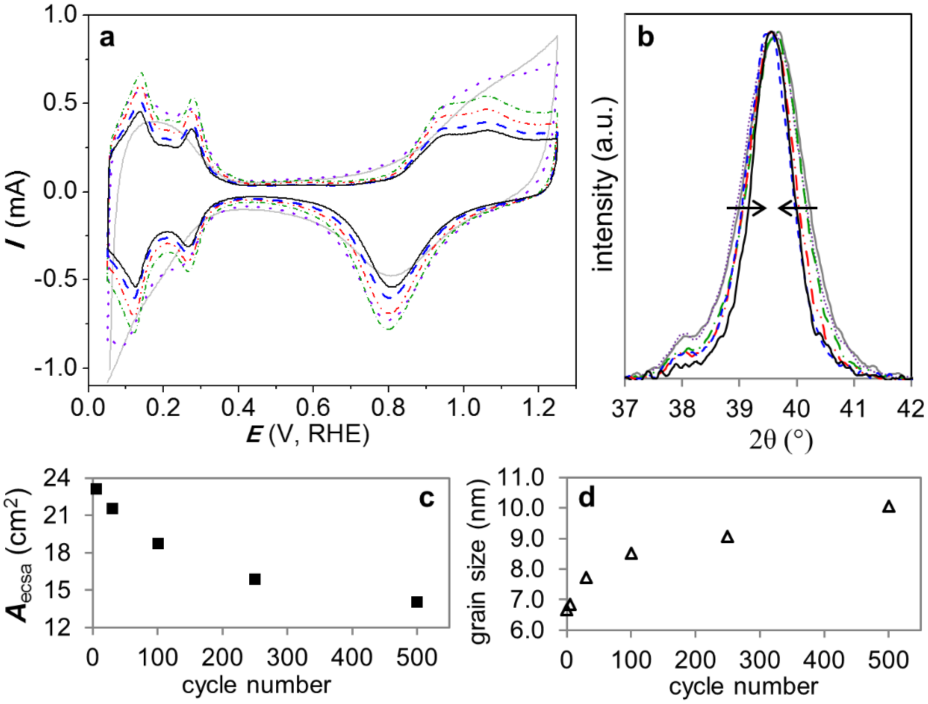

Figure 2.3 **Evaluation of the electrochemical and structural stability of Pt-OP structures at regular intervals after a series of continuous CV scans from 0.05 to 1.25 V (vs. RHE) at a rate of 25 mV s^{-1}. (a) Cyclic voltammetry traces and (b) normalized X-ray diffraction peak of Pt(111) each assessed at regular intervals during the potential cycling: 1 cycle (——); 5 cycles (· · · · ·); 30 cycles (-·-·-); 100 cycles (-··-··); 250 cycles (– – –); and 500 cycles (——). (c) Plot of A_{ecsa} as a function of cycle number. (d) Plot of crystal grain size, estimated from the XRD data, as a function of the number of electrochemical cycles.**

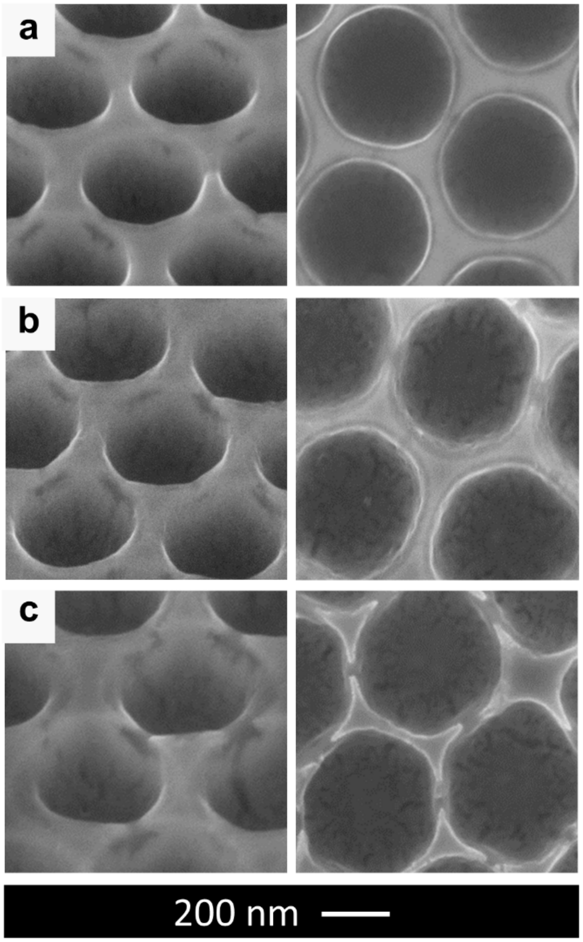

Figure 2.4 **(a-c) High-resolution SEM images acquired at a 45° tilt away from the normal to the surface (left column) and perpendicular to the surface (right column): (a) before cycling; (b) after 100 cycles; and (c) after 500 total cycles. All scale bars are 200 nm.**

We analyzed the electrochemical characteristics of Pt-OP electrodes by recording CV profiles in the potential range corresponding to H_{UPD} adsorption and desorption,(Jerkiewicz, 2010) and PtO formation and reduction.(Jerkiewicz, et al., 2004) Fig. 2.3a shows CV profiles for a Pt-OP electrode in 0.1 M H_2SO_4 recorded at a scan rate (*s*) of 25 mV s^{-1} that is representative of the overall trend observed in 500 transients. The initial scan contains ill-defined peaks in both the H_{UPD} region (0.05 – 0.4 V vs. RHE) and PtO region (0.7 – 1.25 V vs. RHE). The initial shape of the CV profile in the oxide formation region is characteristic of carbon based contamination on the Pt-OP electrode that undergoes oxidative desorption upon prolonged potential cycling.(Conway, et al., 1973) After 30 cycles the CV features corresponding to H_{UPD} adsorption and desorption, as well as PtO formation and reduction, are well-defined and characteristic of an impurity-free system. Further potential cycling (100, 250 and 500 cycles) does not change the shape of the CV features, but decreases their current density values. This observation indicates that there are no structural changes in the Pt deposit, but that $\boldsymbol{A}_{\text{ecsa}}$ is gradually reduced. Integration of the CV features corresponding to H_{UPD} adsorption allows us to determine $\boldsymbol{A}_{\text{ecsa}}$ as a function of the cycle number (Fig. 2.3b). An analysis of the $\boldsymbol{A}_{\text{ecsa}}$ values demonstrates a gradual decrease of $\boldsymbol{A}_{\text{ecsa}}$ up to nearly 40%. The decrease in $\boldsymbol{A}_{\text{ecsa}}$ may be assigned either to surface restructuring of Pt-OP or Pt electro-dissolution.(Tremiliosi-Filho, Jerkiewicz, & Conway, 1992) However, CV experiments alone do not allow us to distinguish the process responsible for $\boldsymbol{A}_{\text{ecsa}}$ loss and complementary analyses (e.g., X-ray diffraction, electron microscopy) are necessary.

To better identify the phenomena responsible for the loss of $\boldsymbol{A}_{\text{ecsa}}$ we removed the Pt-OP electrodes from the electrolyte solution, rinsed with high purity water and analyzed these samples by both XRD (Fig. 2.3c and 2.3d) and SEM (Fig. 2.4). We monitored changes in the full-width-at-half maximum of the XRD peak corresponding to Pt (111) and used this value to calculate the grain size of Pt using the Scherrer formula.(Holzwarth & Gibson, 2011) The results demonstrate that the average grain size gradually increases upon potential cycling by up to 35% (Fig. 2.3d). Additionally, this change occurs in good correspondence with the observed loss in $\boldsymbol{A}_{\text{ecsa}}$ (Fig. 2.3b). Analysis of the Pt-OP electrodes by SEM reveals corresponding changes in morphology. The Pt-OP deposits initially have spherically shaped openings with smooth Pt walls (Fig. 2.3e). Scanning electron microscopy examinations of these porous electrodes after CV analysis indicate a change to both the texture and shape of the pores. After 100 cycles the walls separating spherical pores become thinner and the shape less spherical (Fig. 2.3f). These changes are even more pronounced after ~500 cycles (Fig. 2.3g). In addition, potential cycling of Pt-OP for a total of 500 times leads to further thinning of the walls and generates vertical cracks between pores. The observed changes in SEM can be quantified by measuring changes in the area of the upper pore opening (leading into the Pt-OP electrodes) observed by SEM without tilting the stage (Fig 2.4). This analysis reveals that the average upper pore opening increased from $1.16 \pm 0.02 \times 10^5$ nm^2 with no cycling, to $1.40 \pm 0.08 \times 10^5$ nm^2 after 100 cycles, and to $1.57 \pm 0.04 \times 10^5$ nm^2 after 500 cycles. Altogether, the CV, XRD, and SEM results allow us to conclude that the loss in $\boldsymbol{A}_{\text{ecsa}}$ is most likely due to Pt electro-dissolution and re-deposition (Ostwald ripening). We hypothesize that the outermost layer of Pt is dissolving from the surfaces of the Pt-OP electrodes, and that the outermost layer is composed of Pt with a grain size smaller than that of the underlying layers of Pt. This outer layer of Pt is also most likely less dense and, therefore, more porous than the underlying layers. Removal of the outermost layers of Pt from the Pt-OP electrodes would thus expose a dense, underlying film of Pt composed of larger Pt grains, as well as a more stable $\boldsymbol{A}_{\text{ecsa}}$ and electrochemical response.(Topalov, et al., 2012) In later studies, it will be important to examine whether electro-dissolution of Pt-OP is uniform throughout the porous structure and to evaluate methods for reducing Pt loss, such as thermal annealing to induce grain growth within the Pt electrode before electrochemical testing.

A systematic study was performed to compare three different types of Pt-OP electrodes. As depicted in Fig. 2.1, these three electrodes were films of type 1/3, 3/4, and 1¾. In Fig. 2.5a, we present three representative CV profiles for the three types of Pt-OP electrodes after reaching a point at which the respective CV profiles do not change significantly (typically after 200 cycles). These CV profiles have been normalized by their measured geometric surface area ($\boldsymbol{A}_{\text{geom}}$) as described in the experimental section. Similar to that observed for the Pt-OP electrode described above, CV profiles underwent transformations with continued cycling corresponding to the initial removal of surface contaminants followed by Pt dissolution. The CV profiles demonstrate that all three systems are impurity-free (after initial cycling to remove carbon based surface contaminants) and again the features for H_{UPD} adsorption and desorption can be used to determine $\boldsymbol{A}_{\text{ecsa}}$. Triplicates of each sample type were prepared and analyzed in the same manner for a statistical comparison of the results reported on these structures. Fig. 2.5b presents the experimental RF ($RF_{\text{exp}} = \boldsymbol{A}_{\text{ecsa}} / \boldsymbol{A}_{\text{geom}}$) values for the three types of Pt electrodes and reveals that RF_{exp} increases with increased OP thickness and thus with the Pt loading. The RF_{exp} values were 18.3 ± 1.9, 24.9 ± 0.5, and 30.3 ± 1.0 for type 1/3, 3/4, and 1¾ samples, respectively. The Pt-OP electrodes were prepared reproducibly as indicated by the relatively small error bars associated with each type of electrode. The progressive increase in RF_{exp} with sample thickness provides evidence that the electrolyte can traverse the open pore structure through the ~120 nm diameter interconnects. As mentioned earlier, the interconnectivity of these porous electrodes—as determined by their dimensions, overlap of the spherical templates, and thickness of the electrode could limit vertical and horizontal transport within these materials. These are variables that could be analyzed in the future using similar Pt-OP electrodes, but are beyond the current study of developing and characterizing these electrodes as a platform for further fundamental studies.

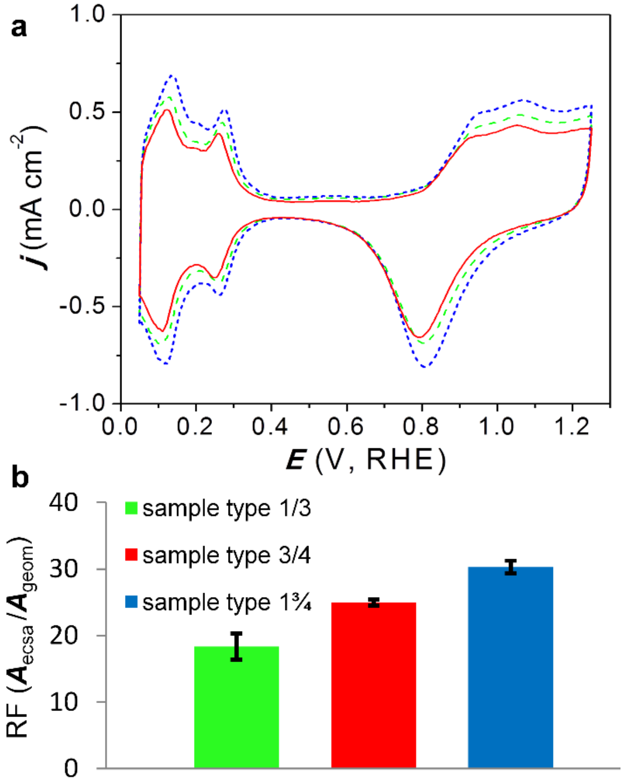

Figure 2.5 **(a) Representative cyclic voltammogram traces that have been normalized to A_{geom} for samples of type 1/3 (——); type 3/4 (- - -); and type 1¾ (----). (b) Bar graph illustrating the roughness factor (RF) for each sample type, where RF corresponds to A_{ecsa}/A_{geom}. Error bars corresponding to each Pt-OP thickness (or sample type) indicate the standard deviation in RF as calculated from the analysis of three independent samples.**

The controlled porous nature of the Pt-OP electrodes is an essential factor for establishing a platform for further fundamental electrochemical studies. The structure of and connection between the pores of the Pt-OP electrodes help to define the RF_{exp} for each type of electrode. The reported RF_{exp} in Fig. 2.5 was determined by dividing the measured $\boldsymbol{A}_{ecsa}$ by the two dimensional area of the electrode covered by these Pt-OP structures ($\boldsymbol{A}_{geom}$). To better evaluate the micro- and nano- roughness of the Pt surfaces within the porous structure, it is necessary to consider the geometric surface area within the Pt-OP electrodes formed by the network of interconnected pores ($\boldsymbol{A}_{\text{pore-geom}}$); where $\boldsymbol{A}_{\text{pore-geom}}$ is a theoretical representation of the porous structures, lacking micro, or nano-pore surface roughness. The $\boldsymbol{A}_{\text{pore-geom}}$ has been estimated (Eq. 1) by evaluating the average pore radius (r_{pore}), density of the pores (ρ_{pore}, pores per cm^2), and average thickness of the electrochemically deposited Pt electrode ($t_{\text{electrode}}$), as measured by the number of porous layers (e.g., $t_{\text{electrode}}$ is 1/3 for sample type 1/3), from SEM analysis.

$$\boldsymbol{A}_{\text{pore-geom}} = 4\pi(r_{\text{pore}})^2 \times \rho_{\text{pore}} \times t_{\text{electrode}} \tag{1}$$

Average pore density within the Pt-OP samples was determined to be $4.91 \pm 0.02 \times 10^8$ pores per cm^2. For the sample type 1¾, the pore density is assumed to be double that for the single layer structures as a function of our assembly method. We were unable to accurately determine the pore density of the bottom layer within these Pt-OP electrodes by SEM as it is covered by a continuous top layer of porous Pt. If the Pt electrodes have no micro- or nano- surface roughness, then we would expect the theoretical roughness factor ($\text{RF}_{\text{pore-geom}}$ or $\boldsymbol{A}_{\text{pore-geom}}/\ \boldsymbol{A}_{\text{geom}}$) to be similar to RF_{exp}. Using the method described above, $\text{RF}_{\text{pore-geom}}$ was calculated to be 1.02 ± 0.01, 2.29 ± 0.01, and 5.34 ± 0.02 for sample type 1/3, 3/4, and 1¾, respectively. We also determined the real surface roughness (RF_{real}) – defined as $\boldsymbol{A}_{\text{ecsa}}/\ \boldsymbol{A}_{\text{pore-geom}}$ – that is correlated with the micro- and nano- scale surface roughness of the Pt surfaces within the Pt-OP electrodes (Table 2.1). If the surfaces of the porous electrodes were atomically smooth, and if all Pt surfaces were in contact with the electrolyte, RF_{real} would be equivalent to a value of 1. For our Pt-OP electrodes, the average RF_{real} was 11.4, demonstrating that micro- and nano- roughness of the Pt surfaces within the porous structure contributes significantly to the total $\boldsymbol{A}_{\text{ecsa}}$. In addition, the RF_{real} decreases with increasing thickness of the Pt-OP electrodes from 17.6 ± 1.9 for sample type 1/3, to 10.9 ± 0.4 for sample type 3/4, and 5.6 ± 0.2 for sample type 1¾. This trend agrees with observations made in the structural and electrochemical analyses by SEM and CV of the Pt-OP electrodes. For example, the analysis by SEM of sample type 1/3 electrodes indicates that they are largely composed of a thin, roughened Pt film (lacking any well-defined 3D porous structure). Moreover, the sample type 1/3 electrodes have a comparable RF_{exp} to that of a Pt electrodeposited film prepared without the use of the sacrificial PS templates. Thin Pt electrodes derived without the use of a sacrificial template displayed RF_{exp} values ranging between 12 and 17, depending on the Pt loading. This comparison suggests that the outermost surfaces of electrodeposited Pt have high surface roughness, but that Pt deposited against the spherical PS templates is comparably smooth. Therefore, future studies could greatly enhance the $\boldsymbol{A}_{ecsa}$ by producing roughened Pt surfaces within the spherical pores of thick Pt-OP electrodes.

Table 2.1 Summary of RF values obtained from analysis of the series of Pt-OP electrodes.

Sample Type	RF_{exp} ($\boldsymbol{A}_{ecsa}/\boldsymbol{A}_{geom}$)	$RF_{pore\text{-}geom}$ ($\boldsymbol{A}_{pore\text{-}geom}/\boldsymbol{A}_{geom}$)	RF_{real} ($\boldsymbol{A}_{ecsa}/\boldsymbol{A}_{pore\text{-}geom}$)
1/3	18.3 ± 1.9	1.02 ± 0.01	17.7 ± 1.9
3/4	24.9 ± 0.5	2.29 ± 0.01	10.9 ± 0.4
1¾	30.3 ± 1.0	5.35 ± 0.02	5.6 ± 0.2

We prepared a thicker Pt-OP electrode to further explore the trend of electrochemical enhancement as it correlates with Pt-OP electrode thickness. This analysis also demonstrated the utility of our methods to make customized Pt-OP electrodes. For this study, we prepared a 3 layer Pt-OP electrode. These samples, referred to as a sample type 3, were characterized by SEM and CV analysis. The relatively thick Pt-OP electrodes contain cracks, as seen in the SEM images, which most likely develop due to relaxation of strain within the samples upon removal of the PS templates.(Gates, Yin, & Xia, 1999) These cracks are not regarded as detrimental to the functionality of the porous electrode, and could increase the porosity of, and thus accessibility of electrolyte into, these structures. The shape of the CV profiles for this thicker sample is comparable to the other Pt-OP electrodes, indicating relatively clean Pt surfaces. This sample exhibited an RF_{exp} of 55 ± 0.1 after stabilization of the CV profiles, which is approximately twice that of the value measured for sample type 1¾ electrodes. A comparison of this enhancement factor to that observed for the other sample types suggests that the cracks within these Pt-OP electrodes do not add significantly to the measured $\boldsymbol{A}_{ecsa}$. The Pt mass per $\boldsymbol{A}_{geom}$ of the sample type 3 was determined by FAAS to be 340 ± 60 μg Pt per cm^2. The ratio of $\boldsymbol{A}_{ecsa}$ to Pt mass for this sample is 16.2 m^2 per gram of Pt. Interestingly, this value of $\boldsymbol{A}_{ecsa}$ per gram of Pt is well within the range of those reported by 3M for their NSTF catalyst layers used for ORR electrocatalysis (e.g., from 5 to 17 m^2 per gram of Pt).(Mark K. Debe, 2012) In addition, our 3 layer Pt-OP electrode is comparable to previous reports on relatively thick, ordered porous Pt. For example, the preparation of a Pt-OP electrode using a template of silica spheres produced an electrode with a roughness factor of nearly 60 for a Pt mass of 532 µg per cm^2 ($\boldsymbol{A}_{\text{geom}}$).(Y. Liu, et al., 2007) This yields a surface area enhancement of 11.3 m^2 ($\boldsymbol{A}_{\text{ecsa}}$) per gram of Pt, which is comparable to the values observed for our samples. Variance between our results and those previously published are most likely the result of differences in electrode thickness, Pt surface roughness, and template sphere size. The potential use of Pt-OP electrodes as electrocatalysts is demonstrated in part by their comparable surface area enhancement with current catalysts layers being pursued for industrial applications.

2.5. Conclusions

Platinum ordered porous electrodes were reproducibly prepared and characterized by electrochemical techniques. These ordered electrodes serve as a reproducible platform for evaluating the efficiency and stability of electrochemical processes that are relevant to understanding the dynamics and optimization of Pt electrocatalysis. The Pt-OP electrodes contained pores with regular dimensions, shapes, and connectivity, in addition to a well-defined thickness and roughness of the Pt surfaces. The Pt-OP electrodes are made by electrodeposition of Pt within a sacrificial template of self-assembled polystyrene spheres, followed by the selective removal of this polymer with toluene. A series of electrodes with specific pore sizes, interconnectivity, and thickness were prepared in order to evaluate their electrochemical performance as a function of changes in the Pt-OP electrode thickness. These Pt-OP electrodes were characterized by electron microscopy, X-ray diffraction and cyclic voltammetry to evaluate the relationship between structure and electrochemical activity of these materials. The $\boldsymbol{A}_{\text{ecsa}}$ is reproducibly modified as a function of thickness of the porous electrodes. The micro- and nano- scale roughness of the Pt-OP electrodes was estimated by comparing the measured $\boldsymbol{A}_{\text{ecsa}}$ to the expected $\boldsymbol{A}_{\text{ecsa}}$ based on morphology of the porous electrodes. This comparative analysis demonstrated that micro- and nano-roughness of the Pt surfaces within the Pt-OP electrodes contributes significantly to the measured $\boldsymbol{A}_{\mathrm{ecsa}}$. The combined results of the CV, XRD, and EM analyses suggest that the surface roughness of the Pt-OP electrodes is non-uniform. The inside of the spherical pores were smooth relative to the top surfaces of the electrodeposited platinum. The regularity of the Pt-OP electrodes was an essential component of also evaluating changes to the electrode surfaces as a function of sequential CV analyses. The prepared electrodes have comparable electrochemical activity to other porous platinum electrodes demonstrated in the literature. In fact, a Pt-OP electrode composed of three layers of interconnected spherical pores and a nominal diameter of ~444 nm have a comparable $\boldsymbol{A}_{\mathrm{ecsa}}$ per gram to electrodes being pursued for the commercial application of low temperature fuel cells. The Pt-OP electrodes described in this study could have further applications in optimizing the efficiency and monitoring the long-term stability of Pt in these and other electrocatalytic applications. In expanding on this work, we aim to prepare composite OP electrodes, whereby Pt NPs decorate the surface of an OP electrode composed of a different material (support@PtNP OP electrodes). The use of alternative support materials, instead of pure Pt, is expected to increase the SSA of Pt. In addition, support materials such as Au can enhance the electrocatalytic activity and stability of Pt NPs.(M. Shao et al., 2010; J. Zhang, et al., 2007; Q. Zhang et al., 2013)

Chapter 3.

Preparation of Nanoparticle Decorated Polystyrene Spheres

3.1. Notice of Permissions

The following chapter is based upon work recently accepted for publication: Brandy K. Pilapil, Michael C. P. Wang, Michael T. Y. Paul, Amir Nazemi and Byron D. Gates, "Self-assembly of nanoparticles onto the surfaces of polystyrene spheres with a tunable composition and loading" Nanotechnology (NANO-105201). Permission to use the following material has been granted by all co-authors and the publisher allows for use of the published material (in part or in full) in a research thesis or dissertation. Michael Wang performed XPS and electron diffraction analysis; Michael Paul and Amir Nazemi assisted with NP synthesis. All other experiments have been performed by myself.

A related study previously published is worth noting here, but is not reported on specifically in this thesis because it is not relevant to the central electrocatalysis theme of this thesis work: Brandy Kinkead, Abdiwali A Ali; John-Christopher Boyer, and B. D. Gates, "Optically active nanoparticle coated polystyrene spheres" MRS Online Proceedings Library 2013, 1546.

3.2. Context of Work

The preparation of composite support@NP OP electrodes was sought through the use of NP decorated PS sphere (PS@NPs) templates, followed by assembly into ordered arrays (Appendix A) and infiltration with a secondary support, as per Fig. 3.1 below. This chapter details the method for preparation of the PS@NPs with the ability to tune NP loading and composition. In this method, NPs are first synthesized to be a desired shape and size, before self-assembly onto the PS sphere surfaces. The ability to fine tune the decoration of catalytically active NPs onto the surface of PS spheres enables the preparation of a wide array of different support@NP-OP electrodes with control over NP surface loading and NP-NP spacing, while preserving shape, size and composition of the NPs. Use of these NP decorated PS spheres for heterogeneous catalysis is also explored to provide necessary insights into the stability of the coatings for further application (e.g., as templates for the preparation of support@NP OP electrodes).

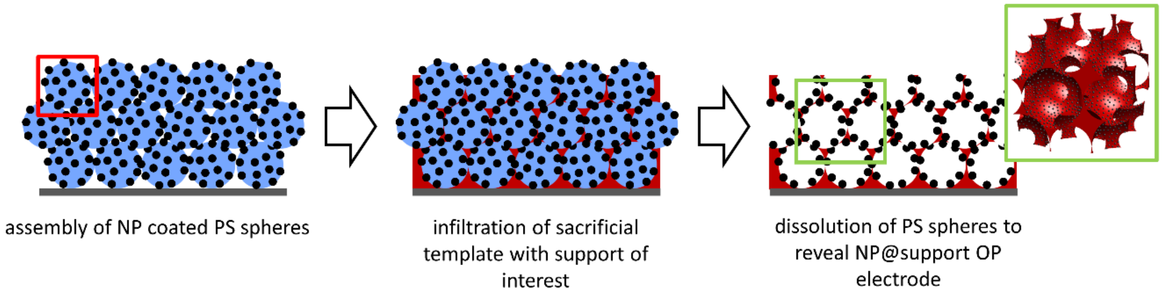

Figure 3.1 **Schematic illustrating the use of NP coated PS spheres in the preparation of support@NP-OP electrodes. The red box indicates a single NP coated PS sphere within the sacrificial template. The green box indicates a region which could represent the three-dimensional inset (outlined in green) of a section of a support@NP-OP electrode.**

3.3. Introduction

A versatile method for the preparation of nanoparticle (NP) decorated polystyrene (PS) spheres has been sought by a number of researchers due to the broad applicability of these materials in areas such as environmental catalysis, and contrast agents in biological imaging.(Bell, 2003; Cao et al., 2009; Chave, Grunenwald, Ayral, Lacroix-Desmazes, & Nikitenko, 2013; C.-W. Chen, Serizawa, & Akashi, 2002; Chia-Wei, Tseng, Shu-Fen, Yeu-Kuang, & Chung-Kwei, 2012; Dokoutchaev et al., 1999; A. G. Dong et al., 2002; Johnston, 2012; D.-W. Kim, Lee, Oh, Kim, & Oh, 2006; J.-H. Lee, Mahmoud, Sitterle, Sitterle, & Meredith, 2009; J.-M. Lee, Jun, Kim, Lee, & Oh, 2009; K. Lee, Kim, & Kim, 2010; Yunxing Li et al., 2012; Yunxing Li et al., 2011; Yimin Li &

Somorjai, 2010; Yoon, Choi, & Cho, 2013; Jianan Zhang et al., 2011; M. Zhang et al., 2013) These methods have, however, had a limited success in preparing NP decorated PS spheres from NPs of a diverse range of compositions, and in controlling the uniformity and loading of the NPs over the surfaces of the support. Herein, we describe a method for the preparation of NP decorated PS spheres (PS@NPs) assembled from NPs of a diverse range of compositions, sizes and shapes. Through this method we are also able to control the quantity of NPs, spacing between these particles within the assembled shells, and relative ratios of NPs of different compositions within a multi-component shell. This report demonstrate the preparation and fine tuning of multi-component PS@NPs for the first time. The NP decorated PS spheres retain their colloidal stability over the course of multiple solution based catalytic reactions. The ease in tuning this method to prepare a wide range of PS@NPs is attributed to the versatility of our approach, using polyvinylpyrrolidone (PVP) stabilized NPs that have favorable interactions with the functionalized PS spheres.

3.4. Experimental

3.4.1. Synthesis of Platinum Nanoparticles

Platinum nanoparticles were synthesized by ethanol reduction.(Teranishi, Hosoe, Tanaka, & Miyake, 1999) Polyvinylpyrrolidone (PVP) (55k MW, 98%) and hexachloroplatinic acid (H_2PtCl_6, ACS grade) were purchased from Sigma-Aldrich. Anhydrous ethyl alcohol (EtOH) was purchased from Commercial Alcohols. All chemicals were used as received, without any further purification. All glassware and stir bars were treated with aqua regia and piranha prior to use. The aqua regia solution was prepared from a 3:1 (v/v) solution of hydrochloric acid (36.5 – 38.0% in water; Anachemia Inc.) and nitric acid (68 – 70% in water; Anachemia Inc.). The piranha solution was prepared from a 5:2 (v/v) solution of concentrated sulfuric acid (90 - 100% in water; Anachemia Inc.) and hydrogen peroxide (30% in water; Caledon Laboratories Ltd.). *CAUTION: Aqua regia and piranha solutions should be handled with extreme care.* Briefly, 5.0 mL of 6 mM H_2PtCl_6 was prepared one day in advance in demineralized water (18 MΩ·cm, produced using a Barnstead NANOpure DIamond water filtration system). A solution of 40 mL EtOH, 5 mL demineralized water, and 1.65 g 55k MW PVP was prepared and stirred for 10 min in a 100 mL round bottom flask equipped with a reflux condenser and stir bar. The 6 mM H_2PtCl_6 solution was then added to the EtOH mixture and the resulting solution was heated to reflux under continuous stirring. After 3 h at reflux under continuous stirring, the mixture was removed from heat and slowly cooled to room temperature. The resulting solution of Pt NPs was directly used for coating onto the PS spheres without any purification.

3.4.2. Synthesis of Palladium Nanoparticles

Nanoparticles of Pd were synthesized by reduction in ethylene glycol (EG).(Xiong et al., 2005) Glassware and stir bars were treated with aqua regia and piranha prior to use, as described above. Ethylene glycol (Caledon Laboratories Inc.), 55k MW PVP (98%; Sigma-Aldrich) and sodium tetrachloropalladate(II) (98%; Sigma-Aldrich) were purchased and used without further purification. Five mL of EG was added to a 25 mL round bottom flask equipped with a condenser and stir bar and heated to 110°C for 1 h with continuous stirring. Fresh solutions of 55k MW PVP (0.080 g) in EG (3 mL) and Na_2PdCl_4 (0.138 g) in EG (3 mL) were prepared during this time. After the 1 h had passed, both EG solutions were simultaneously injected into the hot EG at a rate of 45 mL/min. The reaction mixture was held at 110°C for an additional 3 h before cooling slowly to room temperature. The resulting product was washed once with ~ 50 mL of acetone, isolated by centrifugation and redispersed in 50 mL of EtOH for use in coating of the PS spheres.

3.4.3. Synthesis of FePt Nanoparticles

The FePt NPs were prepared by polyol reduction in dioctyl ether, as per literature.(S. Sun, Murray, Weller, Folks, & Moser, 2000) Platinum(II) acetylacetonate (acac) (97%, Sigma-Aldrich), iron pentacarbonyl (97%, Sigma-Aldrich), 1,2 hexadecanediol (>98%, TCI America), dioctyl ether (99%, Sigma-Aldrich), oleic acid (>98%, Sigma-Aldrich), oleylamine (70%, Sigma-Aldrich), toluene (Anachemia Inc.), 10k MW PVP (Sigma-Aldrich), dichloromethane (DCM) (Anachemia Inc.), dimethylformamide (DMF) (Anachemia Inc.), diethyl ether (Anachemia Inc.) and chloroform (Anachemia Inc.) were all purchased and used as-recieved without any further purification. All glassware and stir bars were treated with aqua regia and piranha prior to use, as described above. Briefly, a 20 mL solution of Pt(acac) (0.5 mM) and 1,2 hexadecanediol (1.5 mM) in dioctyl ether was heated to 100°C with continuous stirring under N_2 atmosphere in a 100 mL round bottom flask equipped with a reflux condenser and stir bar. Once all material appeared to be dissolved at 100°C (e.g., 5 min), 0.16 mL of 0.5 mM oleic acid in dioctyl ether and 0.17 mL of 1 mM oleylamine in dioctyl ether were added to the heated mixture. Finally, 0.13 mL of 1 mM $Fe(CO)_5$ was quickly injected. The reaction mixture was heated to 300°C for 30 min while stirred continuously. The resulting mixture was cooled to room temperature before the product was isolated via centrifugation. The FePt NP product was washed 3 times by dispersing in hexanes, subsequently precipitating the NPs with ethanol and isolating the solid product by centrifugation. The purified FePt NPs were transferred to the aqueous phase as described below.(Johnson, Sangeetha, Boyer, & van Veggel, 2010) A dispersion of the purified FePt NPs in chloroform was added to a 50 mL round bottom flask equipped with a stir bar, followed by 5 mL each of DCM and DMF. This reaction mixture was stirred while adding 150 mg of 10k MW PVP. Once the PVP appeared to be dissolved (e.g., 15 min), the mixture was refluxed for 12 h with continuous stirring. The reaction solution was subsequently cooled to RT, and the PVP-coated NPs selectively precipitated by addition to diethyl ether (90 mL) via Pasteur pipette. The NPs were isolated by a centrifugation process, and the resulting pellet of NPs redispersed in ethanol for use in coating the PS spheres. Based on selected area electron diffraction analysis, these NPs are suspected to be an alloy of Fe and Pt (see Appendix C for details).

3.4.4. Preparation and Characterization of Nanoparticle Decorated Polystyrene Spheres

The NP decorated PS spheres were prepared by combining the synthesized NPs with amine functionalized PS spheres (Polysciences, Inc. or Bangs Laboratories, Inc.). Before use, the PS spheres were washed once with a 1:1 (v/v) mixture of EtOH and water, and isolated via centrifugation. In a typical experiment, NP coatings were prepared by combining 1 to 10 mL of the synthesized NPs with 40 to 500 mg of the washed PS spheres. The pH of the reaction was adjusted by addition of 1% HCl, prepared by dilution of concentrated HCl (Anachemia, ACS Reagent Grade) with demineralized water (18 MΩ•cm, produced using a Barnstead NANOpure DIamond water filtration system), for coating the FePt NPs onto the PS spheres. This step was not necessary for Pd or Pt NP coatings since the pH of these solutions was near pH 3 as a result of their synthetic methods. This mixture of particles was continuously stirred at 55°C for 3 h. After 3 h of heating, the NP decorated PS spheres were slowly cooled to room temperature and isolated via centrifugation. To purify the PS@NPs from any residual suspension of NPs, the isolated pellet was washed twice in water and twice in ethanol. In between each wash step, the PS@NPs were isolated via centrifugation for ~10 min at 10,000 rpm.

The purified samples of PS@NPs were analyzed by TEM using using either a FEI Tecnai G2 field emission or a FEI Osirus X-FEG scanning/TEM operated at an accelerating voltage of 200 keV. Energy dispersive X-ray spectroscopy (EDS) analysis was performed on the FEI Osirus X-FEG scanning/TEM, which is equipped with a Super-X EDX detection system. X-ray photoelectron spectroscopy was performed with a Kratos Analytical Axis Ultra DLD spectrometer using a monochromatic aluminum source (Al Kα, 1486.6 eV) operating at 150 W (10 mA emission current and 15 kV HT). Fourier transform infrared spectroscopy (FTIR) analysis was performed using a Perkin Elmer Spectrum Two ATR FTIR spectrometer. Sample solutions in ethanol were drop cast onto the single reflection diamond sample window and the ethanol allowed to evaporate prior to obtaining an FTIR spectra.

The number of NPs per PS sphere was determined by analysis of TEM images. Nanoparticles on both the upper and under side of the PS spheres were visible near to the edges of the PS spheres, due to less interaction of PS with the electron beam. Therefore, the total number of NPs per sphere was determined by dividing the spheres into a central and an outer region (see Appendix C for details). The number of NPs was then counted in each region and the total number of NPs estimated by doubling the number of NPs counted in the central region (to account for NPs not seen in this TEM analysis) and adding that to the number obtained for the region outside the red circle. The central region was defined as the region where the apparent NP density decreased significantly in comparison to the outer region. The difference in contrast between neighbouring NPs in this central region was also less than near the edge of the PS spheres. Reported errors correspond to one standard deviation as determined from the NP coatings on three isolated PS spheres.

The catalytic activity of FePt NP decorated PS spheres was evaluated by studying the catalytic degradation of azo dyes in aqueous solution. In a typical experiment, 3 mL of 20 mM of either Bourdeaux Red (Aldrich, dye content ~ 70%) or Methyl Orange (Fisher indicator) azo dye was combined with 20 µL of freshly prepared 5 mM NaBH4 and 50 µL of ~1 wt% aqueous solution of NP decorated PS spheres.(Gupta, Giordano, Gradzielski, & Mehta, 2013; Lang, Xing-Cai, & Jun-Jie, 2008) The catalytic degradation of the azo dye was monitored by UV-Vis spectroscopy with a Varian Cary Win 300 Bio UV-Vis spectrophotometer as a decrease in absorption with time. Reaction rates have not been reported since the time required for degradation depended greatly on how well the NP decorated PS spheres dispersed into the solutions of dye molecules (e.g., agitation of the sample) and the time passed since preparation of the $NaBH_4$ solution.

3.5. Results and Discussion

Nanoparticle decorated PS spheres were prepared by a two-step method. Nanoparticles and PS spheres were individually prepared before assembly into PS@NPs. This two-step process enables control over the properties of both the NPs and PS spheres; in contrast to a one-pot method, a two-step process is optimal for tuning the properties of the final PS@NPs. In our method, PVP stabilized NPs were first synthesized using literature methods as described above, via routes that could be extended to the preparation of a variety of other metal and metal alloy NPs,(Ung et al., 2009) metal oxide NPs,(S. Sun et al., 2003; S. Yang & Gao, 2006) and semiconducting NPs.(Bae, Char, Hur, & Lee, 2008) These NPs were subsequently added to a suspension of amine functionalized PS spheres under acidic conditions (pH ~3) while stirring at 55°C for up to 3 h. These conditions produced uniform shells of evenly dispersed NPs self-assembled onto the surfaces of PS colloids. Previous work in our group has demonstrated the use of this method to prepare simple coatings of either gold nanorods/nanoparticles or lanthanide up-converting NPs on PS spheres (Fig. 3.2).(I. W.

Guo, Pekcevik, Wang, Pilapil, & Gates, 2014; Kinkead, Ali, Boyer, & Gates, 2013) The current study demonstrates that the general utility of this method by: i) creating PS@NPs from NPs prepared using a diverse range of synthetic routes; ii) preparing multi-component shells from the simultaneous self-assembly of NPs of different composition; and iii) controlling the ratio of dissimilar components, as well as the loading of NPs in these self-assembled shells.

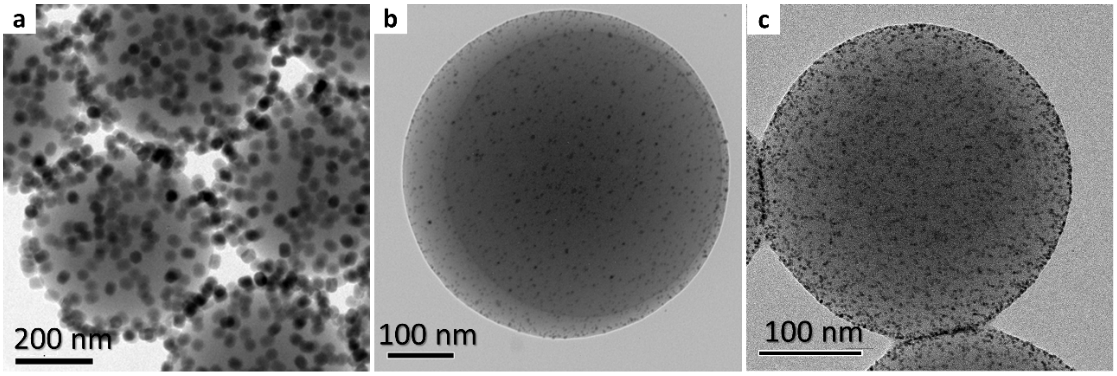

Figure 3.2 Transmission electron microscopy images of (a,b) amine-functionalized polystyrene spheres decorated with (a) lanthanide upconverting NPs or (b) Au NPs and (c) carboxylate functionalized polystyrene spheres decorated with Pt NPs.

The loading and distribution of NPs self-assembled onto a PS core has important implications for their utility, such as optimizing these materials for use in catalytic reactions or tuning their optical properties for use in biological imaging or sensing. The loading of NPs within the PS@NPs is controlled by tuning the relative concentrations of NPs and PS spheres during self-assembly. For example, the average number of NPs decorated onto 200 nm diameter PS spheres can be tuned by nearly one order of magnitude (Fig. 3.3). Average distance between the Pt NPs varied in proportion to their surface coverage. Nanoparticles were separated by 10.8 ± 4.3 nm, 9.3 ± 3.6 nm, and 6.2 ± 1.8 nm with corresponding parking areas (average surface area occupied by an individual NP on a PS sphere) of 92 nm^2 ± 16%, 68 nm^2 ± 15% and 30 nm^2 ± 9% per NP, for the samples with low, medium, and high Pt NP surface coverage, respectively. The NPs were uniformly distributed over the surfaces of the PS spheres as evaluated by TEM analysis (e.g., < 10% variation in NP-NP spacing for PS@Pt NP sample with high Pt loading) (Fig. 3.3). This uniformity is further supported by the relatively small (≤ 16%) and consistent variation in parking area measured for each surface coverage of NPs, while the average loading varied from ~100 to ~1000 NPs per sphere. It should also be noted that, in preparing multiple batches of the PS@NPs using the same method, that reproducibility in the number of NPs per PS sphere was generally good (< 5 % variation between trials).

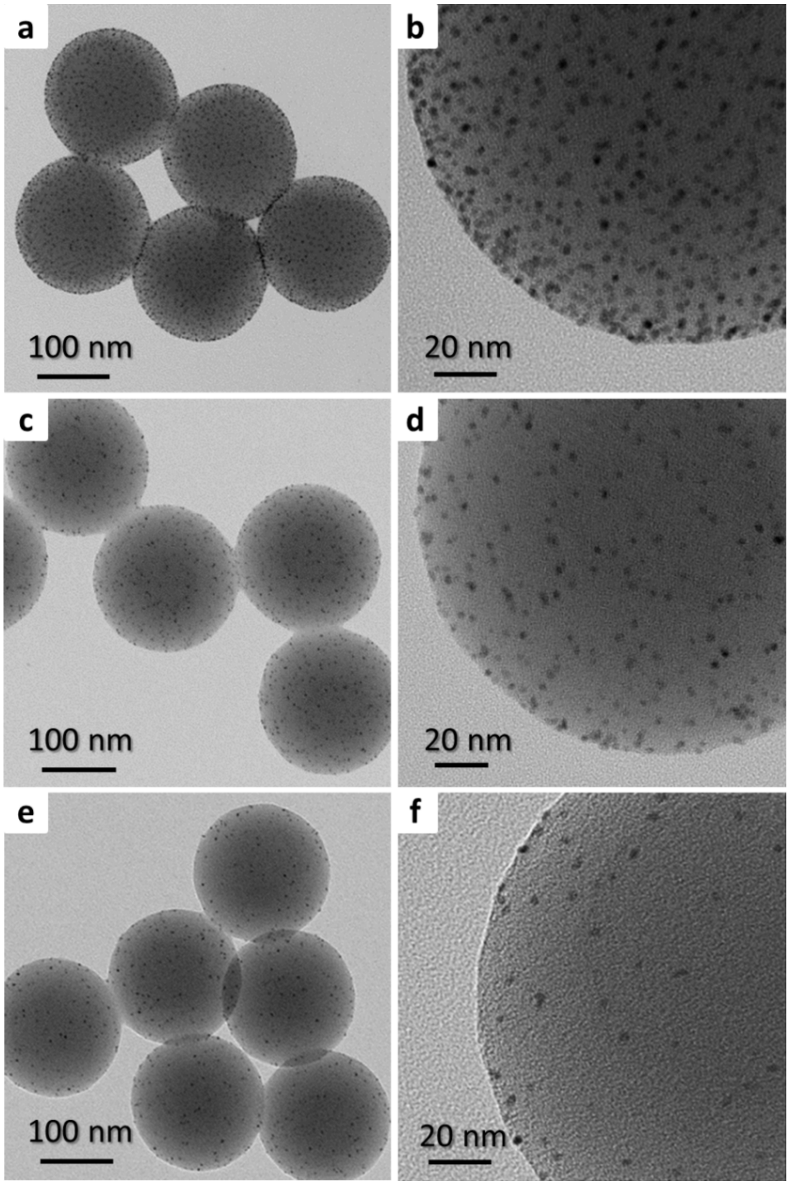

Figure 3.3 Low (left column) and high (right column) magnification transmission electron microscopy (TEM) images of Pt nanoparticle (NP) decorated 200 nm diameter polystyrene (PS) spheres with a high (a,b), medium (c,d) and low (e,f) NP surface coverage. The average number of NPs per PS spheres is 1026 ± 29 NPs for the sample with a high surface coverage, 362 ± 5 at a medium surface coverage and 116 ± 7 NPs for the sample with lowest surface coverage.

Complex multi-component nanoparticle systems have been pursued for a range of different applications, with each discrete type of nanoparticle lending unique properties to the final composite.(Mucic, Storhoff, Mirkin, & Letsinger, 1998; Shevchenko, Kortright, Talapin, Aloni, & Alivisatos, 2007) Multi-component PS@NPs were prepared through the assembly of a mixture of Pt and Pd NPs onto the surfaces of the PS spheres (Fig. 3.4). This is the first demonstration of a multi-component NP shell with fine control over the relative ratio of each component while also maintaining the original size and shape of each type of NP. Three different compositions of the Pt and Pd decorated PS@NPs (i.e., distinct ratios of Pt to Pd within the shell) were prepared by tuning the relative concentrations of each component during the self-assembly process. The relative ratio of Pt to Pd was assessed for each sample using XPS (Fig. 3.5). The uniformity of these samples, as measured by the distribution of individual NPs, was assessed by EDS elemental maps of the multi-component PS@NPs (Fig. 3.4). Each sample had a distinct composition and contained a uniform distribution of both Pt and Pd over the surfaces of the PS cores. These results are the first demonstration of a method to prepare uniform, multi-component PS@NPs with fine control over the concentration of distinct components. It also provides a unique ability to further optimize the properties of the assembled colloidal materials for specific applications.

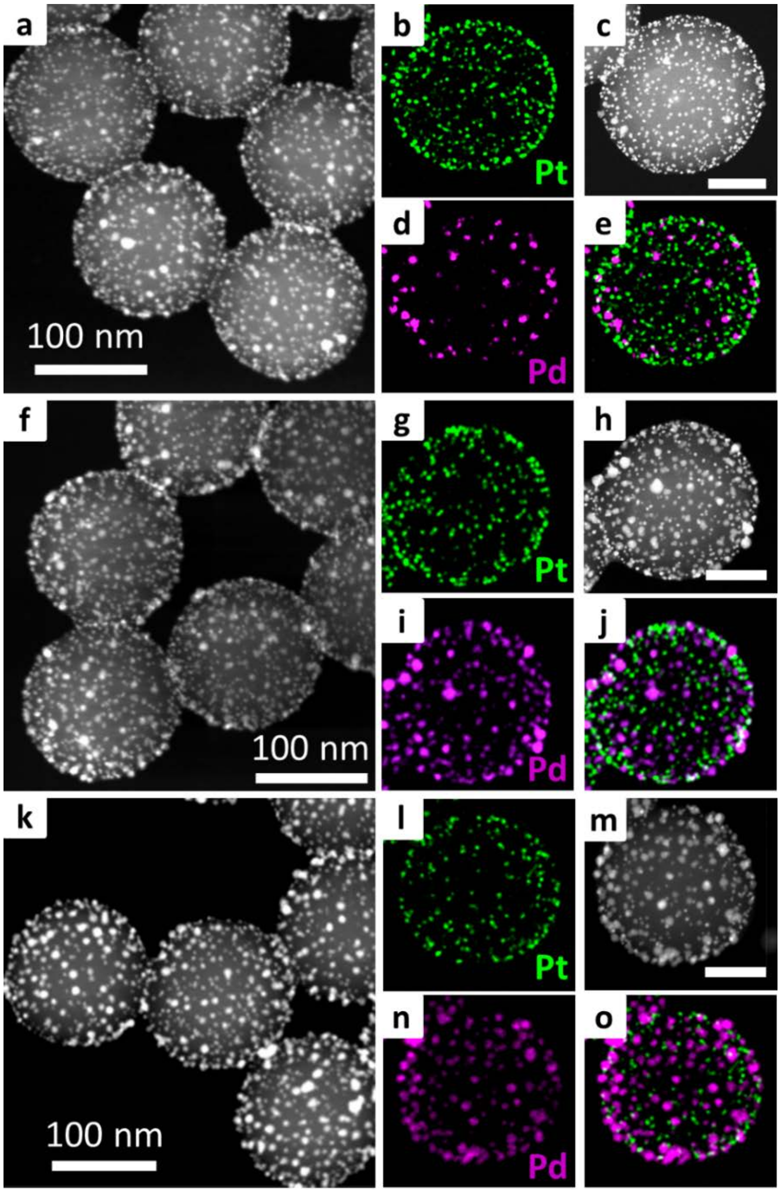

Figure 3.4 (a,f,k) Low and (c,h,m) high magnification (50 nm scale bars) STEM images and elemental mapping by EDS (b,d,e,g,i,j,l,n,o) of bimetallic NP coated 180-nm diameter PS spheres with a tuned ratio of Pt to Pd. Analysis by XPS determined the relative atomic concentrations for a ratio of Pt:Pd to be approximately 44:56, 22:78 and 12:88 for samples 1 (a-e), 2 (f-j) and 3 (k-o), respectively.

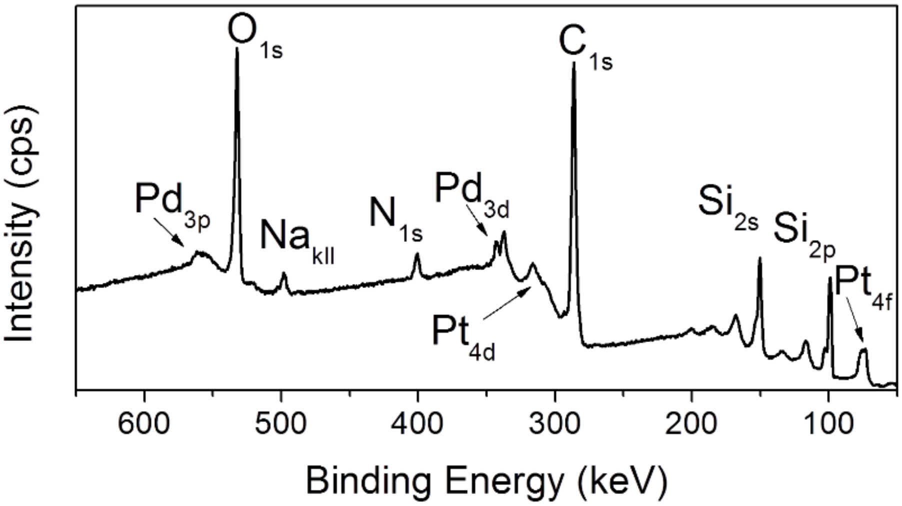

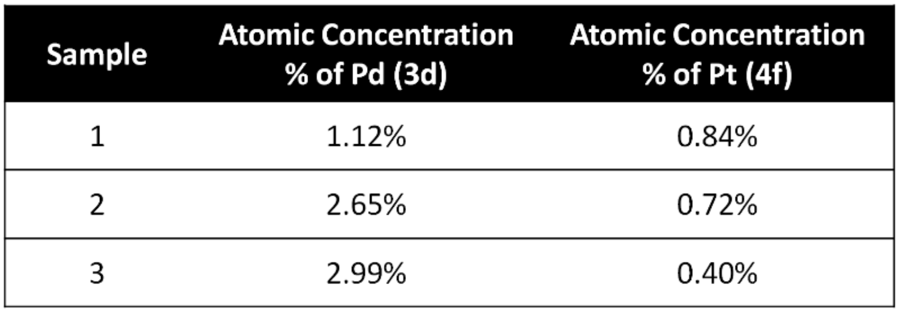

Sample	Atomic Concentration % of Pd (3d)	Atomic Concentration % of Pt (4f)
1	1.12%	0.84%
2	2.65%	0.72%
3	2.99%	0.40%

Figure 3.5 Representative XPS survey spectrum of PS spheres coated with both Pt and Pd NPs and table of percent atomic concentrations of Pd and Pt within samples 1, 2 and 3 of bimetallic NP decorated PS spheres. This sample was prepared for XPS analysis by drop casting a suspension of NP coated PS spheres onto a polished Si substrate. Concentrations were derived from analysis of the Pt 4f and Pd 3d XPS data and have an average percent standard deviation of 10% (e.g., 1.12 ± 0.11%).

In order to better understand how this method enables the formation of uniform coatings with control over composition and loading of NPs, we take a closer look at the components interacting during self-assembly. Many studies have explored the parameters that influence NP self-assembly, such as shape of the particles, surface chemistry, choice of solvent and its ionic strength.(A. Dong et al., 2011; Kalsin et al., 2006; Nie, Petukhova, & Kumacheva, 2010; Norris, Arlinghaus, Meng, Heiny, & Scriven, 2004; Sacanna, Pine, & Yi, 2013; Xia, et al., 2000) The processes taking place during the formation of these PS@NPs may be governed by a number of different mechanisms. It might appear that heterocoagulation plays a significant role in the self-assembly of

NPs onto the surfaces of PS spheres. The high ionic strength of our mixture though weakens the polar interactions of PVP with the PS spheres.(Smith, Meadows, & Williams, 1996) As well, the addition of increasing amounts of PVP while preparing the NP coatings either improves or has no effect on the self-assembly process,(I. W. Guo, et al., 2014; Kinkead, Ali, et al., 2013) which is counter to the effects seen by Li et al. when coating Au NPs onto PS spheres via heterocoagulation.(Yunxing Li, et al., 2012) The self-assembly observed in this study is attributed to the interactions of PVP stabilizing groups with the surfaces of the PS spheres. The dominant interactions are likely hydrogen bonding and electrostatic interactions. This conclusion is based in part on the reported conformation of PVP molecules in solution and the acidic conditions necessary for a successful assembly of the NP coating.(Borodko et al., 2006; Smith, et al., 1996) Additional observations that support this conclusion include: i) unsuccessful attempts to prepare high-quality NP coatings by the same conditions using different surface chemistries on the NPs (e.g., trisodium citrate) ii) the ability to prepare NP coatings with PS spheres with other functionalities that enable H-bonding (e.g., carboxyl functionalized PS at pH 3, Fig. 3.2); iii) uniformity of NP coatings regardless of the type of NP; and iv) homogeneity of the composition over the surfaces of the PS spheres for a multi-component coating. Small amounts of PVP appear to remain associated with the NP decorated PS after purification (Fig. 3.6), suggesting that PVP interacts strongly with the PS spheres (enduring the purification process) and may stabilize the NP coatings on the surfaces of the PS spheres. The even distribution of NPs over the surfaces of the PS spheres is most likely due to coulombic repulsion between neighbouring NPs.(Xia, et al., 2000) Altogether, these observations suggest that PVP plays a key role in the self-assembly process, through simultaneous interactions with the surfaces of both the NPs and PS spheres to create stable, tunable and uniform PS@NPs.

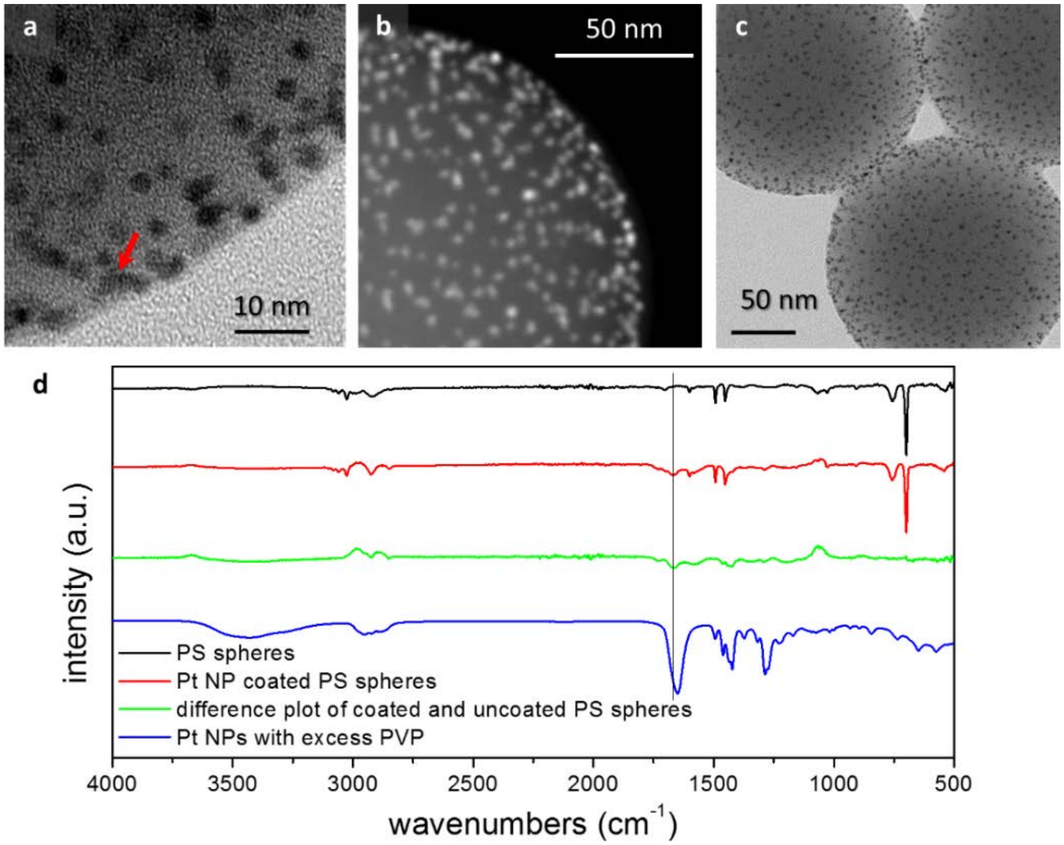

Figure 3.6 (a) High-resolution TEM image, (b) high magnification STEM image, and (c) low magnification TEM image of Pt nanoparticle (NP) coated PS spheres. The red arrow indicates a region where lattice fringes of the Pt NPs can be seen. (d) FTIR spectra acquired by ATR spectroscopy for the uncoated PS spheres (black trace), the Pt NP coated PS spheres (red trace) and the as-synthesized polyvinylpyrrolidone (PVP) stabilized Pt NPs (blue trace). The green trace is the difference between the ATR-FTIR spectra for the bare and Pt NP coated PS spheres. The black line indicates the region of the carbonyl stretch for PVP. This stretch is visible in the difference plot, suggesting the presence of PVP on the PS@NPs, even after several washings.

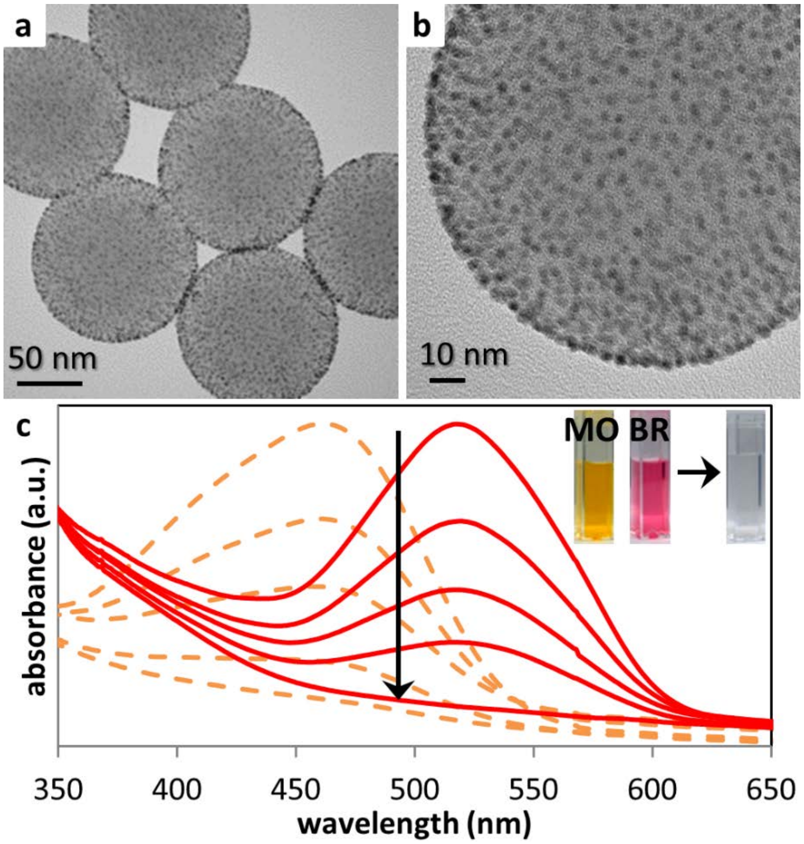

Figure 3.7 (a) Low and (b) high magnification TEM images of FePt NP coated PS spheres. (c) UV-Vis absorbance spectrum of methyl orange (MO, orange dashed traces) and Bourdeaux red (BR, solid red traces) dyes recorded during a catalytic degradation facilitated by FePt NP coated PS spheres. The first spectrum was recorded shortly after addition of the PS@NPs to each solution of dye. The remaining spectra were obtained at approximately equal intervals of time between the first and last spectra (approximately 10 min overall). Inset optical images show solutions of MO and BR dyes before (left) and after (right) catalytic degradation.

Coating NPs onto the surfaces of PS spheres prior to use in a catalytic reaction imparts several advantages. These advantages include, but are not limited to, stabilization of the NPs during the catalytic reaction and simplification of the process required to isolate these particles from solution following the reaction. For example, the PVP stabilized Pt NPs could not be readily isolated from the solution by centrifugation (at force < 3000xg) or filtration following their initial synthesis. Upon coating onto the PS spheres, these NPs were quickly separated from solution via centrifugation at a relatively low force (e.g., 3 min at 1000xg for Pt NP decorated 200-nm diameter PS spheres) or filtration. The catalytic degradation of azo dyes, a potentially harmful environmental contaminant, using FePt NP decorated PS spheres demonstrates the utility of these materials in catalytic reactions. These studies also provided further insight into the colloidal stability of the decorated PS spheres. The FePt NPs were chosen for this study due to their monodisperse size and shape, which was necessary in order to appropriately assess changes in the loading and distribution of NPs within the coatings. In contrast to our demonstration of Pt/Pd NP coated PS spheres (Fig. 3.4), this demonstration of multimetallic FePt coated PS spheres contain NPs composed of an alloy of Fe and Pt (see Appendix C for details). Suspensions of FePt alloy NP decorated PS spheres (Fig. 3.7) were combined with either methyl orange (MO) or Bordeaux red (BR) azo dyes along with a dilute solution of $NaBH_4$ (as a co-catalyst).(Gupta, et al., 2013; Lang, et al., 2008) Degradation of the dyes was monitored by UV-Vis spectroscopy through a decrease in absorption by the dyes (Fig. 3.7). A complete loss of the dye's absorption peak was typically observed after about 10 min. The addition of only the NP coated spheres or only a dilute $NaBH_4$ solution had no measurable impact on the absorption of the dye in solution. These results indicate that the assembled coatings of NPs were catalytically active; the observed decrease in UV-Vis absorption did not result from a reaction with $NaBH_4$ alone or from adsorption of dye molecules onto to the NP coated PS spheres. The FePt NPs remained adhered to the surfaces of the PS spheres after the five catalytic cycles (Fig. 3.8). Approximately one third of the NPs appear to be lost from the coatings by the end of the fifth catalytic reaction (without accounting for aggregation or agglomeration of the FePt NPs remaining adhered to the surfaces of the PS spheres). Further analysis of the TEM images suggests that agglomeration of NPs on the surfaces of the PS spheres could be a predominant route for the observed NP "loss". This observation indicates that the PVP continues to interact with the surfaces of the PS spheres (and adhere the NPs to those surfaces), but a disruption of the coulombic repulsion between the NPs results in a change in NP distribution. Overall, the PS@NPs exhibit desirable properties for potential use in aqueous and alcohol based catalytic reactions, such as tunability of the NP coatings, ease in separating the PS@NPs from reactant solution and their stability over multiple catalytic cycles in the degradation of azo dyes.

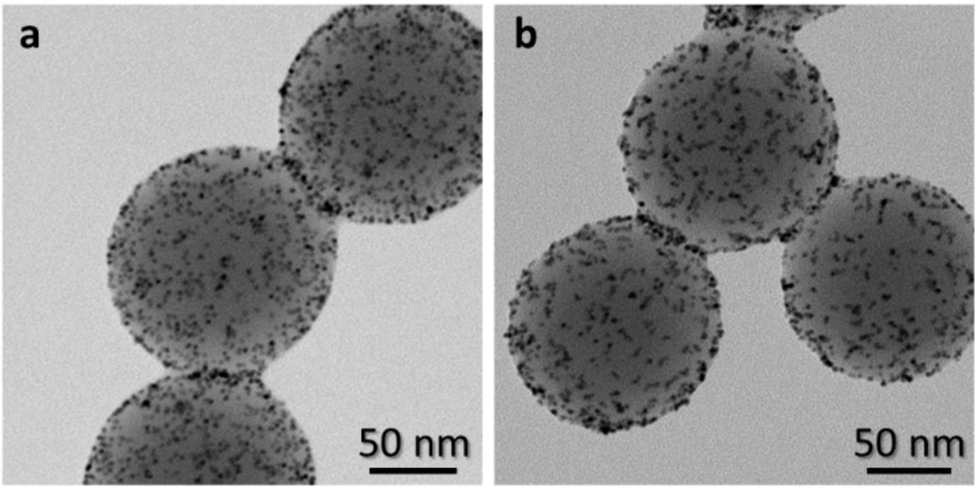

Figure 3.8 **Images obtained by TEM analysis of FePt NP decorated PS spheres (A) before and (B) after five separate uses of these decorated PS spheres to catalytically degrade azo-dyes. The number of the FePt NPs that were visible by TEM analysis per PS sphere decreased by about ⅓ from (A) 365 ± 13 NPs per sphere to (B) 236 ± 5 NPs per sphere. This analysis does not account for aggregation or agglomeration of the FePt NPs while still adhered to the PS spheres, although this redistribution appears to be the primary change in the FePt NP coatings.**

3.6. Conclusions

A tunable method has been demonstrated for the preparation of uniform NP decorated PS spheres by self-assembly of NPs onto the surfaces of PS spheres. Uniformity of these coatings, regardless of the composition of the NP, is attributed to interactions between the PVP stabilizing groups on the NPs and the functionalized surfaces of the PS spheres, as well as from coloumbic repulsion between the NPs. The NP surface coverage was tuned from 1.1×10^4 to 3.3×10^4 Pt NPs per um^2 of PS surface area, providing the ability to optimize NP density as necessary for future applications. Multi-component coatings of NPs were prepared by the co-assembly of Pt and Pd NPs. The relative ratio of each component could be readily tuned during the self-assembly process. The distribution of NPs over the surfaces of the PS spheres appeared uniform by electron microscopy analysis and elemental mapping based on energy dispersive X-ray spectroscopy (in the case of multi-component NP coatings). This uniformity was statistically confirmed for Pt NP decorated PS spheres of varying NP loading by analysis of the average particle spacing. Polystyrene spheres decorated with FePt NPs were also prepared and shown to be active in the catalytic degradation of azo dyes, a toxic environmental contaminant. This activity indicates that the NPs are available to interact with other molecules in solution (e.g., not shielded by PVP or PS). This observation suggests that the NP coatings can be effectively transferred to a secondary support. The NP coatings were also found to be stable following several subsequent catalytic reactions. A change in NP distribution was observed (e.g., aggregation of the NPs on the surfaces of the PS spheres), but the NPs appeared to remain adhered to the PS spheres surfaces as a result of persistent PVP interactions. This stability will be important in performing a quantitative transfer of the NP coatings to the secondary support, as the PS@NPs will be subject to varying conditions during the sacrificial template process (e.g., assembly into ordered arrays and electrodeposition solutions). The two-step method described here for creating NP decorated PS spheres has been demonstrated to be highly versatile for the preparation of PS@NPs that retain their colloidal stability, exhibit uniform composition over the PS sphere surfaces, and have a tunable loading of NPs. The adaptability of this method enables its use in preparing designer PS@NPs that exhibit properties suitable for a diverse range of potential applications. Moreover, the prepared PS@NPs can enable the preparation of OP electrodes with a diverse range of NP functionalities; including OP electrodes with variable NP loading and composition.

Chapter 4.

Platinum Nanoparticle Decorated Ordered Porous Gold Electrodes

4.1. Notice of Permissions

This chapter is based upon work recently submitted for publication: Brandy K. Pilapil, Julia van Drunen, Yoseif Makonnen, Diane Beauchemin, Gregory Jerkiewicz and Byron D. Gates, "Ordered Porous Electrodes by Design: Towards Highly Effective Platinum Utilization in Electrocatalysis". Permission to use the following material has been granted by all co-authors. Julia and Yoseif prepared Au@PtNP-OP samples for (e.g., dissolved Au and Pt) and performed analysis by inductively coupled mass spectrometry to determine Au and Pt masses in the Au@PtNP-OP samples. All other experiments, including preparation of the Au@PtNP-OP electrodes and their characterization by electrochemical and material science techniques, were performed by myself.

4.2. Introduction

The poor kinetics for ORR lead to a large overpotential of reaction and a correspondingly high mass of Pt is required in order to reach appreciable currents.(David, 2002; Mark K Debe, 2012) Ultrathin (< 1µm) CCL designs, such as that produced by 3M, can enhance Pt utilization in comparison to traditional C black supported Pt NP designs through improved mass transport properties and increased Pt stability, such that a greater portion of the mass incorporated into the CCL remains during fuel cell operation.(Mark K Debe, 2012; Mark K. Debe, 2012) Despite these improvements, the high cost of the CCL, along with continued performance issues (e.g., water management), continues to hinder the commercialization of low temperature FCs.(Mark K Debe, 2012; Rabis, et al., 2012) Direct methanol fuel cells (DMFCs) have additional constraints for the ORR catalysts relating to the use of methanol (MeOH) as a fuel, as opposed to H_2 gas.(Lamy, Coutanceau, & Alonso-Vante, 2009; Thomas, Ren, Gottesfeld, & Zelenay, 2002) From an infrastructure point of view, the use of MeOH is a more attractive fuel since it has a higher energy density than H_2 gas and requires less sub-system fuel delivery development than H_2 gas. Methanol crossover from the anode, among other issues, lowers the overall power density achieved in DMFCs and limits its commercial viability. Designing CCLs that are MeOH tolerant could increase the power density achieved in DMFCs.(Lamy, et al., 2009; Thomas, et al., 2002)

Novel support@PtNP ordered porous electrocatalysts developed here aim to maximize the effective utilization of Pt for typical hydrogen-fueled PEM FCs and DMFCs. These Pt NP functionalized OP electrodes contain Pt NPs of uniform size well-dispersed over the inner porous network of an ordered porous support (support@PtNP-OP electrodes). The electrodes have been prepared through the use of a modular sacrificial template, as depicted in Fig. 4.1, providing control over catalyst layer thickness and porosity.(Kinkead, van Drunen, et al., 2013) The size and connectivity of the pores within the ordered porous electrode may also be tuned through the use of spherical templates of varying dimensions.(Lytle & Stein, 2010) To the best of our knowledge, this is the first demonstration of the use of NP coated spherical templates in the preparation of NP functionalized ordered porous materials (also known as inverse opals or 3DOM, 3D ordered macroporous, materials). This new route enables control over pore size and connectivity, Pt NP loading and NP-NP spacing through modification of the Pt NP coated sacrificial template.(Xia, et al., 2000) This ordered nature of the electrodes is different from other electrocatalyst designs that generally contain randomly distributed pores of widely varying size and a non-uniform distribution of Pt. The fine control over morphology of the Au@PtNP-OP electrodes could also enable them to be fine-tuned for further improved catalytic performance,(Nesselberger et al., 2013) though this is beyond the scope of the work presented in this chapter.

These electrodes are anticipated to have good mass transfer properties due to the open porous morphology, ultrathin design and uniform dispersion of Pt NPs throughout the catalyst layer.(Mark K Debe, 2012; Mark K. Debe, 2012; O.-H. Kim et al., 2013) A recent publication by Sung et al. found that a similar architecture (a pure-Pt OP catalyst layer) out-performed conventional ink-based catalyst layer architectures due to morphological advantages.(O.-H. Kim, et al., 2013) The use of Pt NPs, instead of a pure Pt design, should improve Pt utilization in this ultrathin design due to the much greater proportion of Pt atoms exposed to the outer surfaces of the electrode. The aggregation, agglomeration, dissolution and overall loss of Pt NPs is anticipated to be minimized through the use of a Au support.(Awad, El-Deab, & Ohsaka, 2007; S. Guo, Fang, Dong, & Wang, 2007; Senthil Kumar & Phani, 2009; Y. Shao, et al., 2007; Topalov, et al., 2012; C. Xu, Wang, Chen, Zhang, & Ding, 2010; J. Zhang, et al., 2007) Zhang et al. have reported that small Pt NPs can be stabilized through interaction with Au such that no Pt losses are observed during an accelerated durability test, in comparison to an almost 45% loss of Pt surface area for comparable catalyst layers without Au.(J. Zhang, et al., 2007) Interactions with a Au support have also been shown to improve MeOH-tolerance of Pt NP catalysts, such that ORR activity of the Pt is less sensitive to MeOH crossover in DMFCs.(Hernández-Fernández et al., 2008; Senthil Kumar & Phani, 2009; J. Wang, Yin, Wang, Wang, & Gao, 2008)

The work reported in this chapter aims to develop a new Pt NP decorated OP electrocatalyst for potential use in low temperature fuel cells. The Au@PtNP-OP electrodes are expected to exhibit an improved stability of Pt NPs, in comparison to traditional C black/ionomer supported Pt NP designs through support interactions with Au and increased Pt SSA over other ultrathin CCL designs through the use of Pt NPs rather than a porous Pt or Pt thin film designs).(Mark K Debe, 2012; Mark K. Debe, 2012; O.-H. Kim, et al., 2013; Kinkead, van Drunen, et al., 2013) These electrodes were extensively characterized using a variety of material science techniques to evaluate material properties such as Pt NP transfer from the sacrificial template and alloying of Pt with the Au support. Electrochemical properties of the Au@PtNP-OP electrodes have also been assessed, including stability of the electrodes during electrochemical cycling, and activity of the electrodes towards ORR and MOR electrocatalysis.

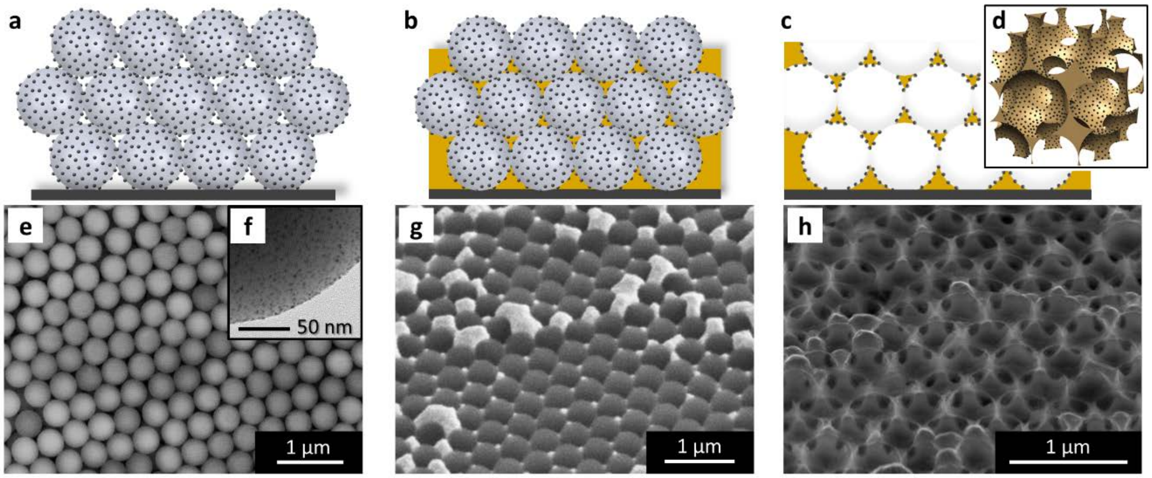

Figure 4.1 **Platinum nanoparticle functionalized ordered porous gold (Au@PtNP-OP) electrodes have been prepared through a modular sacrificial template method. (a) Polystyrene (PS) spheres coated with Pt NPs were assembled into an ordered array. (b) Gold was electrodeposited through the PS sphere assembly, filling the voids between adjacent PS spheres. (c) Polystyrene spheres were dissolved in solution of toluene and hexanes to reveal the ordered porous structure coated with Pt NPs. (d) A 3D schematic of a small section of the prepared Au@PtNP-OP electrodes depicts the porous scaffold of Au coated with Pt NPs. Electron microscopy images were obtained during the preparation of Au@PtNP-OP electrodes. (e) Top view scanning electron microscopy (SEM) image of a PS sphere assembly. (f) Transmission electron microscopy (TEM) images of a section of a Pt NP coated PS sphere (dark spots on the grey hemispherical region are Pt NPs). (g) SEM image of gold filled PS sphere assembly at 45° tilt to normal. (h) SEM image of a Au@PtNP-OP electrode at 60° tilt to normal (dark regions are connections between the spherical pores).**

4.3. Experimental

Platinum NP coated Au OP electrodes were prepared using a sacrificial polystyrene (PS) template. All solvents and chemicals were purchased from either Alfa Aesar, Fisher Scientific, or Sigma-Aldrich and used as received. Polyvinylpyrrolidone (PVP, 55k MW, Sigma-Aldrich Co.) stabilized Pt NPs were first synthesized by literature methods with some optimizations for our research, as reported in the previous chapter. The prepared Pt NPs were subsequently coated onto the surfaces of PS spheres (Polysciences Inc., 0.5 µm nominal diameter, amine functionalized), also reported in the previous chapter. The Pt NP coated PS spheres were then washed 3 times through sequential centrifugations and dispersions, first in water, followed by two cycles in ethanol. The spheres were then dried before dispersion in 1-BuOH (Alfa Aesar, ACS Grade) at ~ 1 wt % dilution. The Pt NP coated PS spheres were then assembled at an air-water interface, as per our previous work.(Kinkead, van Drunen, et al., 2013) Three layers of the resulting close-packed assembly of Pt NP coated PS spheres were sequentially transferred to a polished glassy carbon disk (Pine Instrument Company, glassy carbon ChangeDisk rotating disk electrode (RDE) tip). The use of a glassy carbon disk support allowed for control over the geometric area of the Au@PtNP-OP electrodes and enabled the use of RDE measurements. These assembled templates were dried in a vacuum desiccator overnight, rinsed with ethanol and then dried in an oven at 70°C for 1 hour prior to use as a sacrificial template. Gold electrodeposition was performed with TECHNI-GOLD 25 ES solution, prepared as per manufacturer directions. Gold was deposited through the sacrificial template by pulsed electrodeposition at 38ºC (50 pulses, 5 min at 9 µA followed by 10 s at open circuit potential), at which point the gold deposit covered 2.5 layers of the 3 layer PS sphere assembly. The PS spheres were removed by dissolution in refluxing solvent (1:1, v/v toluene to hexanes, Sigma Aldrich, ACS Grade). Gold ordered porous electrodes were similarly prepared without the additional step of coating the PS spheres with Pt NPs prior to assembly and infiltration.

For comparison to the Au@PtNP-OP electrodes, commercial C black/ionomer supported Pt NP catalyst ink electrodes were also prepared. TEC10E50E (Tanaka Kikinzoku Kyogya co. ltd.) commercial catalyst ink solution containing 50 wt% Pt and 50 wt % C black was combined with Nafion D520 (DuPont) to create a dispersion with 70 wt% Pt/C black and 30 wt% Nafion ionomer. This solution was then ultrasonicated for ~1 hour (Branson Sonic Dismembrator) to ensure complete mixing of the components. This catalyst ink solution was drop cast onto the surface of a polished glassy carbon disk electrode (3 µL volume) and dried overnight in a vacuum desiccator to evaporate all solvent. The disk and associated catalyst electrode were held at 70°C for 1 hour prior to use in electrocatalytic experiments to ensure that no solvent contaminants were present upon introduction to the electrochemical setup. The SSA of Pt for the catalyst ink electrode is 28 ± 3 m^2 per g ($\boldsymbol{A}_{ecsa,Pt}$) with a Pt mass of 3.9 ± 0.5 mg per cm^2 (geometrical electrode area). ThePt NP diameter is in the range of 2 to 3 nm.

Transmission electron microscopy (TEM) and scanning TEM (STEM) images of the template spheres and Au@PtNP-OP electrodes were obtained using a FEI Osirus X-FEG S/TEM operating at 200 kV. The Pt NP coated PS sphere TEM samples were prepared by drop casting ethanol solutions of the particles onto C/Formvar 300 mesh TEM grids (Ted Pella Inc.). ImageJ software was used to analyze the percent surface area of the PS spheres covered by the Pt NPs on the prepared templates. This analysis was performed by selecting an area in which only the top surface Pt NPs were clearly visible (the thickest region with respect to the electron beam). To prepare the 0.5 pore layer Au@PtNP-OP electrode for TEM imaging, the electrode was fabricated onto the glassy carbon disk inserts and subsequently scraped from the surface with a scalpel blade. The scalpel blade, with attached Au@PtNP-OP electrode scraping, was then dipped into a vial of water, transferring the electrode from the scalpel to the high-surface tension water surface. The electrode was then floated onto a 300 mesh Ni grid (Electron Microscopy Sciences). Scanning electron microscope images were acquired with a FEI Strata 235 DualBeam scanning electron microscope (SEM) operating at 10 or 15 kV before and after stability testing. Cross-section images were obtained by cutting through the Au@PtNP-OP electrodes with a scalpel blade and imaging at a 45° to 60° tilt to normal.

X-ray photoelectron spectroscopy (XPS) was performed with a Kratos Analytical Axis Ultra DLD spectrometer using a monochromatic aluminum source (Al Kα, 1486.6 eV) operating at 150 W (10 mA emission current and 15 kV HT). This analysis provides information on the relative quantity and chemical environment of Pt and Au on the surfaces of the Au@PtNP-OP electrodes. A Tougaard baseline was used for fitting analysis of Pt 4f peaks, rather than the standard Shirley baseline, due to the overlap with the large neighbouring Au 4f peak. Fitting analysis of the Pt and Au 4f peaks was performed according to previous studies.(Hammond & Winograd, 1977; Jackson et al., 1993; Juodkazis, Juodkazyt, Jasulaitien, Lukinskas, & Šebeka, 2000; Lim, Lopez-Salido, Dietsche, Bubek, & Kim, 2006)

Electrochemical experiments were carried out using a Princeton Applied Research model 263A potentiostat in glassware freshly cleaned by established methods.(Angerstein-Kozlowska, 1984) A standard three electrode setup was used, with a Pt reversible hydrogen reference electrode (RHE), Pt gauze counter electrode and 0.5 M H_2SO_4 electrolyte (Fisher Scientific, ACS Reagant Grade, diluted with deionized water). The working electrodes consisted of Au@PtNP-OP electrodes, prepared on glassy carbon ChangeDisk RDE tips, in the Teflon shroud design prepared by Pine Instruments for the use of disk inserts with their modulated speed rotator setup. Prior to study, the electrode and Teflon shroud were subject to Soxhlet extraction in acetone for at least 3 h. Platinum electrode materials were supplied by Alfa Aesar (Pt≥99.9%). The RHE electrodes and cell used in evaluating methanol oxidation activity were prepared by Verrerie de Precision Enr. Cyclic voltammetry (CV), oxygen reduction, and carbon monoxide oxidation tests were performed using Pine Instrument's modulated speed rotator setup with associated 4-neck flask.

Contaminants were initially removed from the electrode surface by cycling between 0.05 to 1.8 V (vs. RHE) at a v of 50 mVs^{-1} for ~ 20 cycles, as per previous literature on the analysis of Au electrodes.(El- Deab & Ohsaka, 2002) Extensive cycling between this range resulted in dissolution of Au and subsequent loss of Pt NPs, and so cycling between this range was limited to cleaning and evaluating electrochemical surface area (A_{ecsa}).(Cherevko, Topalov, Zeradjanin, Katsounaros, & Mayrhofer, 2013) A_{ecsa} of Au and Pt were determined from CV analysis, as per literature methods. (D. Chen, et al., 2011; Rand & Woods, 1972; Rouya, Cattarin, Reed, Kelly, & Zangari, 2012; Tremiliosi-Filho, Dall'Antonia, & Jerkiewicz, 2005) The Au oxide reduction and Pt H_{upd} adsorption/desorption peaks were integrated and divided by the scan rate to determine the charge passed during the respective processes at the electrode surfaces. These values were then divided by the characteristic charge passed per area during Au oxide reduction (q_{ox}, 750 ± 30 µC per cm^2) and Pt H_{upd} adsorption/desorption (q_H, 210 µC per cm^2 multiplied by a factor of 2 in order to account for both the adsorption and desorption peaks) to determine $A_{\text{ecsa,Au}}$ and $A_{\text{ecsa,Pt}}$, respectively. Note that ~ 2 monolayers of Au oxide is formed upon cycling to 1.8 V vs. RHE at 50 mVs^{-1} in 0.5 M H_2SO_4, as reflected in the q_{ox} value.(Rouya, et al., 2012; Tremiliosi-Filho, et al., 2005)

Carbon monoxide oxidative stripping analysis was performed before and after stability testing to evaluate changes in Pt surface structure.(Urchaga, Baranton, Coutanceau, & Jerkiewicz, 2011) Adsorption of CO onto the Pt surfaces was achieved by bubbling CO gas (5% CO, 95% N_2, 99.998% purity, Praxair) into the 0.5 M H_2SO_4 electrolyte while holding the electrode potential at 0.1 V (vs. RHE) for 15 min. Excess CO gas was then removed from the electrolyte by bubbling with N_2 gas (99.998% purity, Praxair) for 25 min. The potential was then scanned to 1.2 V (vs. RHE) at a rate of 20 mVs^{-1} to oxidize adsorbed CO from the Pt surfaces, followed by 2 CV scans from 1.2 V to 0.05 V (vs. RHE) at a rate of 20 mVs^{-1}.

Methanol oxidation experiments were performed in 0.5 M H_2SO_4 containing 1 M MeOH (Alfa Aesar, HPLC Grade) using cyclic voltammetry. Oxygen reduction experiments were carried out in O_2 saturated (1 atm) 0.5 M H_2SO_4 electrolyte. The use of H_2SO_4 electrolytes while evaluating Pt electrocatalytic activity is not ideal due to interactions between Pt and sulfur containing species, leading to changes in Pt activity. However, it was not possible to use the preferred perchloric acid in these studies due to safety concerns (e.g., explosive hazard). Electrolytes were saturated with O_2 by bubbling O_2 gas (99.98 %, Praxair) into the electrolyte for 20 min prior to experimentation and then purging the air above the electrolyte with O_2 gas during experimentation to maintain saturation. Oxygen reduction activity was evaluated before and after stability testing by RDE method and cyclic voltammetry. The RDE experiments were conducted at 400, 900, 1200, 2000 and 2500 rpm, starting from 1.2 V (vs. RHE) and scanning to 0.2 V (vs. RHE) at a rate of 10 mVs^{-1}. Before each linear scan experiment, the electrode was cycled once between 0.05 and 1.8 V to remove any surface contaminants.

Mass analysis was conducted on a Varian 820MS (Mulgrave, Victoria, Australia) quadrupole-based ICP-MS instrument featuring the Turner interlaced load coil configuration, which minimizes secondary discharge, allowing representative spatial profiling of the plasma. Sample introduction consisted of a MicroMist concentric nebulizer (Glass Expansion, Pocasset, USA) fitted into a Scott double-pass spray chamber and maintained at 0°C via a computer controlled Peltier cooling system. The optimal plasma operating conditions and measurement parameters are provided in

Appendix D. Standard solutions of Au and Pt in ultrapure 2% (v/v) aqua regia (J.T. Baker, Phillipsburg, USA) were prepared from a stock 500 µg/L multi-elemental standard solution, which was made from commercially available 1000 mg/L single element standard solutions (SCP Science, Quebec, Canada) and demineralized water (Arium Pro UV/DI System, Sartorius Stedim Biotech, Goettingen, Germany). A blank and five external calibration standards over the 0.1 to 500 µg/L range were prepared in 2% v/v aqua regia. The Pt and Au from solid samples of Au@PtNP-OP electrodes after material and electrochemical analysis were dissolved in 1 mL of aqua region for 30 minutes, heated to 30°C. Nine mL of demineralized water was then added to obtain a 10 mL volume of sample for analysis by ICP-MS. The results were then correlated back to the original masses of Au and Pt in the Au@PtNP-OP solid samples.

4.4. Results and Discussion

Platinum nanoparticle functionalized ordered porous gold electrodes were prepared through the use of a modular sacrificial template (Fig. 4.1). Platinum NPs with a diameter of 2.6 ± 0.4 nm were uniformly assembled onto the surfaces of ~420-nm diameter amine-functionalized polystyrene (PS) spheres. The NP decorated PS spheres had a NP loading of 1 NP per 59 ± 4 nm^2 on the PS sphere surfaces and a NP-NP spacing of 9 ± 2 nm between adjacent NPs (Fig. 4.2). The NP decorated PS spheres were assembled into an ordered array at an air-water interface and transferred to the glassy carbon (GC) disk electrode.(Kinkead, van Drunen, et al., 2013; Moon, et al., 2011) This assembly route was chosen over other routes since it allows for simple control the thickness of the sacrificial template.(Kinkead, van Drunen, et al., 2013; Moon, et al., 2011; Xia, et al., 2000) Gold was electrodeposited by a galvanostatic method through the ordered template of the Pt NP coated PS spheres. The PS sphere template was then removed to reveal the ordered porous network (Fig. 4.3). Previous reports have demonstrated the preparation of NP functionalized OP materials, generally through reduction of a metal salt (to form NPs) onto a pre-formed OP framework.(J. I. L. Chen, Loso, Ebrahim, & Ozin, 2008; Guan et al., 2007; Justin & Andreas, 2006; Jun Zhang et al., 2009) The method demonstrated here, whereby NPs are transferred from the PS template provides much greater control over NP properties (e.g., size, shape and loading) than these previously reported methods. This study focuses on the analysis of Au@PtNP-OP electrodes that are ~2.5 pore layers thick. The sacrificial template assembly consisted of three close-packed layers of PS spheres and Au was electrodeposited to a thickness equivalent to ~2.5 PS sphere layers (or ~1 μm). The top of the electrode consists of half-pores, such that the outermost surface of the electrode consists of Pt NPs decorating a regular array of bowl shaped porous Au structures. This design was sought as to enable the study of Pt NPs by surface sensitive techniques such as X-ray photoelectron spectroscopy. The open 3D network of these electrodes enables electrolyte to access the entire porous network and is anticipated to have good mass transfer properties.(O.-H. Kim, et al., 2013; Kinkead, van Drunen, et al., 2013)

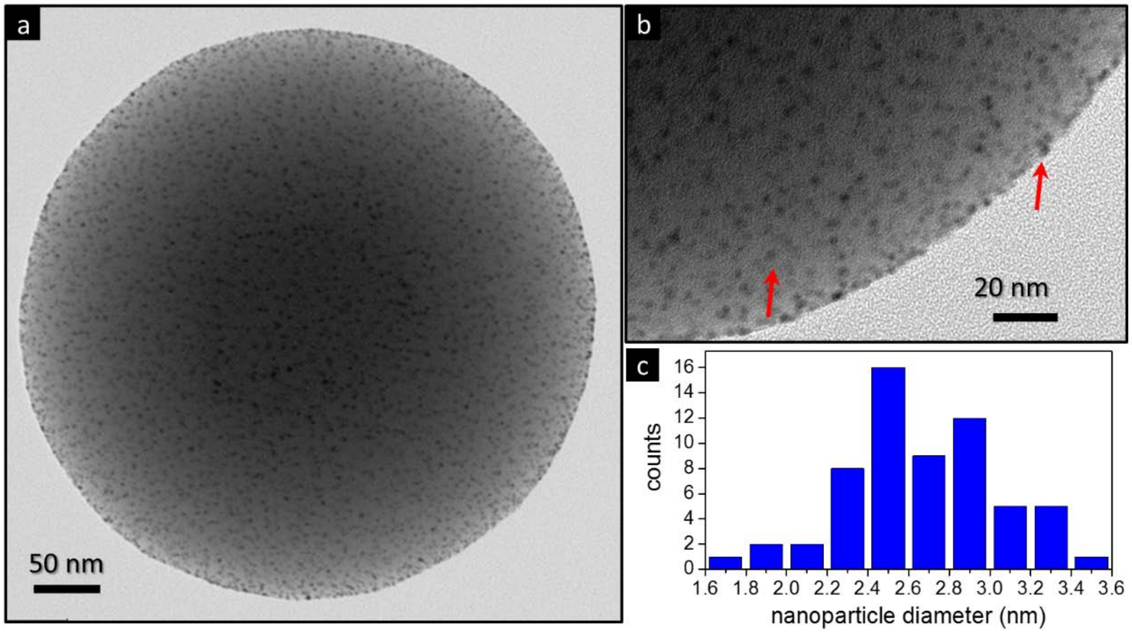

Figure 4.2 **Transmission electron microscopy images of a Pt nanoparticle (NP) coated 500 nm diameter polystyrene (PS) sphere at (a) low and (b) high magnification. Red arrows point to Pt NPs on the PS sphere surface. (c) Histogram of Pt NP size distribution.**

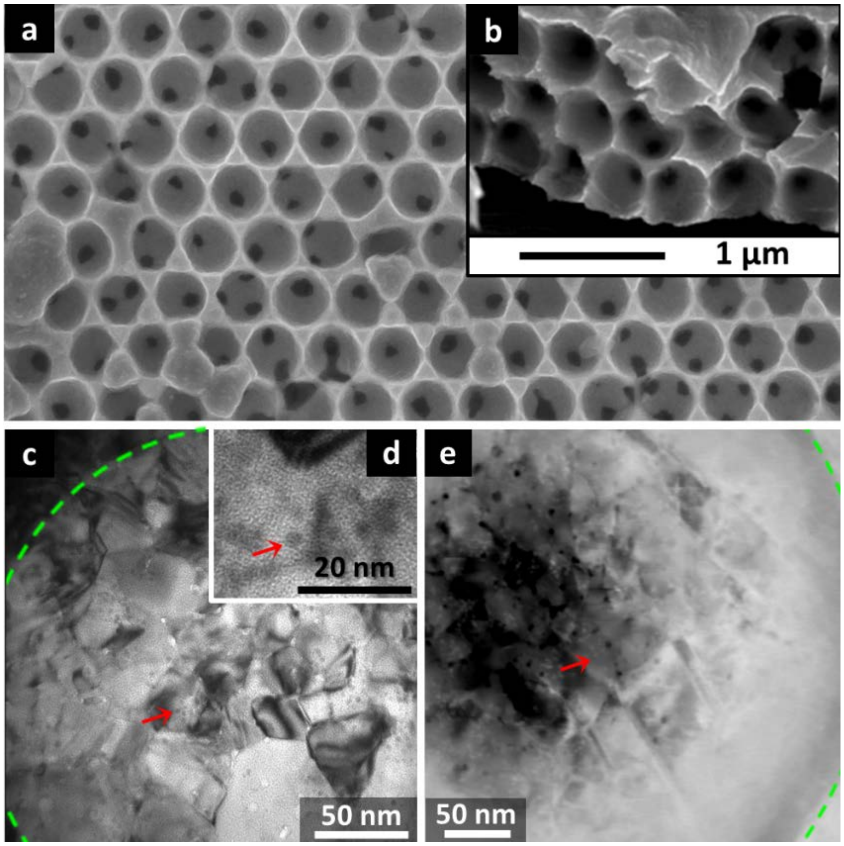

Figure 4.3 **Electron microscopy images of Au@PtNP-OP electrodes. Representative SEM images of Au@PtNP-OP electrodes; (a) top view, and (b) cross-sectional slice at a 60° tilt to normal (1 µm scale bar applies to both SEM images). Transmission electron microscope images obtained at (c) medium and (d) high magnification, and (e) scanning TEM image of the bottom of a single pore within a Au@PtNP-OP electrode. Green dashed line indicates the edge of the Au@PtNP pore and red arrows indicate individual Pt NPs imaged on the surfaces of the Au-OP electrode.**

Analysis of the Au@PtNP-OP electrodes by electron microscopy was performed to confirm the formation of a 3D ordered porous Au framework and the transfer of Pt NPs from the PS sphere templates to this framework. Scanning electron microscopy (SEM) analysis of the Au@PtNP-OP electrodes confirmed the formation of a 3D ordered porous Au network, with uniform pore sizes and a high-level of interconnectivity. Analysis by transmission electron microscopy (TEM) of a fragment of the Au@PtNP-OP electrodes was necessary to image the Pt NPs on the Au surfaces (due to the limiting spatial resolution of the SEM imaging tool used). The TEM images of this Au@PtNP-OP electrode indicate the presence of large Au grains with small, dark spots visible in regions near to the center of the Au macropore, where the Au is thinnest. Similarly, scanning TEM (STEM) images of this Au@PtNP-OP electrode contain small, brighter spots near the same thin region at the center of the macropore. These particles are most likely the Pt NPs transferred from the surfaces of the spherical PS templates. The size of the spots correspond to the original dimensions of the Pt NPs (~2.5 nm in diameter, Fig. 4.4) and the z-contrast (atomic number contrast) observed for the spots under TEM and STEM analysis corresponds to that expected for Pt NPs (higher atomic number/electron density) on a Au support. Mass analysis by ICP-MS was pursued to confirm further the transfer of Pt NPs to the Au framework and to establish the mass ratio of Pt to Au. These results indicated that each Au@PtNP-OP electrode (of ~2.5 pore layer thickness) contained a Pt mass of 2.5 ± 0.5 µg cm^{-2} geometrical area of the electrode ($\boldsymbol{A}_{geom}$) and a Au mass of 760 ± 40 µg cm^{-2} ($\boldsymbol{A}_{geom}$). The Pt NPs account for 0.4 ± 0.1 % of the total electrode mass. This analysis further confirmed that Pt NPs transferred to the porous Au scaffold.

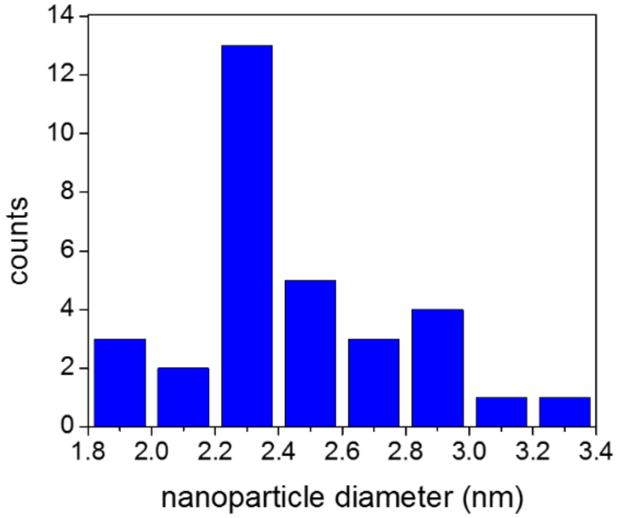

Figure 4.4 Histogram of Pt NP size distribution as measured on a fragment of a Au@PtNP-OP electrode.

Further verification of a successful and quantitative transfer of Pt NPs from the PS sphere templates to the Au porous support was sought via further TEM analysis of the sacrificial templates and comparison to X-ray photoelectron spectroscopy (XPS) and cyclic voltammetry (CV) analyses. A detailed analysis of TEM images of the Pt NP coated PS sphere templates (e.g., Fig. 4.2) reveals that that Pt NPs cover 18 ± 4 % of the surfaces on the PS spheres. X-ray photoelectron spectroscopy survey scans of the Au@PtNP-OP electrodes reveal that Pt covers 15 ± 2 % of the surface of the Au-OP electrode (Fig. 4.6). Note that the errors for the XPS and CV analyses reported here were estimated based on one standard deviation from the mean from the analysis of three independently prepared Au@PtNP-OP samples. The XPS value may be less accurate, due to the non-flat morphology of the electrode surface. Cyclic voltammetry traces of the Au@PtNP-OP electrodes (Fig. 4.5) were used to determine electrochemical surface area ($\boldsymbol{A}_{\text{ecsa}}$). The $\boldsymbol{A}_{\text{ecsa}}$ of Au ($\boldsymbol{A}_{\text{ecsa,Au}}$) and Pt ($\boldsymbol{A}_{\text{ecsa,Pt}}$) were determined to be 1.2 ± 0.3 cm^2 and 0.21 ± 0.03 cm^2, respectively. These $\boldsymbol{A}_{\text{ecsa}}$ values correspond to a Pt surface coverage of 18 ± 3 %. The overall agreement (within error) in the Pt surface coverage estimated from the XPS, CV and TEM analysis suggests that the Pt NPs were successfully and quantitatively transferred from the sacrificial spherical PS templates to the Au-OP support while preserving the properties of the Pt NPs (e.g., particle size, surface loading, and inter-particle spacing).

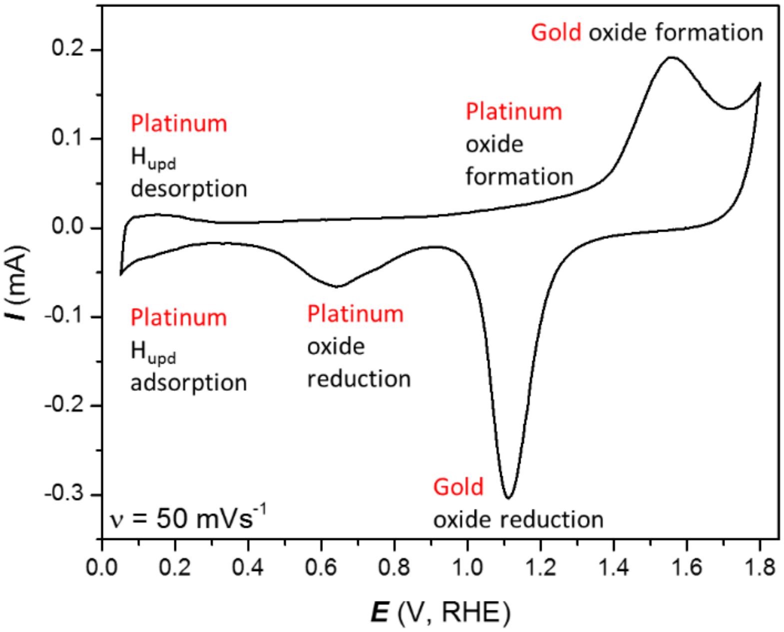

Figure 4.5 **Representative cyclic voltammetry (CV) trace of a Au@PtNP-OP electrode scanned between 0.05 and 1.8 V (vs. RHE). This CV trace displays peaks characteristic of both Pt and Au.**

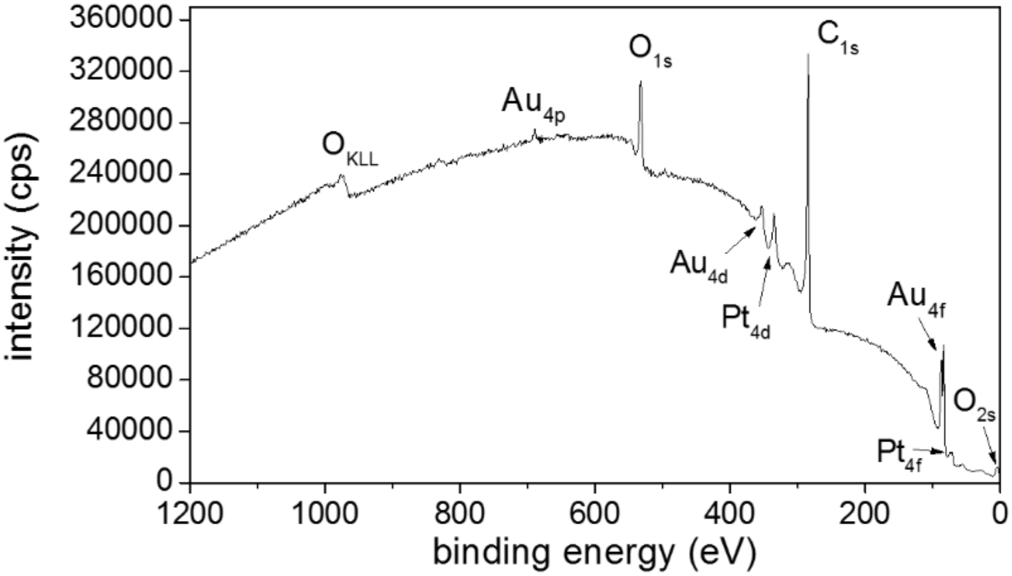

Figure 4.6 Survey X-ray photoelectron spectrum of a Au@PtNP-OP electrode.

Interactions between the Pt NPs and the Au-OP support were expected to have an impact on the electrochemical properties of Pt. The following electrochemical and material analyses evaluate the electrochemical and electrocatalytic properties of the supported Pt NPs and monitor the evolution and stability of the NP-support interactions with electrochemical cycling. Cyclic voltammetry analysis provides a synopsis of the characteristic electrochemical processes occurring at the surfaces of the Au@PtNP-OP electrodes (Fig. 4.5). These CV profiles enable the determination of $\boldsymbol{A}_{ecsa}$ of Au and Pt (as presented above), evaluation of the presence of surface contaminants, and insight into the influence of the Au support on the Pt interfacial properties.(Conway, et al., 1973; Rand & Woods, 1972; Tremiliosi-Filho, et al., 2005) The CV trace in Fig. 4.5 was obtained in 0.5 M H_2SO_4 at a scan rate (v) of 50 mVs^{-1} between 0.05 and 1.8 V (versus a reversible hydrogen electrode, or RHE). The electrode surface is relatively clean, as indicated by the centering of the CV about the baseline of I = 0.(Conway, et al., 1973) The CV traces exhibit peaks characteristic of both Pt and Au present on the surfaces of the Au@PtNP-OP electrode. These peaks are attributed to hydrogen underpotential deposition (H_{upd}) on Pt (adsorption and desorption), Pt oxide formation and reduction, and Au oxide formation and reduction. The Pt oxide formation and reduction peaks are shifted to higher and lower potentials, respectively, in comparison to sample containing only polycrystalline Pt. Contact between Pt NPs and either Au NPs or bulk-like Au supports is anticipated to alter the CV profile of Pt.(Ge, Yan, Wang, Tian, & Ding, 2009; J. Wang, et al., 2008; C. Xu, et al., 2010; J. Yang, Chen, Yang, & Ying, 2012; Jintao Zhang et al., 2008; J. Zhang, et al., 2007) These shifts in the CV profile of Pt have been observed when the Pt is in intimate contact with Au.(Awad, et al., 2007; Friedrich, Henglein, Stimming, & Unkauf, 2000; Ge, et al., 2009; Kristian et al., 2009; Senthil Kumar & Phani, 2009; Suntivich et al., 2013; Venkateswara Rao, Cabrera, & Ishikawa, 2011; Yan & Zhang, 2012; J. Zhang, et al., 2007) The lower work function of Au in comparison to Pt results in a donation of electron density from Au to Pt.(Kristian, et al., 2009) Correspondingly, an upwards shift in the d-band center is anticipated for Pt.(Hammer & Nørskov, 2000) The increase in negative charge at the Pt surfaces and shift in the d-band center result in stronger binding of the Pt with oxide species and a shift in the reduction potential to lower potentials, corresponding to the increased difficulty of Pt to gain electrons.(Hammer & Nørskov, 2000; Kristian, et al., 2009) This change in the electrochemical behavior of Pt has several implications on its electrochemical stability and electrocatalytic performance discussed later in this chapter.

Achieving a large Pt SSA ($\boldsymbol{A}_{\mathrm{ecsa,Pt}}/\mathrm{g}_{\mathrm{Pt}}$) is a challenge for ultrathin catalyst layer designs.(Mark K Debe, 2012; Mark K. Debe, 2012; O.-H. Kim, et al., 2013; Kinkead, van Drunen, et al., 2013) Traditional catalyst layers of C black/ionomer supported Pt NPs can readily achieve greater than 40 m^2 per g_{Pt}, while ultrathin designs typically achieve between 5 and 20 m^2 per g_{Pt}.(Mark K Debe, 2012; Liao, Li, & Li, 2008) Developing electrocatalyst architectures with a high Pt SSA, while maintaining an ultrathin design and the associated improvements in mass transport properties, could enable great improvements to electrocatalyst performance. Through determination of $\boldsymbol{A}_{\mathrm{ecsa,Pt}}$ by cyclic voltammetry and mass analysis by ICP-MS, the Pt SSA for Au@PtNP-OP electrodes was determined to be 27 ± 4 m^2 per g_{Pt}. This represents an ~ 40 % improvement over other ultrathin designs, such as previous reports on pure Pt-OP electrodes.(O.-H. Kim, et al., 2013; Kinkead, van Drunen, et al., 2013) The surface area enhancement factor (SEF) ($\boldsymbol{A}_{\mathrm{ecsa}}/\boldsymbol{A}_{\mathrm{geom}}$) of the Au@PtNP-OP electrodes was 6.1 ± 0.9 for Au and 1.1 ± 0.2 for Pt. The SEF for Pt is quite low (~1), but can be increased through a variety of methods with minimal impact on the high SSA. Examples include increasing the thickness of the Au@PtNP-OP electrodes, which would increase both Pt and Au SEFs, or increasing the loading of Pt NPs on the sacrificial PS templates to increase only the Pt SEF via an increase in Pt surface coverage on the Au.

In order to provide insight into the stability of the PtNP-Au support interactions and potential route for electrode degradation, the Au@PtNP-OP electrodes were subject to ~3.5 h of electrochemical cycling. The NP-support interactions were monitored by CV, XPS and CO stripping voltammetry. The Au@PtNP-OP electrodes were cycled between 0.05 and 1.25 V (vs. RHE) at a scan rate of 50 mVs^{-1} for 250 cycles. Scanning electron microscopy images of the Au@PtNP-OP electrodes after the 250 stability cycles were consistent in appearance to those obtained before the stability test (Fig. 4.7). Cyclic voltammetry traces between 0.05 and 1.8 V (vs. RHE) were obtained before and after this electrochemical stability test (Fig. 4.8). Notably, there is no significant change in the Pt H_{upd} adsorption and desorption region throughout the duration of this stability test, indicating no changes to the $\boldsymbol{A}_{ecsa,Pt}$. In comparison, pure Pt ordered porous electrodes or Pt NPs on C supports can lose up to 40% $\boldsymbol{A}_{ecsa,Pt}$ under the same or similar conditions.(Kinkead, van Drunen, et al., 2013; J. Zhang, et al., 2007) The values for $\boldsymbol{A}_{ecsa}$ of Au and Pt after the stability test were calculated to be 1.2 ± 0.3 cm^2 and 0.24 ± 0.03 cm^2, respectively. The small increase in measured $\boldsymbol{A}_{ecsa,Pt}$ (from 0.21± 0.03 cm^2) may be due to the removal of persistent organic contaminants, such as residual PS from the template preparation process, during the stability test (that were not removed by the initial 20 cycles between 0.05 and 1.8 V vs. RHE intended to clean the surfaces prior to the stability test).(Conway, et al., 1973) Shifts were also observed in the on-set potential of Au oxide formation/reduction peaks and the Pt oxide reduction peak. In addition to the possible removal of persistent organic contaminants, these shifts could indicate changes in the electrochemical properties of Pt or Au.(Conway, et al., 1973) Further insight into the source of these changes in peak position and shape were sought via XPS and CO stripping voltammetry analyses.

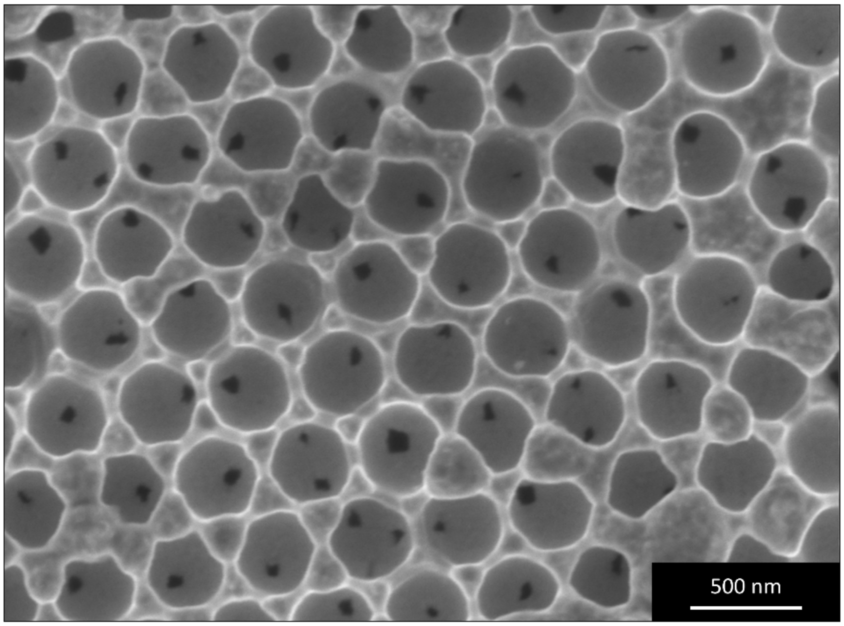

Figure 4.7 **Representative SEM image of a Au@PtNP-OP electrode after the electrochemical stability test.**

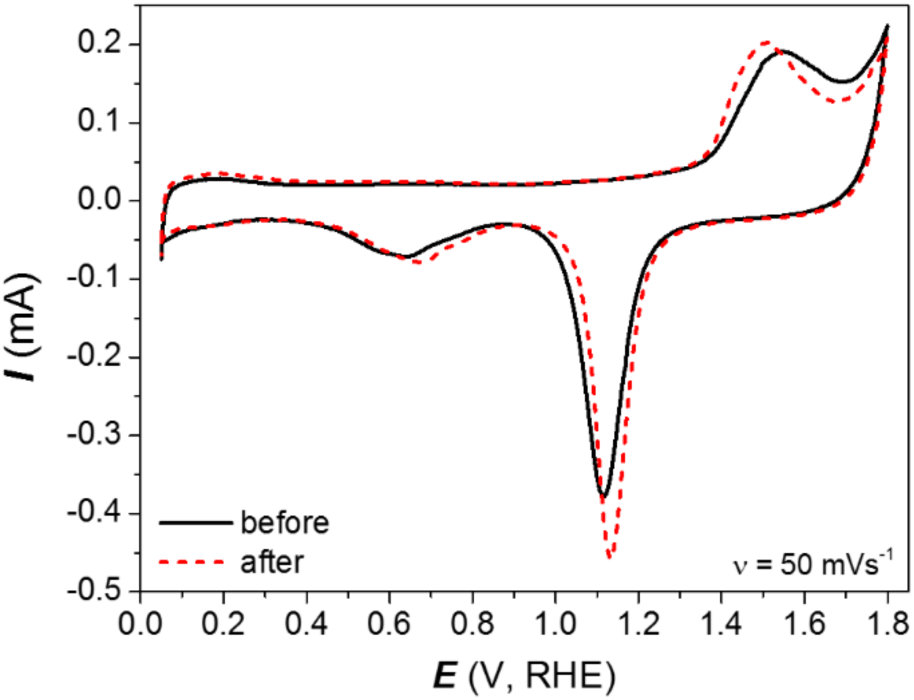

Figure 4.8 **Cyclic voltammetry traces obtained by cycling between 0.05 and 1.8 V at 50 mVs^{-1} in 0.5 M H_2SO_4 before and after the stability test.**

High resolution XPS analysis was sought to study the chemical environment of Pt and to provide insight into any changes in this environment with electrochemical cycling. High resolution XPS scans of Pt 4f were obtained before and after 250 electrochemical cycles to monitor changes to the NP-support interactions (Fig. 4.9). The total percent composition of oxides was 21 ± 3 % for Pt and 11 ± 3 % for Au. The higher concentration of oxides for Pt is anticipated due to the large relative percentage of surface exposed to air for the Pt NPs as compared to the porous Au support. The percent composition of oxides remained relatively constant for both Au and Pt after electrochemical cycling, suggesting that the morphology (e.g., size of the Pt NPs) has not changed significantly with electrochemical cycling. An increase in the overall intensity of the XPS peaks after cycling was also observed, due to the removal of surface impurities during electrochemical cycling. A similar trend was also observed for the XPS analysis of Au 4f (Fig. 4.10). The most notable change in the Pt 4f spectra after cycling is a shift in the Pt 4f 7/2 peak from 72.0 eV to 70.9 eV. This shift suggests that the Pt NPs have formed an alloy with the Au support.(Bastl & Pick, 2004; Ge, et al., 2009) A corresponding shift in the Au 4f XPS peak to higher binding energies would be anticipated, but is not observed due to the large proportion of Au on the electrode surface that is not in contact with Pt NPs and so is not available for alloy formation.(Bastl & Pick, 2004; Ge, et al., 2009) Upon forming an alloy, the Au donates electron density to the Pt NPs leading to the observed decrease in Pt 4f binding energy. This donation of electron density is anticipated to impact the interfacial properties and, correspondingly, the electrochemical properties of the Pt NPs. To probe this further, CO oxidative stripping voltammetry experiments were performed on these samples. This electrochemical experiment is highly sensitive to changes in Pt interfacial properties, such as faceting.(Urchaga, et al., 2011) In addition, no electrochemical reactions occur between CO and Au under the conditions used for the CO stripping experiments. Interference from the Au support is, therefore, minimal on the obtained voltammograms for Pt CO oxidative stripping.

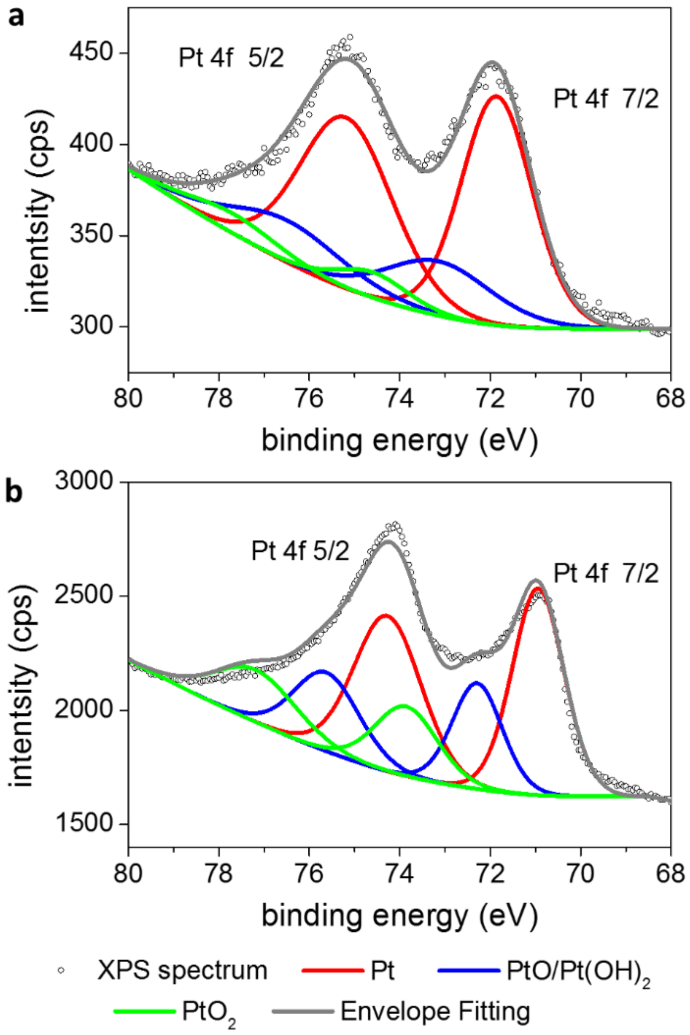

Figure 4.9 **High resolution Pt 4f X-Ray photoelectron spectra (a) before and (b) after the electrochemical stability test with fitting analysis.**

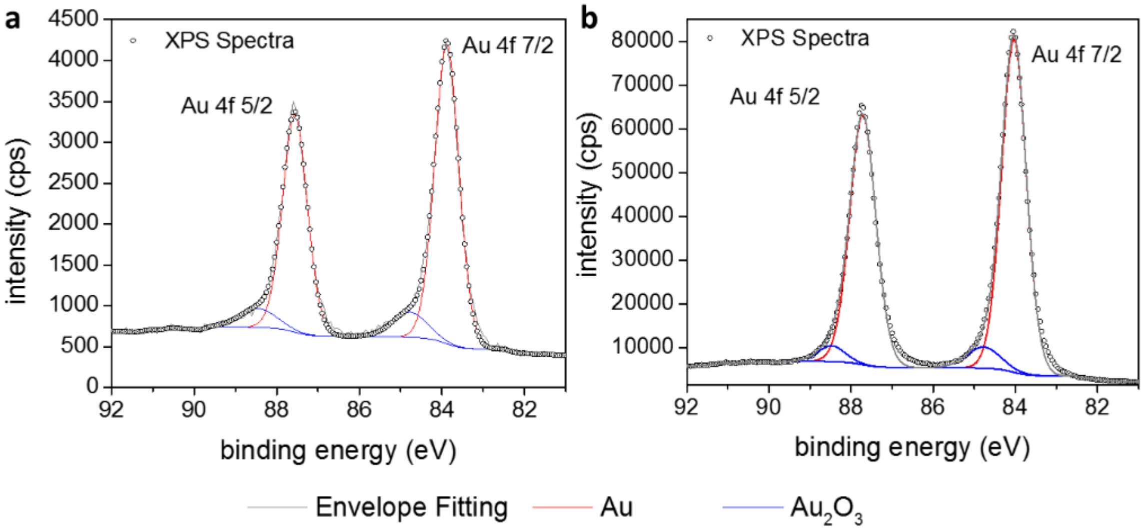

Figure 4.10 **High resolution Au 4f X-Ray photoelectron spectra (a) before and (b) after the electrochemical stability test with fitting analysis.**

Electrochemical CO oxidative stripping experiments provide insight into the interfacial properties of the Pt NPs in the Au@PtNP-OP electrodes. Fig 4.11 shows the CO oxidative stripping voltammogram profiles before and after stability testing with baseline correction to remove contributions from Au oxide formation (see Appendix D for the original CO oxidative stripping CV traces). The CO oxidative stripping profile of Pt generally consists of a pre-peak, seen here between 0.6 and 0.85 V (vs. RHE), followed by a main peak. The presence of this pre-peak is generally attributed to the presence of highly ordered facets of Pt.(Urchaga, et al., 2011) It is well-established in literature that CO oxidation from a Pt surface proceeds through the formation of oxide species on the Pt surface that nucleate the oxidation of CO.(Friedrich, et al., 2000; Urchaga, et al., 2011) For a polycrystalline Pt electrode, CO oxidation onsets at ~0.65 V. The onset potential for Pt within Au@PtNP-OP electrodes is positively shifted to 0.81 V. This positive shift indicates that the nucleation of CO oxidation is inhibited. Moreover, the onset potential is further positively shifted after the stability test to 0.86 V. A change in the shape of the Pt CO oxidative stripping profile is also observed after electrochemical cycling. After the stability test, the maxima of the peak is positively shifted. A similar phenomena was observed by Friedrech et al., who found that the CO oxidation onset and peak maxima positively shifted as the surface coverage of small (~3 nm diameter) Pt NPs decreased on a Au support.(Friedrich, et al., 2000) Similarly to Friedrech et al., the positive shift observed for CO oxidation from Pt in our studies could be the result of greater electron donation from the Au support. This finding agrees well with XPS findings, which indicated the formation of AuPt alloys during the stability test. This increase in electron density at the Pt surfaces increases the binding strength of Pt with its oxide and inhibits the nucleation of CO oxidation.(Hammer & Nørskov, 2000; Kristian, et al., 2009) After stability testing, the integrated area of the main peak in the CO oxidative stripping profile remains relatively constant. This consistency indicates that Pt NPs remain on the electrode surfaces without significant change in size. The $\boldsymbol{A}_{\mathrm{ecsa,Pt}}$ was also measured from analysis of the CO oxidative stripping profile and found to be consistent with analysis of the H_{upd} adsorption/desorption. Overall, SEM, CV, XPS and CO oxidative stripping analyses are in agreement that the composition and morphology of the Au@PtNP-OP electrodes remains constant throughout the stability test. These analyses also suggest that an alloy forms between the Au support and the Pt NPs. The constancy of $\boldsymbol{A}_{\mathrm{ecsa,Pt}}$ throughout the stability test is attributed to favorable interactions with the Au support.(J. Zhang, et al., 2007) The observed change in Pt interfacial properties as a result of the Au support is also anticipated to impact the electrocatalytic properties of Pt towards ORR and MOR.

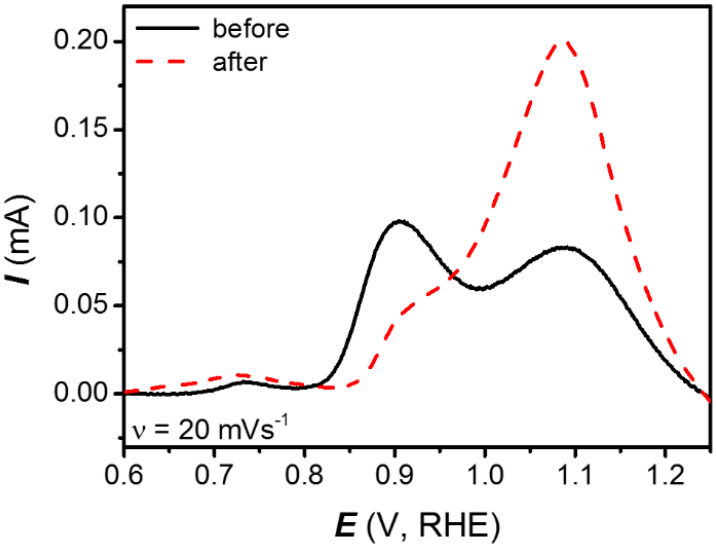

Figure 4.11 **Baseline corrected Pt CO oxidative stripping voltammogram traces before (solid black trace) and after (dashed red trace) the electrochemical stability test.**

Electrocatalytic activity of the Au@PtNP-OP electrodes towards ORR was evaluated by a rotating disk electrode (RDE) method. Linear sweep voltammograms (LSVs) of Au@PtNP-OP electrodes and commercial catalyst ink electrodes were obtained in O_2 saturated (1 atm) 0.5 M H_2SO_4 at various rotation speeds (Fig. 4.12). Note that this comparison was done by normalizing each curve by $\boldsymbol{A}_{\mathrm{ecsa,Pt}}$. Attempts to compare the data by normalizing to Pt mass were unsuccessful, due to the huge disparity in the mass of Pt for the catalyst ink electrodes (~ 0.7 mg per electrode) versus the Au@PtNP-OP electrodes (~ $6 \cdot 10^{-7}$ mg per electrode). Oxygen reduction onsets on the Au@PtNP-OP electrodes at ~ 0.85 V vs. RHE, or an overpotential (η) of ~ 0.4 V. This overpotential is ~ 0.1 V larger than for the commercial catalyst ink electrodes; ORR generally onsets at an overpotential of ~ 0.3 V for Pt NPs supported on C black under similar conditions (e.g., temperature and electrolyte).(Paulus, et al., 2001) The current generated by ORR at the surfaces of the Au@PtNP-OP electrode is primarily from the Pt NPs. Only a small amount of current is generated due to ORR at the Au surfaces at η > 0.7 V (Fig. 4.13). Interestingly, the electrocatalytic properties of the Au@PtNP-OP electrodes towards ORR remain mostly constant after the stability test (and observed formation of a Pt/Au alloy) (Fig. 4.14). Note that Fig. 4.14 and 4.12 correspond with two separately prepared Au@PtNP-OP electrodes (these LSVs were normalized by $\boldsymbol{A}_{\mathrm{ecsa,Pt}}$). Comparing these LSVs reveals that the profiles are relatively consistent with a small variance that may be attributed to differences in O_2 content, Au@PtNP-OP electrode morphology and/or impurities in the electrolyte. Levich plots, such as that shown in Fig. 4.15, have been generated for analysis of the kinetic parameter of Au@PtNP-OP electrodes before and after the stability test. This analysis found that the kinetic parameter also remained relatively constant after the stability test and was calculated to be 3.14 ± 0.04. This indicates that ORR proceeds through a combination of direct (4 e^- transfer) and indirect (2 e^- transfer via a peroxide intermediate) pathways on the Pt NPs supported on OP gold.(C. Song & Zhang, 2008)

The delay in onset potential for Pt/Au electrodes has been observed by other researchers for Au-rich systems.(S. Guo, et al., 2007; Luo, Njoki, Lin, Wang, & Zhong, 2006; Senthil Kumar & Phani, 2009) Similarly, a kinetic parameter of ~3 has been previously reported for a Au-rich Au/Pt electrocatalytic systems.(Luo, et al., 2006) The binding of oxygen to the catalyst surface is known to be a key step in the electrocatalytic reduction of oxygen. Platinum is suggested to bind oxygen-containing species with greater strength than is necessary, limiting the rate of removal of adsorbates and, consequently, increasing ORR η. Pt/Au alloys are expected to bind oxygen more strongly than Pt based on electronic arguments.(M. Shao, et al., 2010) A correlation between the shift in the Pt oxide reduction peak and the observed ORR onset potential for Au@PtNP-OP electrodes suggests that this delayed onset potential is due to electron donation from the Au support and a corresponding increase in binding strength of Pt with oxygen-containing species.(Hammer & Nørskov, 2000; Kristian, et al., 2009) The growth of a Pt "skin" onto a Au surface or Au nanoparticle has been shown to enhance the activity of Pt towards ORR due to compressive strain effects, which exist due to the slight lattice mismatch between Pt and Au.(Pedersen et al., 1999; M. Shao, et al., 2010) The Au@PtNP-OP electrodes are not anticipated to exhibit this behavior since they are not of a core-shell morphology. Despite the delay in onset of ORR on the surfaces of the Au@PtNP-OP electrodes, the limiting current density (per $\boldsymbol{A}_{\mathrm{ecsa,Pt}}$) achieved for Au@PtNP-OP electrodes is ~6 times greater than for the commercial catalyst ink electrodes. This high current density at large η is due to the ultra-low loading of Pt at the surfaces of the Au@PtNP-OP elecrodes.(Y. Sun, Lu, & Zhuang, 2010; Zalitis, Kramer, & Kucernak, 2013) The low loading of Pt effectively reduces the kinetic current and enables measurement at higher overpotentials. Enhanced performance at high η for ordered macroporous catalyst layers was observed by Sung et al. and attributed to morphological advantages of the OP design.(O.-H. Kim, et al., 2013) To evaluate the impact of the ordered porous morphology on the RDE results, RDE analysis was performed on pure-Pt ordered porous electrodes of varying porosity (Fig 4.16).

Pure Pt-OP electrodes with varying porosity were prepared on the GC disks via an analogous method to that of the Au@PtNP-OP electrodes, but with electrodeposition of Pt as per our previous report.(Kinkead, van Drunen, et al., 2013) Two electrodes of varying porosity were prepared by electrodepositing Pt to different thicknesses. The first electrode is non-porous with a Pt thickness of < 100-nm, producing a Pt "macro-bowl" array. The second electrode contains a Pt deposit of ~400-nm thickness, producing an ordered macroporous Pt electrode (Pt-OP). Representative ORR RDE LSVs obtained in O_2 sat. (1 atm) 0.1 M aqueous H_2SO_4 at 900 rpm are displayed in Fig 4.16. The "macro-bowl" type electrode exhibits a considerably larger limiting current density (current normalized by $A_{\mathrm{ecsa,Pt}}$) than the Pt-OP electrode. This result suggests that electrolyte does not penetrate the OP electrode during RDE analysis, such that only the outer surface contributes to the currents measured during the LSV. As a result, the evaluated current density for the porous electrode is artificially lower, since it is normalized by the total $A_{ecsa,Pt}$ (which includes the inner pore surfaces). Although the morphological advantage of the OP morphology was not observable by RDE analysis, it is anticipated that the Au@PtNP-OP electrodes would also exhibit the morphological advantages observed by Sung et al. for their pure Pt OP fuel cell catalyst layer, due to similarities in the OP morphologies of these designs. The Au@PtNP-OP electrocatalysts are, therefore, anticipated to have very good mass transport properties, owing to their ultra-low Pt loading and open macroporous morphology.

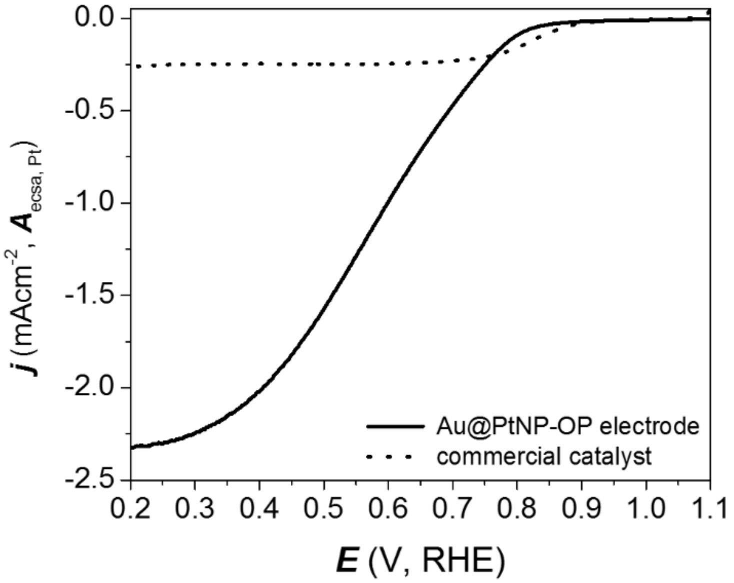

Figure 4.12 **Representative RDE linear sweep voltammograms profiles obtained in O_2 saturated (1 atm, 0.5 M H2SO4 at 900 rpm, v = 10 mVs-1) for a Au@PtNP-OP electrode (red trace) and a commercial catalyst ink electrode (black trace). The current is normalized by Aecsa,Pt.**

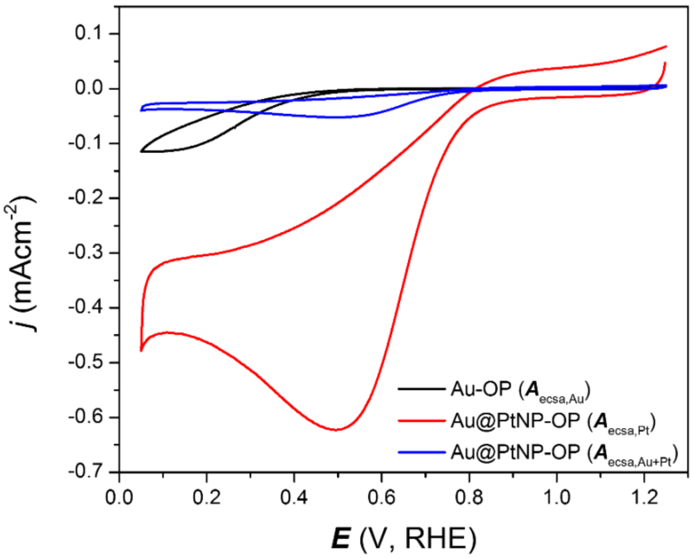

Figure 4.13 **Cyclic voltammetry trace of Au-OP (black trace) and Au@PtNP-OP electrodes (red and blue traces) obtained in oxygen saturated (1 atm.) 0.5 M H_2SO_4 at a scan rate of 20 mVs^{-1} with current normalized by either $A_{ecsa,Au}$, $A_{ecsa,Pt}$ or the sum of $A_{ecsa,Au}$ and $A_{ecsa,Pt}$ ($A_{ecsa,Au+Pt}$).**

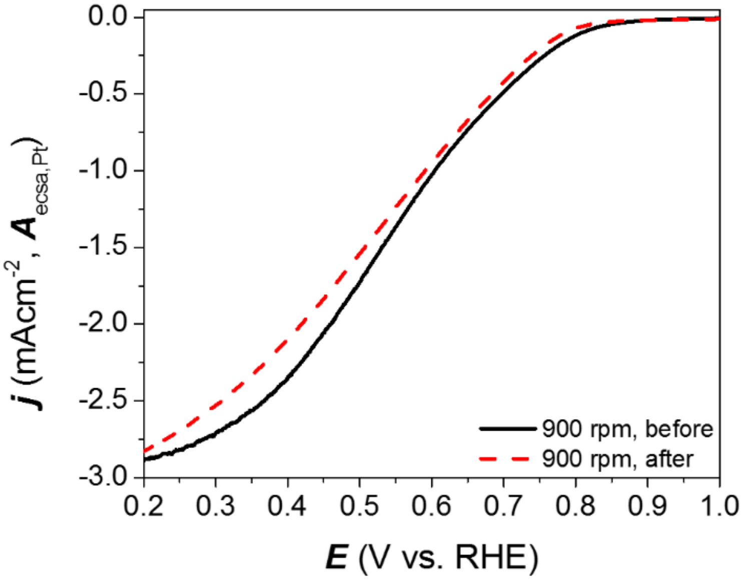

Figure 4.14 **Representative RDE linear sweep voltammogram profiles obtained in O_2 saturated (1 atm, 0.5 M H_2SO_4 at 900 rpm, v = 10 mVs^{-1}) before (solid trace) and after (dashed trace) the electrochemical stability test. The current is normalized by $A_{ecsa,Pt}$.**

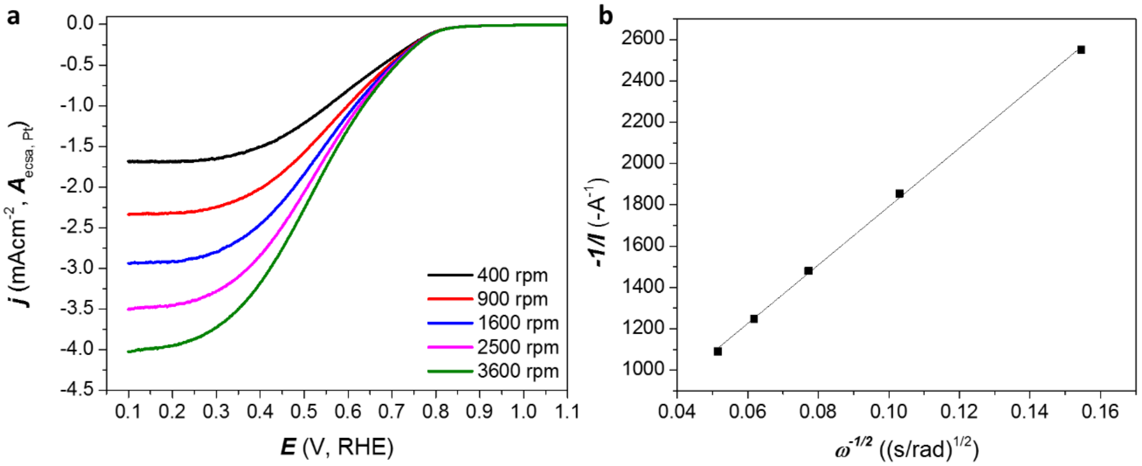

Figure 4.15 **(a) Linear sweep voltammograms obtained by scanning from 1.1 to 0.1 V vs. RHE in O_2 saturated (1 atm) 0.5 M H_2SO_4 at v = 10 mVs^{-1} at varying rotation rates using a rotating disk electrode setup. (b) Levich plot derived from the linear sweep voltammograms shown in (a) for derivation of the kinetic parameter.**

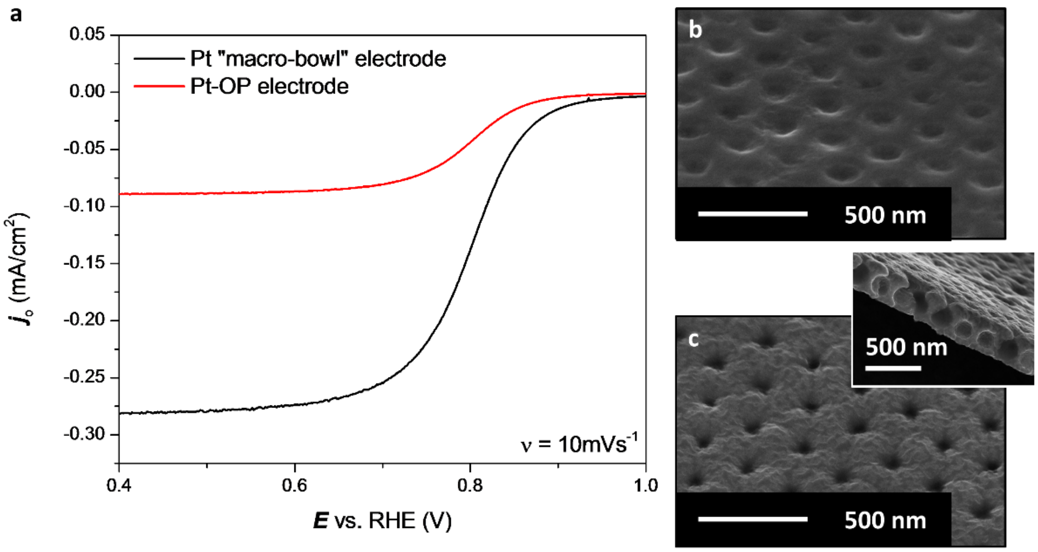

Figure 4.16 **a) Representative ORR RDE LSVs obtained in O_2 sat. (1 atm) 0.1 M aqueous H_2SO_4 at 900 rpm for Pt "macro-bowl" array and Pt-OP electrodes. Representative SEM images of b) the "macro-bowl" array electrode and c) the Pt-OP electrode (inset shows a cross-sectional view at 60° tilt to normal).**

The MeOH oxidation activity of the Au@PtNP-OP electrodes was also assessed (Fig. 4.17) via cyclic voltammetry in MeOH containing electrolyte (1 M MeOH, 0.5 M H_2SO_4). In previous literature, Au/Pt electrocatalysts have been pursued as MeOH tolerant ORR catalysts for DMFCs due to their catalytic selectivity depending on the composition and structure of the Au/Pt material.(Hernández-Fernández, et al., 2008; Lamy, et al., 2009; Senthil Kumar & Phani, 2009; Suntivich, et al., 2013; J. Wang, et al., 2008) The Au@PtNP-OP electrodes catalyze the oxidation of MeOH considerably less than a commercial catalyst ink electrode (normalized by $\boldsymbol{A}_{\text{ecsa,Pt}}$) with a peak current density of ~0.25 mAcm^{-2} for Au@PtNP-OP electrodes, in comparison to ~0.7 mAcm^{-2} for the commercial catalyst ink electrodes. This behavior is anticipated based on previous literature,(Hernández-Fernández, et al., 2008; Lamy, et al., 2009; Senthil Kumar & Phani, 2009; Suntivich, et al., 2013; J. Wang, et al., 2008) which reports that Au-rich Au/Pt systems tend to be poor catalysts for MeOH oxidation. Additionally, MOR only occurs at potentials less than ~0.8 V (vs. RHE) on the Au@PtNP-OP electrodes. In comparison, current from MOR on the surfaces of the catalyst ink electrode is observed at potentials as great as 1.05 V (vs. RHE). A shift in the onset of MOR for a Au rich Au/Pt system was also observed in a recent report by Fierro et al., although it was not extensively discussed in text.(Hernández-Fernández, et al., 2008) Methanol oxidation on Pt surfaces proceeds through MeOH adsorption and dehydrogenation across at least three neighboring Pt atoms.(Hernández-Fernández, et al., 2008; Lamy et al., 2002) The low current generated from MOR at the surfaces of the Au@PtNP-OP electrodes may be due to a lower possibility in finding three neighbouring Pt sites in a suitable arrangement.(Hernández-Fernández, et al., 2008) The shift in onset of MOR on the Au@PtNP-OP electrodes is suggested here to be a result of electron donation from the Au support to the Pt NPs. This electron donation could increase the negative charge at the Pt surfaces and inhibit the adsorption of MeOH at higher potentials (less oxidizing). The low current and shifted onset potential for the electrocatalysis of MOR at the surfaces of Au@PtNP-OP electrodes, combined with their good ORR electrocatalytic properties, make Au@PtNP-OP electrodes ideal for application as a methanol-tolerant ORR catalyst in DMFC technologies.(Antolini, Lopes, & Gonzalez, 2008)

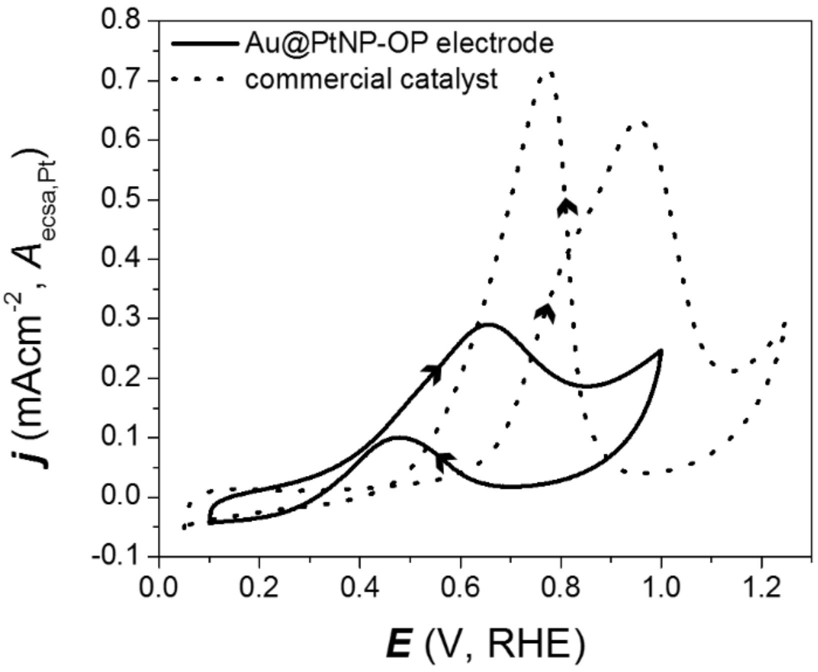

Figure 4.17 Representative CV traces obtained in 1M methanol, 0.5 M H_2SO_4 at a scan rate of 20 mVs^{-1} with current normalized by $A_{ecsa,Pt}$ for a Au@PtNP-OP electrode and a commercial catalyst ink electrode.

4.5. Conclusions

The successful preparation of Au@PtNP-OP electrodes was confirmed by XPS, SEM, TEM and CV analysis. A large Pt SSA, in comparison to other ultrathin designs, of 27 ± 4 m^2 per g_{Pt} was achieved using these porous electrodes. A small SEF was measured, but could be increased through a variety of methods. An electrochemical stability test was performed by scanning between 0.05 and 1.25 V vs. RHE for 250 sequential cycles. Throughout this stability test, the $\boldsymbol{A}_{ecsa,\ Pt}$ remained constant. Alloying of Pt with the Au support during the stability test was detected by CO oxidative stripping and XPS analyses. The onset of ORR catalysis for the Au@PtNP-OP electrodes was found be at $\boldsymbol{n} \approx 0.4$ V, which is greater than for C black supported Pt electrocatalysts ($\boldsymbol{n} \approx 0.3$ V). A comparison by RDE analysis was sought for Au@PtNP-OP electrodes and commercial catalyst ink electrodes. This comparison found that the limiting current density (per $\boldsymbol{A}_{ecsa,Pt}$) is ~6 times greater for Au@PtNP-OP electrodes than for the commercial catalyst ink electrodes. This enhancement is attributed to the effective utilization of Pt within the Au@PtNP-OP architecture via morphological advantages of the Au@PtNP-OP design (improved mass transport).(O.-H. Kim, et al., 2013) The inhibited activity of Au@PtNP-OP electrodes towards MOR makes these electrodes suitable for cathodic application in DMFCs, where MeOH crossover from the anode limits achievable ORR currents. The new architecture demonstrated in the Au@PtNP-OP electrodes also holds great promise for further development, such as through modification of the NPs and/or supporting material, to create highly efficient electrocatalysts.

Chapter 5.

Support@Platinum-Nanoparticle Nanobowls

5.1. Notice of Permissions

A manuscript based on the work presented in this chapter is currently in preparation. Permissions to use this material has been granted by all co-authors of this manuscript in progress. Austin W. Lee assisted in materials preparation (primarily the PVD of TiO_2). Dr. Michael Wang and Dr. Xin Zhang assisted in performing STEM tomography analysis. All other experiments were performed by myself. A report on my work in the area of support@Pt-NP nanbowls has also been submitted for publication in the 2014 Winter issue of ECS Interfaces, in follow-up to the ECS F. M. Becket Summer Research Fellowship. The material presented in this report is not reproduced here, but is mentioned here for reference only.

5.2. Introduction

At present, carbon is the most commonly used material for the support of Pt NP electrocatalysts in low temperature fuel cell applications. This support provides a high surface area for dispersion of the Pt NPs and good conductivity, but has limited stability under fuel cell operating conditions.(Mark K Debe, 2012; Y.-J. Wang, et al., 2011) Therefore, alternative support materials are being pursued to increase the stability of Pt-based catalyst layers, such as Au(Awad, et al., 2007; Kristian, et al., 2009) or metal oxides(Hayden, et al., 2009; Lewera, Timperman, Roguska, & Alonso-Vante, 2011) (and combinations of Au or metal oxides with C black)(Kristian, et al., 2009; Sasaki, et al., 2008; J. Zhang, et al., 2007).(Y.-J. Wang, et al., 2011) Interactions with these supports can improve durability and/or catalytic activity through electronic effects or support interactions that alter the catalytic pathway. Designing catalyst layers that incorporate these new supports presents a significant challenge. Gold is an expensive metal and so minimizing the mass of Au in the catalyst layer is necessary to minimize cost. Metal oxides are generally poor conductors, and so catalytic turnover can be limited in these catalyst layer designs by efficient electron conduction to the Pt catalysts.(S.-Y. Huang, Ganesan, & Popov, 2012; Lewera, et al., 2011; Y.-J. Wang, et al., 2011) Herein, a novel catalyst layer design consisting of Pt NPs dispersed over the inner surface of nanobowl (NB) supports is described. These support@PtNP NBs are prepared by a modular sacrificial template method, providing fine control over support composition and Pt NP properties. Previous reports have demonstrated the preparation of NBs (or half-shells),(Cho, Kim, Shim, Lee, & Lee, 2013; Love, Gates, Wolfe, Paul, & Whitesides, 2002; Lu et al., 2013; X. D. Wang, Graugnard, King, Wang, & Summers, 2004; Y. Wang et al., 2008; M. Xu et al., 2009; Ye, Van Dorpe, Van Roy, Borghs, & Maes, 2009) generally for optical applications and without NP decoration. This chapter is the first report to our knowledge on the preparation of NP decorated NBs with controlled distribution of NPs (via transfer from a spherical template). This new nanomaterial offers a number of advantages as an electrocatalytic material over traditional catalyst ink designs containing Pt NPs dispersed onto C black: i) the support material can be varied to optimize the support properties to ensure good conductivity, and enable enhanced Pt electrocatalytic activity and stability;(Y.-J. Wang, et al., 2011) ii) the distribution of Pt NPs is controlled over the surfaces of the NBs as to ensure a high surface area to mass ratio; iii) the 3D morphology of the NBs also promotes macroporosity in the catalyst layer, which has implications on the mass transport and water management properties of the prepared catalyst layer.(O.-H. Kim, et al., 2013) The work described in this chapter demonstrates the preparation and characterization Pt NP functionalized nanobowls (support@PtNP NBs) with three different nanobowl compositions. Gold nanobowl (Au@PtNP NBs) supports were pursued herein for the reported ability of Au supports to enhance the activity and stability of Pt NP catalysts.(Gu, Cong, & Ding, 2010; Jeong, Kim, Kim, Kim, & Baeck, 2012; Jia, Cao, & Wang, 2008; J. Zhang, et al., 2007; Q. Zhang, et al., 2013; Zhao & Xu, 2006) Titanium oxide nanobowl supports (TiO_2@PtNP NBs) are pursued for similar reasons, with the added benefit of a lower material cost for titania (in comparison to Au).(X. Guo, Guo, Qiu, Chen, & Zhu, 2009; S.-Y. Huang, Ganesan, & Popov, 2011) The low conductivity of TiO_2 may limit electron conduction to the Pt NPs, inhibiting electrocatalysis at the Pt surfaces.(Y.-J. Wang, et al., 2011) Therefore, a third design containing both Au and TiO_2 within the NB has been prepared. These Au/TiO_2@PtNP NBs have a thin (~10-nm) nm shell of TiO_2 (in direct contact with the Pt NPs) and a thicker (~25-nm) Au shell. The outer Au shell will primarily conduct electrons between NBs, such that electrons will only need to pass through TiO_2 to the Pt NPs from the Au shell (TiO_2 will not have to act as the primary electron conductor within the catalyst design). These thicknesses and compositions can also be readily tuned in future studies to optimize catalytic performance via the tunable method developed here. The materials prepared here serve to demonstrate the general utility of this method in preparing electrocatalyst materials with a favorable morphology and with supports of varying composition for optimizing the electrocatalytic performance of Pt NPs for a range of different reactions.

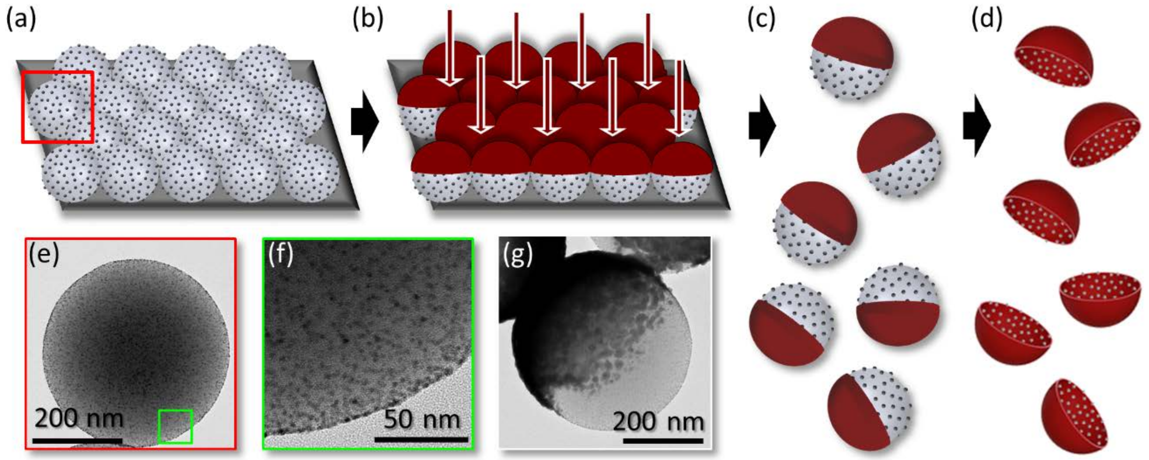

Figure 5.1 **Schematic describing the preparation of support@PtNP nanobowls. (a) Pt NP decorated PS spheres are assembled into a close-packed array onto a clean Si wafer. (b) The top surface of the PS sphere array is coated with the support material of interest by physical vapor deposition. (c) Anisotropically coated PS spheres are released from the polished Si wafer by sonication in ethanol. (d) Reflux of the anistropic spheres in organic solvents dissolves the PS spheres and reveals the support@PtNP nanobowls. Transmission electron microscopy (TEM) images of a Pt NP decorated PS sphere at (e) low and (f) high magnification and (g) an anisotropically coated Pt NP decorated PS spheres (with gold) are also shown.**

5.3. Experimental

The support@PtNP nanobowls are prepared through a sacrificial template method as seen in Fig. 5.1. This modular sacrificial template method proceeded through a number of steps: i) Pt NPs were synthesized and decorated onto the surfaces of polystyrene (PS) spheres; ii) the decorated PS spheres were assembled into a single close-packed layer onto a Si wafer; iii) the exposed top surfaces of the Pt NP decorated PS spheres were coated by PVD; iv) the asymmetrically coated Pt NP decorated PS spheres were removed from the Si wafer by sonication; v) PS spheres were dissolved in refluxing organic solvents, revealing the support@PtNP nanobowls.

All chemicals were used as received without any further purification. All glassware and stir bars were treated with aqua regia and piranha prior to use. The aqua regia solution was prepared from a 3:1 (v/v) solution of hydrochloric acid (36.5 – 38.0% in water; Anachemia Inc.) and nitric acid (68 – 70% in water; Anachemia Inc.). The piranha solution was prepared from a 5:2 (v/v) solution of concentrated sulfuric acid (90 - 100% in water; Anachemia Inc.) and hydrogen peroxide (30% in water; Caledon Laboratories Ltd.). *CAUTION: Aqua regia and piranha solutions should be handled with extreme care.* Polyvinylpyrrolidone (PVP) (55k MW, 98%) and hexachloroplatinic acid (H_2PtCl_6, ACS grade) were purchased from Sigma-Aldrich.

Platinum NPs were synthesized by an alcohol reduction method(Teranishi, et al., 1999) and subsequently decorated onto the surfaces of amine functionalized PS spheres.(I. W. Guo, et al., 2014; Kinkead, Ali, et al., 2013) The PS spheres served as a template for the formation of the NB shape and as a surface for assembly of Pt NPs with controlled distribution. In brief, a 6 mM H_2PtCl_6 solution in deionized water (18 MΩ·cm, produced using a Barnstead NANOpure DIamond water filtration system) was prepared 1 day in advance. A solution containing 40 mL of EtOH, 5 mL of demineralized water, and 1.65 g of 55k MW PVP was prepared and allowed to stir for 10 min in a 100 mL round bottom flask equipped with a reflux condenser and stir bar before addition of 5.0 mL of the 6.0 mM Pt solution. This mixture was brought to reflux with continuous stirring and held at reflux for 6 h. The resulting solution was removed from heat and slowly cooled to room temperature. Amine functionalized PS spheres (2.5 mL, 2 wt% solution, Polysciences Inc., ~ 420 nm diameter) were washed twice by centrifugation (11,000 rpm, 10 min) in an ~ 1:1 mixture of EtOH and deionized water. The PS spheres were then added to the Pt NP solution and warmed to 55°C under continuous stirring. After 3 h at 55°C under continuous stirring, the Pt NP decorated PS spheres were allowed to cool to room temperature and separated from the solution by centrifugation (8,500 rpm, 25 min). Residual Pt NPs (not adhered to the PS sphere surfaces) were removed from solution by removal of the NP containing supernatant, re-dispersion in water, and separation by centrifugation (8,500 rpm, 25 min). This process was repeated 2 more times with EtOH. The Pt NP decorated spheres were then dried in a vacuum desiccator for ~2 h to remove any residual solvents remaining from the washing process.

The Pt NP decorated PS spheres were assembled onto a flat surface into a single close packed layer prior to coating via PVD to ensure the uniform preparation of support@PtNP NBs.(Kinkead, van Drunen, et al., 2013; Moon, et al., 2011) In brief, the dried Pt NP decorated PS spheres were dispersed in 5 mL of 1-BuOH by sonication for ~ 10 min. This 1-BuOH solution of PS spheres was cast drop-wise onto the surface of warm (55°C) deionized water contained in a glass dish until the surface of the water was fully covered by the PS spheres (see Appendix A for details). This water bath was then allowed to slowly cool to room temperature (~1 h). The polished surface of a clean Si wafer was rinsed with EtOH and dipped into the water sub-phase. The close packed PS sphere assembly was transferred to the Si wafer upon careful removal of the Si wafer from the water sub-phase through the PS assembly at an angle of ~ 45°. The PS sphere assemblies (on Si wafer supports) were then dried in a vacuum desiccator overnight and generously rinsed with ethanol to removal any 1-BuOH residues prior to PVD treatment. Gold was deposited onto the PS spheres *via* thermal evaporation in a Kurt J. Lesker physical vapour deposition system at a rate of 0.8-1.0nm/min. The thickness of Au deposited for Au@PtNP and Au/TiO_2@PtNP NBs was 35 and 25 nm, respectively, based on the quartz crystal measurement system within the PVD system. TiO_2 was deposited using a Kurt J. Lesker sputtering system with a TiO_2 target at a rate of ~ 0.17nm/min [AC power source, 140W (ramp rate 0.2W), 100% Ar gas composition during sputtering, Chapman pressure 3mTorr].

Physical vapor deposition coating of the PS spheres is asymmetric, in that the deposit is primarily on the top surface of the spheres. This asymmetry in the coating enables the formation of the NB (or half-shell) materials sought here.(Love, et al., 2002) The asymmetrically coated (Janus-type) Pt NP decorated PS spheres were released from the Si wafer substrates by sonication in EtOH, separated from by centrifugation (10,000 rpm, 5 min) and re-dispersed in 10 mL of acetone.(Love, et al., 2002) The acetone solution was combined with 10 mL of hexanes and 10 mL of toluene in a 50 mL round bottom flask equipped with a reflux condenser and stir bar. This solution was brought to reflux and held at reflux for 6 h under continuous stirring as to completely dissolve the PS sphere templates. After cooling to room temperature, the support@PtNP NBs were washed 2 times each with ~10 mL of hexanes and acetone and subsequently dispersed in isopropanol. The NBs were cast onto transmission electron microscopy (TEM) grids (C/Formvar coated 300 mesh Cu, Ted Pella Inc.) for TEM analysis and glassy carbon (GC) substrates (Pine Instrument Company, 5 mm OD) for scanning electron microscopy (SEM) and X-ray diffraction (XRD) analysis. The TiO_2@PtNP and Au/TiO_2@PtNP NBs on GC supports were annealed at 450°C for 2 hours to form anatase TiO_2 (see Appendix E for details).

The support@PtNP nanobowls were characterized by a number of methods to evaluate their material properties. Transmission electron microscopy and STEM analyses were performed using a FEI Osirus X-FEG S/TEM equipped with a Super-X energy EDS detection system. Scanning TEM tomography analysis was performed on this instrument using a calibrated Fischione single tilt tomography holder between -60° and 60° tilt (to normal) and Amira software for 3-D reconstruction. The tomography sample was prepared on a 300 mesh Cu TEM grid coated with ultrathin carbon on a carbon holey support film (Ted Pella Inc.). Scanning electron microscopy analysis of a drop-casted dispersion of the NBs was performed using a FEI Helios SEM/FIB operating at 5 kV with a stage bias of 50 mV. X-ray diffraction analysis was performed using a Rigaku Rapid-Axis Diffractometer with a Cu Kα1 radiation source ($\lambda = 1.5406$ Å) with a 0.5 mm collimator.

5.4. Results and Discussion

The successful preparation of support@PtNP nanobowls via the modular sacrificial template method described in Fig. 5.1 was confirmed through STEM/EDS analysis (Fig. 5.2). Platinum NPs are seen on the inner surface of the NBs and not on the outer edges, confirming direct transfer of the NPs from the surfaces of the PS spheres to the surfaces of the support NB. The Pt NPs are especially evident in the EDS maps for the TiO_2@PtNP NBs (Fig. 5.2b) due to the large difference in z-contrast between TiO_2 and Pt. After transfer to a nanobowl support, the Pt NP size remains the same within experimental error (Fig. 5.3, Pt NP diameter of 2.4 ± 0.5 nm before and 2.6 ± 0.5 nm after). This diameter of Pt NP (between 2 and 3 nm) is desirable for high electrocatalytic activity and a large surface area to mass ratio.(Nesselberger, et al., 2013; Nørskov, et al., 2004) In addition, annealing of the TiO_2 containing NBs does not change the size or distribution of the Pt NPs over the surface of the NBs, as evident in STEM analysis (see Appendix E). The % surface area covered by the Pt NPs on the surfaces of the PS spheres (before transfer) and % surface area covered by the Pt NPs on the surfaces of the nanobowls (after transfer) is that same, at 15 ± 5 %. This is indicative of a quantitative transfer of Pt NPs from the PS sphere template to the support NBs (not considering that ~ ½ of the NPs coating the PS spheres will not be transferred to the NB support). The ability to tune the properties of the Pt nanocatalysts (e.g., dimensions and surface coverage) prior to transfer and maintain these properties on the NB support is an important aspect of this work, as it provides fine control over the final electrocatalyst properties.

A minimal thickness of the NBs was sought to reduce material costs associated with the support, while maintaining a bowl-like shape in the prepared nanomaterials. A NB thickness of ~35 nm was found to be required for the method presented here, in order for the NBs to retain their hemispherical shape. The bowl-like shape of the NBs was confirmed through STEM tomography analysis of a sample of Au@PtNP NBs (Fig. 5.4). Although artifacts in the STEM tomography reconstruction are present (mostly from difficulties in aligning the reconstruction), it can clearly be seen that the material (with ~35 nm thick Au) has a bowl-like shape. At smaller thicknesses, the NBs tended to flatten and/or flake into smaller pieces upon handling (e.g., sonication, drying onto the

TEM grid) (Fig. 5.4). The thickness of the TiO_2, Au/TiO_2, and Au NBs, as measured for multiple samples by TEM analysis near the thickest region of the NBs, are 39 ± 5 nm, 34 ± 5 nm (Au is 23 ± 5 nm, TiO_2 is 9 ± 3 nm) and 37 ± 4 nm, respectively. Note that the Au and TiO_2 individual thicknesses are measured from elemental maps obtained through EDS analysis (such as those seen in Fig. 5.2) of a small number of NBs, resulting in the apparent difference between the total thickness and the added thickness of each component. The shape of the NBs was also found to be stable to sonication, which was used to disperse the samples prior to TEM analysis. This stability is necessary to ensure the support@PtNP materials can be incorporated into an electrocatalyst device without changes to the NB morphology.

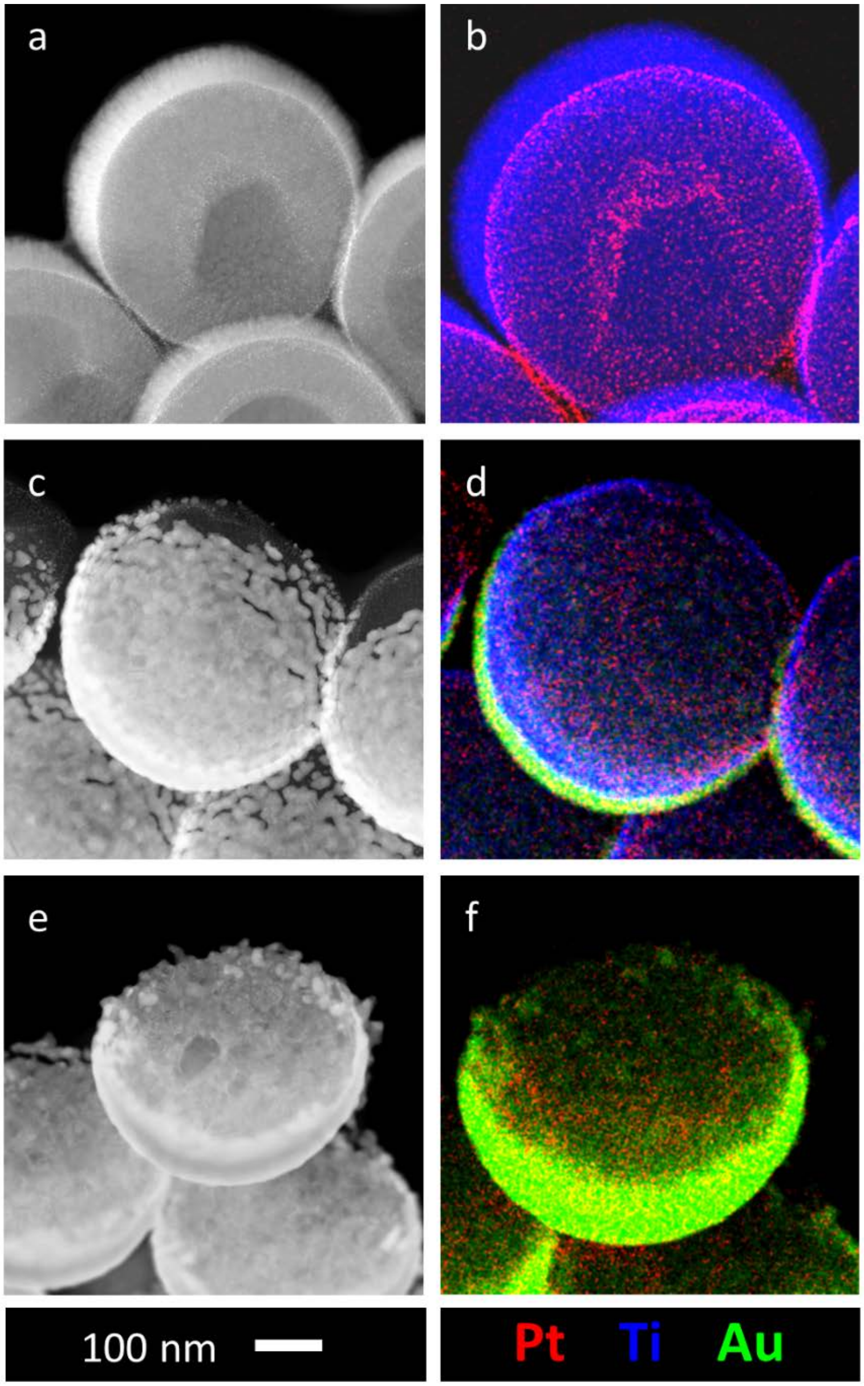

Figure 5.2 (a,c,e) Scanning TEM images and (b,d,f) energy dispersive X-ray spectroscopy element maps of (a,b) TiO_2@PtNP, (c,d) Au/TiO_2@PtNP, and (e,f) Au@PtNP nanobowls.

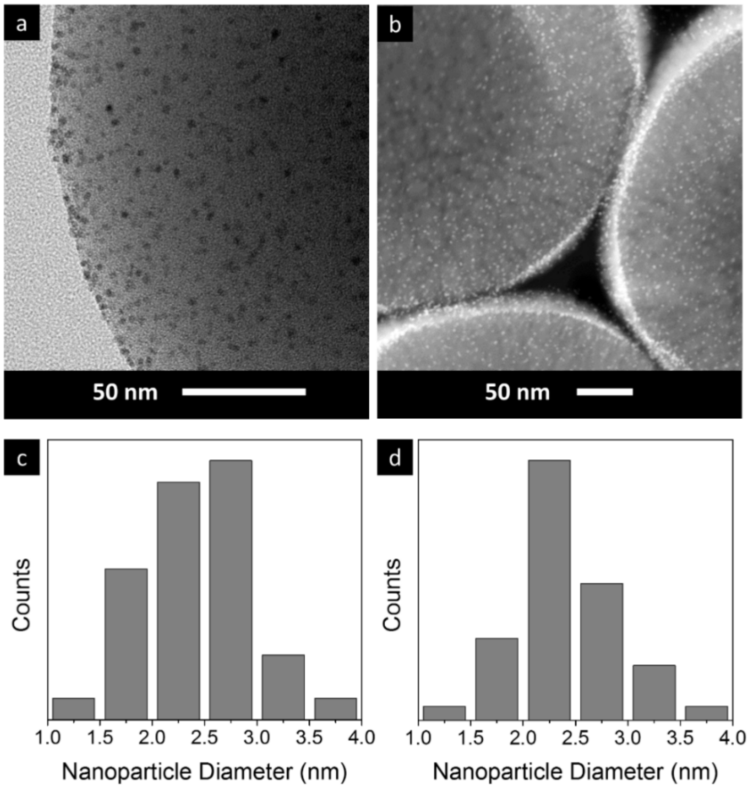

Figure 5.3 High magnification (a) TEM image of a PS@NPs template and (b) STEM image of a TiO_2@PtNP NB with corresponding histograms of Pt NP diameter: (c) PS@NPs; (d) TiO_2@PtNP NB.

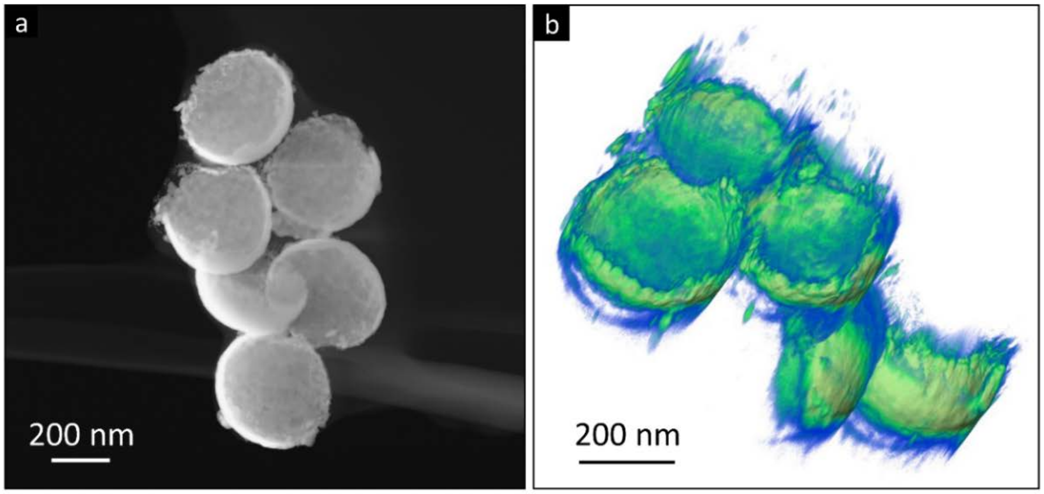

Figure 5.4 (a) Scanning TEM image of Au@PtNP NBs and (b) a corresponding STEM tomography reconstruction of the Au@PtNP NBs.

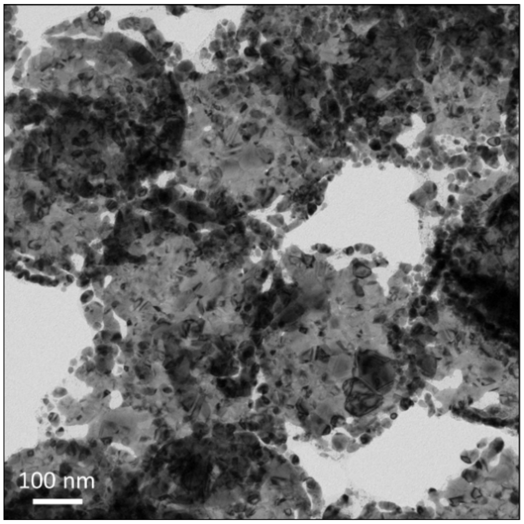

Figure 5.5 Transmission electron microscopy image of Au@PtNP NBs prepared with a Au shell of about 20-nm thickness. The NBs flatten onto the C/Formvar coating of the TEM grid upon drying, such that a bowl-like shape is not observed.

A recent report by Sung et al. found that a macroporous electrocatalyst out-performed traditional catalysts (Pt NPs supported on carbon particles) as an oxygen reduction reaction catalyst at a fuel cell cathode.(O.-H. Kim, et al., 2013) This report emphasized the importance of electrocatalyst morphology in the performance of Pt electrocatalysts. To study the morphology of the NBs as they would be employed for electrocatalytic applications, dispersions of the NBs were prepared in alcohol and drop cast onto a flat surface. The resulting material was imaged by SEM to view its morphology. A representative SEM image is shown in Fig. 5.6 of TiO_2@PtNP NBs cast into a film on a polished glassy carbon surface. The bowl-like shape is maintained after casting onto the flat surface. In addition, the NBs tend to remain in contact after removal of the PS sphere template, forming sheets of the NBs. This formation of sheets is also seen with Au@PtNP NBs; connectivity of the Au@PtNP NPs can been seen in the STEM tomography image in Fig. 5.5. The shape and connectivity of the NBs is very stable; the morphology of the NBs and NB sheets persists even after sonication for ~6 h and (for TiO_2 containing NBs) annealing at 450°C for 2 h. The bowl-like shape and connectivity of the NBs into sheets enable the TiO_2@PtNP NB film to have a large amount of free space throughout the dispersion. The NB sheets act to create macroporous tunnels throughout the film with widths between 500 and 1800-nm. The bowl-like shape of the NBs also provides space between stacks of the NB sheets that is approximately equal to the NB depth [e.g., radius of the PS sphere template (~210-nm)] (Fig. 5.6). Ordered macroporous morphologies with similar pore sizes (diameter of ~450-nm) have previously been demonstrated to enhance Pt electrocatalytic activity, such as in the previous chapter for Au@PtNP-OP electrodes and by Sung et al. for ordered macroporous Pt.(O.-H. Kim, et al., 2013) It is, therefore, anticipated that this disordered macroporous morphology could exhibit similar morphological advantages.

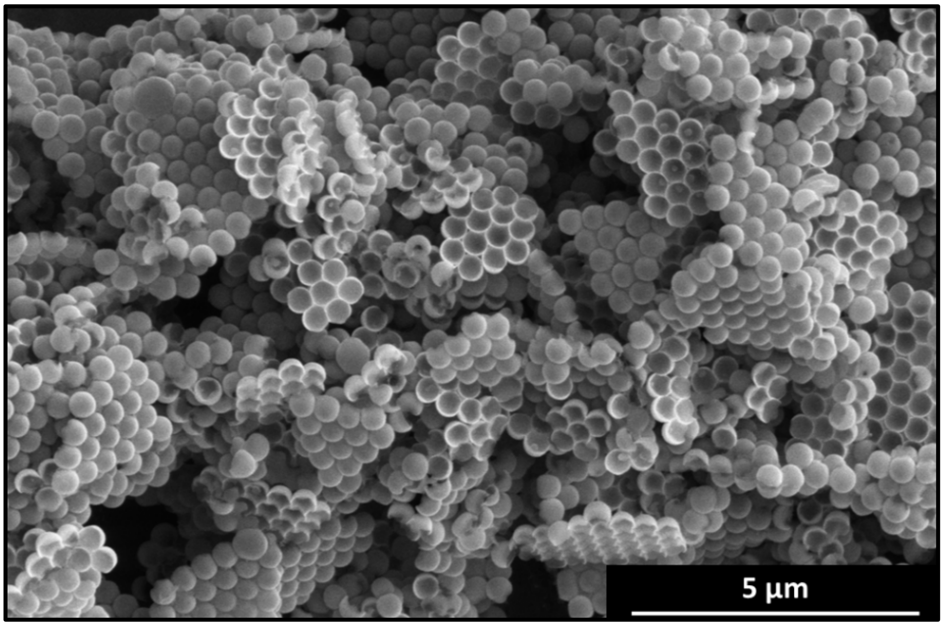

Figure 5.6 Scanning electron microscope image of a film of TiO_2@PtNP NBs prepared by drop casting of an alcohol dispersion onto a polished glassy carbon surface.

5.5. Conclusions

Support@PtNP NBs have been prepared with Au, TiO_2 and Au/TiO_2 supports. These support materials have been chosen to address issues with Pt electrocatalytic activity, such as the electrochemical stability of Pt NPs. The NB materials were characterized by EDS and XRD to confirm composition, phase and morphology of the materials. The thickness of the support shell was optimized to minimize thickness while ensuring the formation of a bowl-like shape. This bowl-like shape of the NBs was verified by STEM tomography (Au@PtNP NBs) and SEM imaging of a NB film (TiO_2@PtNP NBs). Much of the NBs tend to remain in contact after removal of the PS sphere template, forming NB sheets. The NBs and their connectivity into NB sheets are stable to sonication and annealing. Films of the NBs, prepared by drop casting of an alcohol dispersion of the NBs, had a macroporous morphology. Sheets of the NBs formed tunnels with widths between 500 and 1800-nm. The NB shape provided space between these sheets approximately equal to the NB depth (~210-nm). Overall, the tunable properties (e.g., support interactions) and open porous morphology of these NB materials could be of great interest for improving the electrocatalytic performance of Pt NPs for fuel cell applications.

Chapter 6.

Summary and Outlook

This thesis work has described the preparation and characterization of three unique electrocatalyst architectures (Fig. 6.1): Pt-OP electrodes; Au@PtNP-OP electrodes; and support@PtNP nanobowls. These materials were prepared through the use of self-assembled sacrificial templates. The synthesis of NP decorated PS spheres (PS@NPs) as sacrificial templates for the preparation of support@PtNP materials was demonstrated with tunable NP surface coverage (by ~1 order of magnitude for 200-nm diameter PS spheres) and tunable NP parking area (from 30 to 92 nm^2) with a variety of NP compositions. This method improved on previous methods for the preparation of PS@NPs, which had shown limited success in preparing PS@NPs from NPs of a diverse range of compositions, and in controlling the uniformity and loading of the NPs over the surfaces of the support.(Chia-Wei, Tseng, Shu-Fen, Yeu-Kuang, & Chung-Kwei, 2012; Dokoutchaev et al., 1999; A. G. Dong et al., 2002; Johnston, 2012; D.-W. Kim, Lee, Oh, Kim, & Oh, 2006; J.-H. Lee, Mahmoud, Sitterle, Sitterle, & Meredith, 2009; J.-M. Lee, Jun, Kim, Lee, & Oh, 2009; K. Lee, Kim, & Kim, 2010; Yunxing Li et al., 2012; Yunxing Li et al., 2011; Yimin Li & Somorjai, 2010; Yoon, Choi, & Cho, 2013; Jianan Zhang et al., 2011; M. Zhang et al., 2013) A method for assembling these PS@NPs into ordered arrays of varying thickness was also developed and optimized, based on modification of a previous report by Jeong et al.(Moon, et al., 2011) Ordered arrays of bare PS spheres and Pt PS@ NPs were essential to the formation of Pt-OP and Au@PtNP-OP electrodes, respectively. The methods developed here for the preparation of high-quality sacrificial templates provided fine control over the morphology of the electrocatalyst materials, including: i) electrode thickness; ii) macropore size; and iii) NP properties (e.g., dimensions, surface coverage and composition).

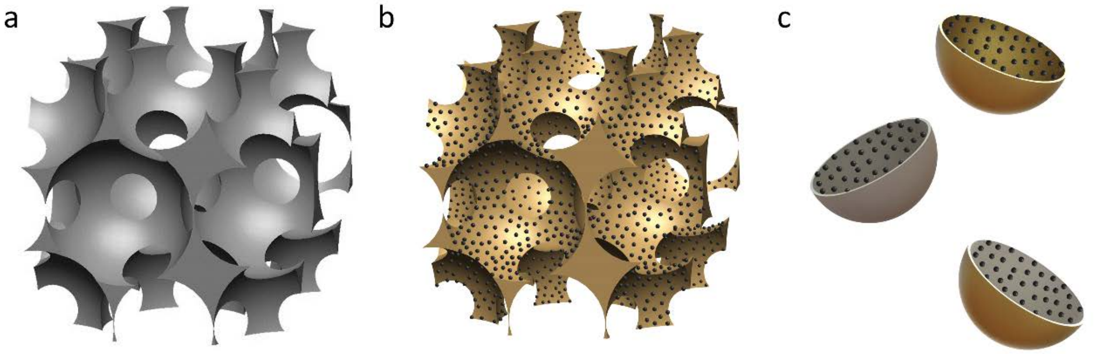

Figure 6.1 Schematic depicting the materials prepared and studied in this thesis work: (a) Pt-OP electrodes; (b) Au@PtNP-OP electrodes; (c) support@PtNP nanobowls (top - Au@PtNP NB, middle - TiO_2@PtNP NB, bottom - Au/TiO_2@PtNP NB).

The study of Pt-OP electrodes aimed to evaluate the electrochemical and material properties of Pt-OP electrodes as a platform for further application, such as in a fuel cell or as a model electrode for comparison to theoretical work. This work provided details on the connectivity of the porous network, Pt specific surface area, Pt roughness factor, and stability of the Pt-OP electrodes through the preparation and study of Pt-OP electrodes with varying thickness (and porosity). This analysis revealed that the morphology of the OP-Pt electrodes enabled access of the electrolyte throughout the OP network. The specific surface area of the Pt-OP electrodes was found to be comparable to the 3M NSTF ultrathin catalyst layer design.(Mark K. Debe, 2012) Comparison of the measured $\boldsymbol{A}_{\text{ecsa,Pt}}$ to the anticipated real surface area of the electrodes ($\boldsymbol{A}_{\text{pore-geom}}$) revealed that micro- and nano- roughness of the Pt surfaces within the Pt-OP electrodes contributes significantly to the measured $\boldsymbol{A}_{\text{ecsa}}$ with the inside of the spherical pores being smooth relative to the top surfaces of the electrodeposited Pt. The stability of the Pt-OP electrodes was assessed by electrochemical cycling from 0.05 to 1.25 V for >3 hours. After 250 cycles, the appearance by SEM, grain size and $\boldsymbol{A}_{\text{ecsa,Pt}}$ mostly stabilized. A total loss of nearly 40% of $\boldsymbol{A}_{\text{ecsa,Pt}}$ was observed during this test though, indicating some stability issues. Shortly after our report on Pt-OP electrodes was published, Sung et al. reported on the use of a very similar architecture in a PEM FC. The work by Sung et al. found that the Pt-OP electrocatalyst architecture could out-perform traditional catalyst inks in a fuel cell due to the enhanced mass transport properties provided by the macroporous morphology.(O.-H. Kim, et al., 2013) This report though, did not evaluate the stability of the Pt-OP architecture in the fuel cell. Further work on Pt-OP electrocatalysts could include:

- the use of a sacrificial template with higher surface roughness (as to increase the surface area enhancement factor)
- *in situ* fuel cell testing ofof Pt-OP electrodes with
  - varying macropore dimensions
  - varying electrode thickness (e.g., number of pore layers) to elucidate
  - hierarchial macroporous deisgn (varying macropore dimensions)

These studies could provide valuable insight into optimal design parameters (e.g., thickness and porosity) for more effective utilization of Pt within fuel cell catalyst layers.

The preparation of support@PtNP-OP electrodes was sought to build upon the Pt-OP electrode architecture, through improvements to Pt stability and Pt specific surface area. This work focused on Au@PtNP-OP electrodes, due to previous reports that had outlined several beneficial effects of Au supports for enhancing the electrocatalytic performance of Pt NPs.(Awad, et al., 2007; El- Deab & Ohsaka, 2002; Jia, et al., 2008; Kumar & Zou, 2007; Pedersen, et al., 1999; M. Shao, et al., 2010; J. Zhang, et al., 2007; Zhao & Xu, 2006) The preparation of Au@PtNP-OP electrodes with uniform Pt NP size and distribution was demonstrated through the use of Pt NP coated PS sphere templates (PS@NPs) and verified by EM, XPS and CV analysis. This method for demonstrating NP decorated ordered porous materials (also known as 3DOM or inverse opal materials), through the use of PS@NPs, was shown here for the first time. The Pt specific surface area of the Au@PtNP-OP electrodes was determined to be 27 ± 4 m^2 per g_{Pt}, representing an ~40 % improvement over the Pt-OP design.(O.-H. Kim, et al., 2013) The Au support in the Au@PtNP-OP electrodes was shown to enhance the stability of Pt NPs during electrochemical cycling and improved MeOH tolerance of Pt, an important consideration for application in DMFCs. In addition, the Au@PtNP-OP electrodes exhibited enhanced ORR activity at high overpotentials (up to 6x greater than for a commercial C/Pt catalyst ink electrode). This enhanced activity is attributed to the morphological advantages of the new architecture, similar to the morphological advantage of a porous architecture reported by Sung et al.(O.-H. Kim, et al., 2013) Further work on the support@PtNP-OP architecture could include:

- *in situ* fuel cell testing of the Au@PtNP-OP materials
- preparation and evaluation of support@PtNP-OP electrodes with different support materials (see below for material ideas)
- preparation and evaluation of support@PtNP-OP electrodes with different NP compositions (e.g., Pt alloys, as discussed in Ch. 1)

This work would assist in evaluating the benefits of this morphology regarding mass transport effects, while varying of the support and NP composition could enhance performance, lower cost and further increase Pt utilization.

The final work described in this thesis is the preparation of support@PtNP NBs designed for electrocatalytic applications. This is the first reported demonstration of a support@PtNP NB architecture for electrocatalytic applications and the first preparation of NB or half-shell materials with controlled NP distribution and size (via the use of a PS@NPs template). The NBs were prepared with a variety of support materials including TiO_2, Au, and Au/TiO_2. These materials (TiO_2@PtNP, Au@PtNP and Au/TiO_2@PtNP NBs) demonstrate the versatility of this method in preparing materials with the aim of enhancing Pt NP electrocatalytic activity through support interactions. The NBs were shown to exist primarily in sheets or arrays of NBs, that were highly stable (e.g., to extensive sonication). Films of the NBs prepared on flat supports demonstrated a macroporous morphology, with the sheets forming tunnels through the NB dispersion and the bowl-like shape of the NB providing space between the NB sheets. These NBs represent a simplified route (in comparison to support@PtNP OP electrodes) to macroporous support@NP electrodes with fine control over NP and support properties (e.g., dimensions, composition, NP surface coverage). Future work on the support@PtNP NBs will include their electrochemical characterization and their application in a fuel cell.

I believe that this work has demonstrated the preparation and characterization of new Pt-based materials that could be of great value to electrocatalysis. Future work on the OP and NB materials could explore their preparation with different support materials. Materials of interest include metal oxides, metal nitrides and metal carbides. These supports can boast a range of beneficial properties for PEM fuel cell catalysts, including activity towards ORR, improved stability (in comparison to C supports), low cost (in comparison to metal supports) and enhanced CO tolerance, among others.(Y.-J. Wang, et al., 2011) For example, tungsten oxides have been shown to improve CO tolerance and electrochemical stability of supported Pt catalysts (in comparison to C supports). The formation of hydrates on the oxide surface also enables tungsten oxides to conduct protons,(Y. M. Li, Hibino, Miyayania, & Kudo, 2000) which could be a valuable property for ionomer-free catalyst layers. Incorporation of tungsten oxide into the support@PtNP-OP architecture could be readily achieved through a similar method to that recently reported by Djaoued et al. (with the use of Pt PS@NPs instead of bare template spheres),(H. Li et al., 2014) while well-developed methods for PVD of tungsten oxides would enable their incorporation into support@PtNP NBs.(Y. B. Li, Bando, Golberg, & Kurashima, 2003) Tungsten carbides are also of interest, for their stability and Pt-like behaviour that can improve Pt catalytic activity through synergistic effects.(Ganesan, Ham, & Lee, 2007; Jeon, Daimon, Lee, Nakahara, & Woo, 2007; N. Liu, Kourtakis, Figueroa, & Chen, 2003; Zellner & Chen, 2005) Physical vapor deposition of tungsten carbide is also well-developed,(Zellner & Chen, 2005) enabling it's ready incorporation into a support@PtNP NB design. These examples demonstrate the potential utility of the developed methods in preparing Pt electrocatalysts with a variety of support materials. The ability to create these materials (OP electrodes or NBs) with a variety of support compositions, while maintaining electrocatalyst architecture is unique. Preparation of the NB or OP materials with a variety of support materials can enable more comparable study of the effect of different supports on catalytic activity, whereby the only variable changing between experiments is support composition (e.g., Pt NP properties and overall catalyst morphology remain constant), for a better understanding of catalyst-support interactions. The NP composition could also be varied for use of the OP or NB architectures for other electrocatalytic reactions. For example, Pd NPs show high activity for formic acid oxidation.(Capon & Parsons, 1973; Larsen, Ha, Zakzeski, & Masel, 2006; Zhou et al., 2006) In addition, the materials developed here could be explored for use in other applications, such as photocatalysis (e.g., TiO_2@PtNP NBs).(Lu, et al., 2013) Overall, further study of the electrocatalytic OP and NB materials in applications such as PEM FCs and in fundamental study of electrocatalysis (e.g., effects of support interactions, macropore size, or electrode thickness on catalytic performance) could confirm the morphological advantages of the new electrocatalyst architectures and provide important insights into the effects of morphology and catalyst support interactions on Pt catalyst layer activity.

References

Aiken Iii, J. D., & Finke, R. G. (1999). A Review of Modern Transition-Metal Nanoclusters: Their Synthesis, Characterization, and Applications in Catalysis. *Journal of Molecular Catalysis A: Chemical, 145*(1–2), 1-44. doi: 10.1016/S1381-1169(99)00098-9

Angerstein-Kozlowska, H. (1984). Surfaces, Cells and Solutions for Kinetic Studies. In E. Yeager (Ed.), *Comprehensive Treatise of Electrochemistry* (Vol. 9). NY: Plenum Press.

Angerstein-Kozlowska, H., Conway, B. E., & Sharp, W. B. A. (1973). The Real Condition of Electrochemically Oxidized Platinum Surfaces: Part I. Resolution of Component Processes. *Journal of Electroanalytical Chemistry and Interfacial Electrochemistry, 43*(1), 9-36. doi: 10.1016/S0022-0728(73)80307-9

Antolini, E., Lopes, T., & Gonzalez, E. R. (2008). An Overview of Platinum-Based Catalysts as Methanol-Resistant Oxygen Reduction Materials for Direct Methanol Fuel Cells. *Journal of Alloys and Compounds, 461*(1-2), 253-262. doi: 10.1016/j.jallcom.2007.06.077

Attard, G. S., Goltner, C. G., Corker, J. M., Henke, S., & Templer, R. H. (1997). Liquid-Crystal Templates for Nanostructured Metals. *Angewandte Chemie-International Edition in English, 36*(12), 1315-1317. doi: 10.1002/anie.199713151

Awad, M. I., El-Deab, M. S., & Ohsaka, T. (2007). Tailor-Designed Platinum Nanoparticles Electrodeposited onto Gold Electrode: Catalytic Activity for Oxygen Reduction. *Journal of The Electrochemical Society, 154*(8), B810-B816. doi: 10.1149/1.2744138

Bae, W. K., Char, K., Hur, H., & Lee, S. (2008). Single-Step Synthesis of Quantum Dots with Chemical Composition Gradients. *Chemistry of Materials, 20*(2), 531-539. doi: 10.1021/cm070754d

Bagotsky, V. S. (2008). Electrocatalysis *Fuel Cells* (pp. 207-230): John Wiley & Sons, Inc.

Bai, Y., Yang, W. W., Sun, Y., & Sun, C. Q. (2008). Enzyme-Free Glucose Sensor Based on a Three-Dimensional Gold Film Electrode. *Sensors and Actuators B, 134*(2), 471-476. doi: 10.1016/j.snb.2008.05.028

Bard, A. J., & Faulkner, L. R. (Eds.). (2000). *Electrochemical methods: fundamentals and applications* (2nd ed.). Hoboken, NJ: John Wiley and Sons, Inc.

Bartlett, P. N., Baumberg, J. J., Birkin, P. R., Ghanem, M. A., & Netti, M. C. (2002). Highly Ordered Macroporous Gold and Platinum Films Formed by Electrochemical Deposition through Templates Assembled from Submicron Diameter Monodisperse Polystyrene Spheres. *Chemistry of Materials, 14*(5), 2199-2208. doi: 10.1021/cm011272j

Bartlett, P. N., Birkin, P. R., & Ghanem, M. A. (2000). Electrochemical Deposition of Macroporous Platinum, Palladium and Cobalt Films using Polystyrene Latex Sphere Templates. *Chem. Commun.* , 1671-1672. doi: 10.1039/b004398m

Bastl, Z., & Pick, Š. (2004). Angle Resolved X-ray Photoelectron Spectroscopy Study of Au Deposited on Pt and Re Surfaces. *Surface Science, 566–568, Part 2*, 832-836. doi: 10.1016/j.susc.2004.06.017

Bell, A. T. (2003). The Impact of Nanoscience on Heterogeneous Catalysis. *Science, 299*(5613), 1688-1691. doi: 10.1126/science.1083671

Bonakdarpour, A., Fleischauer, M. D., Brett, M. J., & Dahn, J. R. (2008). Columnar Support Structures for Oxygen Reduction Electrocatalysts Prepared by Glancing Angle Deposition. *Appl. Catal. A-Gen., 349*(1-2), 110-115. doi: 10.1016/j.apcata.2008.07.015

Borodko, Y., Habas, S. E., Koebel, M., Yang, P., Frei, H., & Somorjai, G. A. (2006). Probing the Interaction of Poly(vinylpyrrolidone) with Platinum Nanocrystals by UV−Raman and FTIR. *The Journal of Physical Chemistry B, 110*(46), 23052-23059. doi: 10.1021/jp063338+

Cao, Y.-C., Wang, Z., Jin, X., Hua, X.-F., Liu, M.-X., & Zhao, Y.-D. (2009). Preparation of Au Nanoparticles-Coated Polystyrene Beads and its Application in Protein Immobilization. *Colloids and Surfaces A: Physicochemical and Engineering Aspects, 334*(1–3), 53-58. doi: 10.1016/j.colsurfa.2008.10.002

Capon, A., & Parsons, R. (1973). Oxidation of formic acid on noble metal electrodes. II. Comparison of the behavior of pure electrodes. [10.1016/S0022-0728(73)80250-5]. *J. Electroanal. Chem. Interfacial Electrochem., 44*(Copyright (C) 2014 American Chemical Society (ACS). All Rights Reserved.), 239-254. doi: 10.1016/s0022-0728(73)80250-5

Chan, K. R., & Eikerling, M. (2014). Water Balance Model for Polymer Electrolyte Fuel Cells with Ultrathin Catalyst Layers. [Article]. *Physical Chemistry Chemical Physics, 16*(5), 2106-2117. doi: 10.1039/c3cp54849j

Chave, T., Grunenwald, A., Ayral, A., Lacroix-Desmazes, P., & Nikitenko, S. I. (2013). Sonochemical Deposition of Platinum Nanoparticles on Polymer Beads and their

Transfer on the Pore Surface of a Silica Matrix. *Journal of Colloid and Interface Science, 395*, 81-84. doi: 10.1016/j.jcis.2012.12.029

Chen, C.-W., Serizawa, T., & Akashi, M. (2002). In Situ Formation of Au/Pt Bimetallic Colloids on Polystyrene Microspheres: Control of Particle Growth and Morphology. *Chemistry of Materials, 14*(5), 2232-2239. doi: 10.1021/cm011634n

Chen, C., Li, Y., & Liu, S. (2009). Fabrication of Macroporous Platinum using Monodisperse Silica Nanoparticle Template and its Application in Methanol Catalytic Oxidation. *J. Electroanal. Chem., 632*, 14-19. doi: 10.1016/j.jelechem.2009.03.009

Chen, D., Tao, Q., Liao, L. W., Liu, S. X., Chen, Y. X., & Ye, S. (2011). Determining the Active Surface Area for Various Platinum Electrodes. *Electrocatalysis, 2*(3), 207-219. doi: 10.1007/s12678-011-0054-1

Chen, J. I. L., Loso, E., Ebrahim, N., & Ozin, G. A. (2008). Synergy of Slow Photon and Chemically Amplified Photochemistry in Platinum Nanocluster-Loaded Inverse Titania Opals. *Journal of the American Chemical Society, 130*(16), 5420-5421. doi: 10.1021/ja800288f

Cherevko, S., Topalov, A. A., Zeradjanin, A. R., Katsounaros, I., & Mayrhofer, K. J. J. (2013). Gold Dissolution: Towards Understanding of Noble Metal Corrosion. *RSC Advances, 3*(37), 16516-16527. doi: 10.1039/c3ra42684j

Cheung, C. L., Nikolić, R. J., Reinhardt, C. E., & Wang, T. F. (2006). Fabrication of Nanopillars by Nanosphere Lithography. *Nanotechnology, 17*(5), 1339.

Chia-Wei, W., Tseng, S. J., Shu-Fen, P., Yeu-Kuang, H., & Chung-Kwei, L. (2012). Functionalized Polymer Spheres via One-Step Photoinduced Synthesis for Antimicrobial Activity and Gene Delivery. *Nanotechnology, 23*(25), 255103. doi: 10.1088/0957-4484/23/25/255103

Chlistunoff, J., Wilson, M., & Garzón, F. (2011). Electrochemical Studies of Novel Pt/Ceria/C Oxygen Reduction Catalysts for Fuel Cells. *ECS Transactions, 41*(1), 2341-2348. doi: 10.1149/1.3635768

Cho, Y.-B., Kim, J. E., Shim, J. H., Lee, C., & Lee, Y. (2013). Synthesis and Electrocatalytic Activity of Highly Porous Hollow Palladium Nanoshells for Oxygen Reduction in Alkaline Solution. [10.1039/C3CP50661D]. *Physical Chemistry Chemical Physics, 15*(27), 11461-11467. doi: 10.1039/c3cp50661d

Choi, S. M., Kim, J. H., Jung, J. Y., Yoon, E. Y., & Kim, W. B. (2008). Pt Nanowires Prepared via a Polymer Template Method: Its Promise Toward High Pt-Loaded Electrocatalysts for Methanol Oxidation. *Electrochim. Acta, 53*, 5804-5811. doi: 10.1016/j.electacta.2008.03.041

Conway, B. E., Angerstein-Kozlowska, H., Sharp, W. B. A., & Criddle, E. E. (1973). Ultrapurification of Water for Electrochemical and Surface Chemical Work by Catalytic Pyrodistillation. *Analytical Chemistry, 45*(8), 1331-1336. doi: 10.1021/ac60330a025

Dam, V. A. T., & de Bruijn, F. A. (2007). The Stability of PEMFC Electrodes - Platinum Dissolution vs Potential and Temperature Investigated by Quartz Crystal Microbalance. *Journal of The Electrochemical Society, 154*(5), B494-B499. doi: 10.1149/1.2714327

Dam, V. A. T., Jayasayee, K., & de Bruijn, F. A. (2009). Determination of the Potentiostatic Stability of PEMFC Electro Catalysts at Elevated Temperatures. [Article]. *Fuel Cells, 9*(4), 453-462. doi: 10.1002/fuce.200800136

David, T. (2002). Catalysts for the Proton Exchange Membrane Fuel Cell *Fuel Cell Technology Handbook*: CRC Press.

de Bruijn, F. A., Dam, V. A. T., & Janssen, G. J. M. (2008). Durability and Degradation Issues of PEM Fuel Cell Components. [Review]. *Fuel Cells, 8*(1), 3-22. doi: 10.1002/fuce.200700053

Debe, M. K. (2012). Electrocatalyst Approaches and Challenges for Automotive Fuel Cells. *Nature, 486*, 43-51. doi: 10.1038/nature11115

Debe, M. K. (2012). Nanostructured Thin Film Electrocatalysts for PEM Fuel Cells - A Tutorial on the Fundamental Characteristics and Practical Properties of NSTF Catalysts. *ECS Trans., 45*, 47-68. doi: 10.1149/1.3701968

Dokoutchaev, A., James, J. T., Koene, S. C., Pathak, S., Prakash, G. K. S., & Thompson, M. E. (1999). Colloidal Metal Deposition on Functionalized Polystyrene Spheres. *Chem. Mater., 11*(9). doi: 10.1021/cm9900352

Dong, A., Chen, J., Oh, S. J., Koh, W.-k., Xiu, F., Ye, X., . . . Murray, C. B. (2011). Multiscale Periodic Assembly of Striped Nanocrystal Superlattice Films on a Liquid Surface. *Nano Letters, 11*(2), 841-846. doi: 10.1021/nl104208x

Dong, A. G., Wang, Y. J., Tang, Y., Ren, N., Yang, W. L., & Gao, Z. (2002). Fabrication of Compact Silver Nanoshells on Polystyrene Spheres Through Electrostatic Attraction. *Chemical Communications*(4), 350-351. doi: 10.1039/b110164c

Du, Y., Lv, K., Su, B., Zhang, N., & Wang, C. (2009). Electro-Reduction of Oxygen and Electro-Oxidation of Methanol at Pd Monolayer-Modified Macroporous Pt Electrode. *J. Appl. Electrochem., 39*, 2409-2414. doi: 10.1007/s10800-009-9928-9

Egerton, R. (2005). *Physical Principles of Electron Microscopy: An Introduction to TEM, SEM, and AEM*: Springer US.

El- Deab, M. S., & Ohsaka, T. (2002). An Extraordinary Electrocatalytic Reduction of Oxygen on Gold Nanoparticles-Electrodeposited Gold Electrodes. *Electrochemistry Communications, 4*(4), 288-292. doi: 10.1016/S1388-2481(02)00263-1

Friedrich, K. A., Henglein, F., Stimming, U., & Unkauf, W. (2000). Size Dependence of the CO Monolayer Oxidation on Nanosized Pt Particles Supported on Gold. *Electrochimica Acta, 45*(20), 3283-3293. doi: 10.1016/S0013-4686(00)00430-8

Ganesan, R., Ham, D. J., & Lee, J. S. (2007). Platinized Mesoporous Tungsten Carbide for Electrochemical Methanol Oxidation. *Electrochemistry Communications, 9*(10), 2576-2579. doi: http://dx.doi.org/10.1016/j.elecom.2007.08.002

Gasteiger, H. A., Kocha, S. S., Sompalli, B., & Wagner, F. T. (2005). Activity Benchmarks and Requirements for Pt, Pt-alloy, and Non-Pt Oxygen Reduction Catalysts for PEMFCs. *Applied Catalysis B: Environmental, 56*(1–2), 9-35. doi: 10.1016/j.apcatb.2004.06.021

Gates, B., Yin, Y., & Xia, Y. (1999). Fabrication and Characterization of Porous Membranes with Highly Ordered Three-Dimensional Periodic Structures. *Chem. Mater., 11*, 9. doi: 10.1021/cm990195d

Ge, X., Yan, X., Wang, R., Tian, F., & Ding, Y. (2009). Tailoring the Structure and Property of Pt-Decorated Nanoporous Gold by Thermal Annealing. *The Journal of Physical Chemistry C, 113*(17), 7379-7384. doi: 10.1021/jp9008702

Giorgi, R., Giorgi, L., Gagliardi, S., Salernitano, E., Alvisi, M., Dikonimos, T., . . . Serra, E. (2011). Nanomaterials-Based PEM Electrodes by Combining Chemical and Physical Depositions. *J. Fuel Cell Sci. Technol., 8*(4). doi: 10.1115/1.4003629

Gottesfeld, S., & Zawodzinski, T. A. (2008). Polymer Electrolyte Fuel Cells *Advances in Electrochemical Science and Engineering* (pp. 195-301): Wiley-VCH Verlag GmbH.

Greeley, J., Stephens, I. E. L., Bondarenko, A. S., Johansson, T. P., Hansen, H. A., Jaramillo, T. F., . . . Nørskov, J. K. (2009). Alloys of Platinum and Early Transition Metals as Oxygen Reduction Electrocatalysts. *Nature Chemistry, 1*(7), 552-556. doi: 10.1038/nchem.367

Gregor, H. (2002). Introduction *Fuel Cell Technology Handbook*: CRC Press.

Gu, X., Cong, X., & Ding, Y. (2010). Platinum-Decorated Au Porous Nanotubes as Highly Efficient Catalysts for Formic Acid Electro-Oxidation. *ChemPhysChem, 11*(4), 841-846. doi: 10.1002/cphc.200900927

Guan, G., Zapf, R., Kolb, G., Men, Y., Hessel, V., Loewe, H., . . . Zentel, R. (2007). Low Temperature Catalytic Combustion of Propane over Pt-Based Catalyst with

Inverse Opal Microstructure in a Microchannel Reactor. *Chemical Communications*(3), 260-262. doi: 10.1039/b609599b

Guizard, C., & Princivalle, A. (2009). Preparation and Characterization of Catalyst Thin Films. *Catalysis Today, 146*(3-4), 367-377. doi: 10.1016/j.cattod.2009.05.012

Guo, I. W., Pekcevik, I. C., Wang, M. C. P., Pilapil, B. K., & Gates, B. D. (2014). Colloidal Core-Shell Materials with 'Spiky' Surfaces Assembled from Gold Nanorods. *Chemical Communications, 50*(60), 8157-8160. doi: 10.1039/c4cc02410a

Guo, S., Fang, Y., Dong, S., & Wang, E. (2007). High-Efficiency and Low-Cost Hybrid Nanomaterial as Enhancing Electrocatalyst: Spongelike Au/Pt Core/Shell Nanomaterial with Hollow Cavity. *The Journal of Physical Chemistry C, 111*(45), 17104-17109. doi: 10.1021/jp075625z

Guo, X., Guo, D.-J., Qiu, X.-P., Chen, L.-Q., & Zhu, W.-T. (2009). Excellent Dispersion and Electrocatalytic Properties of Pt Nanoparticles Supported on Novel Porous Anatase TiO_2 Nanorods. *Journal of Power Sources, 194*(1), 281-285. doi: 10.1016/j.jpowsour.2009.05.035

Gupta, S., Giordano, C., Gradzielski, M., & Mehta, S. K. (2013). Microwave-Assisted Synthesis of Small Ru Nanoparticles and Their Role in Degradation of Congo Red. *Journal of Colloid and Interface Science*. doi: 10.1016/j.jcis.2013.08.030

Hammer, B., & Nørskov, J. K. (2000). Theoretical Surface Science and Catalysis—Calculations and Concepts. In H. K. Bruce C. Gates (Ed.), *Advances in Catalysis* (Vol. 45, pp. 71-129): Academic Press.

Hammond, J. S., & Winograd, N. (1977). XPS Spectroscopic Study of Potentiostatic and Galvanostatic Oxidation of Pt Electrodes in H_2SO_4 and $HClO_4$. *Journal of Electroanalytical Chemistry and Interfacial Electrochemistry, 78*(1), 55-69. doi: 10.1016/S0022-0728(77)80422-1

Hayden, B. E., Pletcher, D., Suchsland, J. P., & Williams, L. J. (2009). The Influence of Support and Particle Size on the Platinum Catalysed Oxygen Reduction Reaction. *Physical Chemistry Chemical Physics, 11*(40), 9141-9148. doi: 10.1039/b910110a

Hernández-Fernández, P., Rojas, S., Ocón, P., de Frutos, A., Figueroa, J. M., Terreros, P., . . . Fierro, J. L. G. (2008). Relevance of the Nature of Bimetallic PtAu Nanoparticles as Electrocatalysts for the Oxygen Reduction Reaction in the Presence of Methanol. *Journal of Power Sources, 177*(1), 9-16. doi: 10.1016/j.jpowsour.2007.11.020

Holzwarth, U., & Gibson, N. (2011). The Scherrer Equation Versus the 'Debye-Scherrer Equation'. *Nature Nanotechnology, 6*(9), 534-534. doi: 10.1038/nnano.2011.145

Huang, S.-Y., Ganesan, P., & Popov, B. N. (2011). Titania Supported Platinum Catalyst with High Electrocatalytic Activity and Stability for Polymer Electrolyte Membrane Fuel Cell. *Applied Catalysis B: Environmental, 102*(1–2), 71-77. doi: 10.1016/j.apcatb.2010.11.026

Huang, S.-Y., Ganesan, P., & Popov, B. N. (2012). Electrocatalytic Activity and Stability of Titania-Supported Platinum–Palladium Electrocatalysts for Polymer Electrolyte Membrane Fuel Cell. *ACS Catalysis, 2*(5), 825-831. doi: 10.1021/cs300088n

Huang, Y.-J., Lai, C.-H., Wu, P.-W., & Chen, L.-Y. (2010). Ni Inverse Opals for Water Electrolysis in an Alkaline Electrolyte. *J. Electrochem. Soc., 157*, P18-P22. doi: 10.1149/1.3281332

Jackson, S. D., Willis, J., McLellan, G. D., Webb, G., Keegan, M. B. T., Moyes, R. B., . . . Whyman, R. (1993). Supported Metal Catalysts: Preparation, Characterization, and Function: I. Preparation and Physical Characterization of Platinum Catalysts. *Journal of Catalysis, 139*(1), 191-206. doi: 10.1006/jcat.1993.1017

Jeon, M. K., Daimon, H., Lee, K. R., Nakahara, A., & Woo, S. I. (2007). CO Tolerant Pt/WC Methanol Electro-Oxidation Catalyst. *Electrochemistry Communications, 9*(11), 2692-2695. doi: 10.1016/j.elecom.2007.09.001

Jeong, S.-M., Kim, M. K., Kim, G.-P., Kim, T. Y., & Baeck, S.-H. (2012). Preparation of Pt–Au/Carbon Catalysts by a Reduction Method and their Electrocatalytic Activities for Oxygen Reduction Reactions. *Chemical Engineering Journal, 198–199*(0), 435-439. doi: 10.1016/j.cej.2012.04.002

Jerkiewicz, G. (2010). Electrochemical Hydrogen Adsorption and Absorption. Part 1: Under-potential Deposition of Hydrogen. *Electrocatalysis, 1*(4), 179-199. doi: 10.1007/s12678-010-0022-1

Jerkiewicz, G., Vatankhah, G., Lessard, J., Soriaga, M. P., & Park, Y.-S. (2004). Surface-Oxide Growth at Platinum Electrodes in Aqueous H_2SO_4: Reexamination of Its Mechanism Through Combined Cyclic-Voltammetry, Electrochemical Quartz-Crystal Nanobalance, and Auger Electron Spectroscopy Measurements. *Electrochimica Acta, 49*(9–10), 1451-1459. doi: 10.1016/j.electacta.2003.11.008

Ji, M., & Wei, Z. (2009). A Review of Water Management in Polymer Electrolyte Membrane Fuel Cells. *Energies, 2*(4), 1057-1106.

Jia, J., Cao, L., & Wang, Z. (2008). Platinum-Coated Gold Nanoporous Film Surface: Electrodeposition and Enhanced Electrocatalytic Activity for Methanol Oxidation. *Langmuir, 24*(11), 5932-5936. doi: 10.1021/la800163f

Johnson, N. J. J., Sangeetha, N. M., Boyer, J.-C., & van Veggel, F. C. J. M. (2010). Facile Ligand-Exchange with Polyvinylpyrrolidone and Subsequent Silica Coating of Hydrophobic Upconverting beta-Na_YF_4:Yb^{3+}/Er^{3+} Nanoparticles. *Nanoscale, 2*(5), 771-777.

Johnston, R. L. (2012). Chapter 1 - Metal Nanoparticles and Nanoalloys. In L. J. Roy & J. P. Wilcoxon (Eds.), *Frontiers of Nanoscience* (Vol. Volume 3, pp. 1-42): Elsevier.

Juodkazis, K., Juodkazyt, J., Jasulaitien, V., Lukinskas, A., & Šebeka, B. (2000). XPS Studies on the Gold Oxide Surface Layer Formation. *Electrochemistry Communications, 2*(7), 503-507. doi: 10.1016/S1388-2481(00)00069-2

Justin, C. L., & Andreas, S. (2006). Recent Progress in Synthesis and Applications of Inverse Opals and Related Macroporous Materials Prepared by Colloidal Crystal Templating *Annual Review of Nano Research* (Vol. Volume 1, pp. 1-79): World Scientific.

Kalsin, A. M., Pinchuk, A. O., Smoukov, S. K., Paszewski, M., Schatz, G. C., & Grzybowski, B. A. (2006). Electrostatic Aggregation and Formation of Core−Shell Suprastructures in Binary Mixtures of Charged Metal Nanoparticles. *Nano Letters, 6*(9), 1896-1903. doi: 10.1021/nl060967m

Kim, D.-W., Lee, J.-M., Oh, C., Kim, D.-S., & Oh, S.-G. (2006). A Novel Preparation Route for Platinum–Polystyrene Heterogeneous Nanocomposite Particles Using Alcohol-Reduction Method. *Journal of Colloid and Interface Science, 297*(1), 365-369. doi: 10.1016/j.jcis.2005.09.067

Kim, O.-H., Cho, Y.-H., Kang, S. H., Park, H.-Y., Kim, M., Lim, J. W., . . . Sung, Y.-E. (2013). Ordered Macroporous Platinum Electrode and Enhanced Mass Transfer in Fuel Cells using Inverse Opal Structure. *Nat Commun, 4*. doi: 10.1038/ncomms3473

Kinkead, B., Ali, A. A., Boyer, J.-C., & Gates, B. D. (2013). Optically Active Nanoparticle Coated Polystyrene Spheres. *MRS Online Proceedings Library, 1546*. doi: doi:10.1557/opl.2013.606

Kinkead, B., van Drunen, J., Paul, M. Y., Dowling, K., Jerkiewicz, G., & Gates, B. (2013). Platinum Ordered Porous Electrodes: Developing a Platform for Fundamental Electrochemical Characterization. *Electrocatalysis, 4*(3), 179-186. doi: 10.1007/s12678-013-0145-2

Kocha, S. S. (2012). Chapter 3 - Electrochemical Degradation: Electrocatalyst and Support Durability. In M. M. Mench, E. C. Kumbur & T. N. Veziroglu (Eds.), *Polymer Electrolyte Fuel Cell Degradation* (pp. 89-214). Boston: Academic Press.

Kongkanand, A., Dioguardi, M., Ji, C., & Thompson, E. L. (2012). Improving Operational Robustness of NSTF Electrodes in PEM Fuel Cells. *Journal of The Electrochemical Society, 159*(8), F405-F411. doi: 10.1149/2.045208jes

Kongkanand, A., Owejan, J. E., Moose, S., Dioguardi, M., Biradar, M., & Makharia, R. (2012). Development of Dispersed-Catalyst/NSTF Hybrid Electrode. *Journal of The Electrochemical Society, 159*(11), F676-F682. doi: 10.1149/2.023211jes

Kristian, N., Yu, Y., Gunawan, P., Xu, R., Deng, W., Liu, X., & Wang, X. (2009). Controlled Synthesis of Pt-decorated Au Nanostructure and its Promoted Activity Toward Formic Acid Electro-Oxidation. *Electrochimica Acta, 54*(21), 4916-4924. doi: 10.1016/j.electacta.2009.04.018

Kumar, S., & Zou, S. (2007). Electrooxidation of Carbon Monoxide and Methanol on Platinum-Overlayer-Coated Gold Nanoparticles: Effects of Film Thickness. *Langmuir, 23*(13), 7365-7371. doi: 10.1021/la0637216

Lamy, C., Coutanceau, C., & Alonso-Vante, N. (2009). Methanol-Tolerant Cathode Catalysts for DMFC *Electrocatalysis of Direct Methanol Fuel Cells* (pp. 257-314): Wiley-VCH Verlag GmbH & Co. KGaA.

Lamy, C., Lima, A., LeRhun, V., Delime, F., Coutanceau, C., & Léger, J.-M. (2002). Recent Advances in the Development of Direct Alcohol Fuel Cells (DAFC). *Journal of Power Sources, 105*(2), 283-296. doi: 10.1016/S0378-7753(01)00954-5

Lang, X., Xing-Cai, W., & Jun-Jie, Z. (2008). Green Preparation and Catalytic Application of Pd Nanoparticles. *Nanotechnology, 19*(30), 305603. doi: 10.1088/0957-4484/19/30/305603

Larsen, R., Ha, S., Zakzeski, J., & Masel, R. I. (2006). Unusually Active Palladium-Based Catalysts for the Electrooxidation of Formic Acid. *J. Power Sources, 157*, 78-84. doi: 10.1016/j.jpowsour.2005.07.066

Lavacchi, A., Miller, H., & Vizza, F. (2013a). A Bird's Eye View of Energy-Related Electrochemistry *Nanotechnology in Electrocatalysis for Energy* (Vol. 170, pp. 25-61): Springer New York.

Lavacchi, A., Miller, H., & Vizza, F. (2013b). Electrochemical Devices for Energy Conversion and Storage *Nanotechnology in Electrocatalysis for Energy* (Vol. 170, pp. 63-89): Springer New York.

Lavacchi, A., Miller, H., & Vizza, F. (2013c). Introduction *Nanotechnology in Electrocatalysis for Energy* (Vol. 170, pp. 3-23): Springer New York.

Lee, J.-H., Mahmoud, M. A., Sitterle, V., Sitterle, J., & Meredith, J. C. (2009). Facile Preparation of Highly-Scattering Metal Nanoparticle-Coated Polymer Microbeads and Their Surface Plasmon Resonance. *Journal of the American Chemical Society, 131*(14), 5048-5049. doi: 10.1021/ja900698w

Lee, J.-M., Jun, Y.-D., Kim, D.-W., Lee, Y.-H., & Oh, S.-G. (2009). Effects of PVP on the Formation of Silver–Polystyrene Heterogeneous Nanocomposite Particles in Novel Preparation Route Involving Polyol Process: Molecular Weight and Concentration of PVP. *Materials Chemistry and Physics, 114*(2–3), 549-555. doi: 10.1016/j.matchemphys.2008.10.001

Lee, K., Kim, M., & Kim, H. (2010). Catalytic Nanoparticles Being Facet-Controlled. *Journal of Materials Chemistry, 20*(19), 3791-3798. doi: 10.1039/b921857b

Lewera, A., Timperman, L., Roguska, A., & Alonso-Vante, N. (2011). Metal–Support Interactions between Nanosized Pt and Metal Oxides (WO_3 and TiO_2) Studied Using X-ray Photoelectron Spectroscopy. *The Journal of Physical Chemistry C, 115*(41), 20153-20159. doi: 10.1021/jp2068446

Li, H., Theriault, J., Rousselle, B., Subramanian, B., Robichaud, J., & Djaoued, Y. (2014). Facile Fabrication of Crack-Free Large-Area 2D WO_3 Inverse Opal Films by a 'Dynamic Hard-Template' Strategy on ITO Substrates. *Chemical Communications, 50*(17), 2184-2186. doi: 10.1039/c3cc48558g

Li, Y., Pan, Y., Yang, C., Gao, Y., Wang, Z., & Xue, G. (2012). Synthesis and Structural Control of Gold Nanoparticles-Coated Polystyrene Composite Particles Based on Colloid Thermodynamics. *Colloids and Surfaces A: Physicochemical and Engineering Aspects, 414*, 504-511. doi: 10.1016/j.colsurfa.2012.08.006

Li, Y., Pan, Y., Zhu, L., Wang, Z., Su, D., & Xue, G. (2011). Facile and Controlled Fabrication of Functional Gold Nanoparticle-Coated Polystyrene Composite Particle. *Macromolecular Rapid Communications, 32*(21), 1741-1747. doi: 10.1002/marc.201100377

Li, Y., & Somorjai, G. A. (2010). Nanoscale Advances in Catalysis and Energy Applications. *Nano Letters, 10*(7), 2289-2295. doi: 10.1021/nl101807g

Li, Y. B., Bando, Y., Golberg, D., & Kurashima, K. (2003). WO_3 Nanorods/Nanobelts Synthesized via Physical Vapor Deposition Process. *Chemical Physics Letters, 367*(1–2), 214-218. doi: 10.1016/S0009-2614(02)01702-5

Li, Y. M., Hibino, M., Miyayania, M., & Kudo, T. (2000). Proton Conductivity of Tungsten Trioxide Hydrates at Intermediate Temperature. *Solid State Ionics, 134*(3–4), 271-279. doi: 10.1016/S0167-2738(00)00759-1

Liao, S., Li, B., & Li, Y. (2008). Physical Characterization of Electrocatalysts. In J. Zhang (Ed.), *PEM Fuel Cell Electrocatalysts and Catalyst Layers* (pp. 487-546): Springer London.

Lim, D. C., Lopez-Salido, I., Dietsche, R., Bubek, M., & Kim, Y. D. (2006). Oxidation of Au Nanoparticles on HOPG Using Atomic Oxygen. *Surface Science, 600*(3), 507-513. doi: 10.1016/j.susc.2005.10.064

Liu, N., Kourtakis, K., Figueroa, J. C., & Chen, J. G. (2003). Potential Application of Tungsten Carbides as Electrocatalysts: III. Reactions of Methanol, Water, and Hydrogen on Pt-Modified C/W(111) Surfaces. *Journal of Catalysis, 215*(2), 254-263. doi: 10.1016/S0021-9517(03)00019-8

Liu, Y., Chen, J., Misoska, V., Sweigers, G. F., & Wallace, G. G. (2007). Preparation of Platinum Inverse Opals Using Self-Assembled Templates and their Application in Methanol Oxidation. *Materials Letters, 61*, 3. doi: 10.1016/j.matlet.2007.01.096

Love, J. C., Gates, B. D., Wolfe, D. B., Paul, K. E., & Whitesides, G. M. (2002). Fabrication and Wetting Properties of Metallic Half-Shells with Submicron Diameters. *Nano Letters, 2*(8), 891-894. doi: 10.1021/nl025633l

Lu, J., Zhang, P., Li, A., Su, F., Wang, T., Liu, Y., & Gong, J. (2013). Mesoporous Anatase TiO_2 Nanocups with Plasmonic Metal Decoration for Highly Active Visible-Light Photocatalysis. *Chemical Communications, 49*(52), 5817-5819. doi: 10.1039/c3cc42029a

Luo, J., Njoki, P. N., Lin, Y., Wang, L., & Zhong, C. J. (2006). Activity-Composition Correlation of AuPt Alloy Nanoparticle Catalysts in Electrocatalytic Reduction of Oxygen. *Electrochemistry Communications, 8*(4), 581-587. doi: 10.1016/j.elecom.2006.02.001

Lytle, J. C., & Stein, A. (2010). Recent Progress in Syntheses and Applications of Inverse Opals and Related Macroporous Materials Prepared by Colloidal Crystal Templating. *ChemInform, 41*(28), i.

Mahshid, S. S., Mahshid, S., Dolati, A., Ghorbani, M., Yang, L. X., Luo, S. L., & Cai, Q. Y. (2011). Template-Based Electrodeposition of Pt/Ni Nanowires and its Catalytic Activity Towards Glucose Oxidation. *Electrochimica Acta, 58*, 551-555. doi: 10.1016/j.electacta.2011.09.083

Marković, N. M., Schmidt, T. J., Stamenković, V., & Ross, P. N. (2001). Oxygen Reduction Reaction on Pt and Pt Bimetallic Surfaces: A Selective Review. *Fuel Cells, 1*(2), 105-116. doi: 10.1002/1615-6854(200107)

Mayrhofer, K. J. J., Strmcnik, D., Blizanac, B. B., Stamenkovic, V., Arenz, M., & Markovic, N. M. (2008). Measurement of Oxygen Reduction Activities via the Rotating Disc Electrode Method: From Pt Model Surfaces to Carbon-Supported High Surface Area Catalysts. *Electrochimica Acta, 53*(7), 3181-3188. doi: 10.1016/j.electacta.2007.11.057

Mine, E., & Shirai, M. (2009). Preparation of Ordered Macroporous Platinum and Palladium Powders. *J. Porous Mater., 16*, 185-190. doi: 10.1007/s10934-007-9183-6

Moon, G. D., Lee, T. I., Kim, B., Chae, G., Kim, J., Kim, S., . . . Jeong, U. (2011). Assembled Monolayers of Hydrophilic Particles on Water Surfaces. *ACS Nano, 5*(11), 12.

Moulder, J. F., Stickle, W. F., Sobol, P. E., & Bomben, K. D. (1992). *Handbook of X-ray Photoelectron Spectroscopy* (Vol. 40): Perkin Elmer Eden Prairie, MN.

Mucic, R. C., Storhoff, J. J., Mirkin, C. A., & Letsinger, R. L. (1998). DNA-Directed Synthesis of Binary Nanoparticle Network Materials. *Journal of the American Chemical Society, 120*(48), 12674-12675.

Nesselberger, M., Roefzaad, M., Hamou, R. F., Biedermann, P. U., Schweinberger, F. F., Kunz, S., . . . Heiz, U. (2013). The Effect of Particle Proximity on the Oxygen Reduction Rate of Size-Selected Platinum Clusters. *Nat Mater, 12*(10), 919-924. doi: 10.1038/nmat3712

Nie, Z., Petukhova, A., & Kumacheva, E. (2010). Properties and Emerging Applications of Self-Assembled Structures Made From Inorganic Nanoparticles. *Nat Nano, 5*(1), 15-25. doi: 10.1038/nnano.2009.453

Norris, D. J., Arlinghaus, E. G., Meng, L., Heiny, R., & Scriven, L. E. (2004). Opaline Photonic Crystals: How Does Self-Assembly Work? *Advanced Materials, 16*(16), 1393-1399. doi: 10.1002/adma.200400455

Nørskov, J. K., Rossmeisl, J., Logadottir, A., Lindqvist, L., Kitchin, J. R., Bligaard, T., & Jónsson, H. (2004). Origin of the Overpotential for Oxygen Reduction at a Fuel-Cell Cathode. *The Journal of Physical Chemistry B, 108*(46), 17886-17892. doi: 10.1021/jp047349j

Park, S., Shao, Y., Wan, H., Rieke, P. C., Viswanathan, V. V., Towne, S. A., . . . Wang, Y. (2011). Design of Graphene Sheets-Supported Pt Catalyst Layer in PEM Fuel Cells. *Electrochemistry Communications, 13*(3), 258-261. doi: 10.1016/j.elecom.2010.12.028

Paulus, U. A., Schmidt, T. J., Gasteiger, H. A., & Behm, R. J. (2001). Oxygen Reduction on a High-Surface Area Pt/Vulcan Carbon Catalyst: A Thin-Film Rotating Ring-Disk Electrode Study. *Journal of Electroanalytical Chemistry, 495*(2), 134-145. doi: 10.1016/S0022-0728(00)00407-1

Pedersen, M. Ø., Helveg, S., Ruban, A., Stensgaard, I., Lægsgaard, E., Nørskov, J. K., & Besenbacher, F. (1999). How a Gold Substrate Can Increase the Reactivity of a Pt Overlayer. *Surface Science, 426*(3), 395-409. doi: 10.1016/S0039-6028(99)00385-4

Qi, Z. (2008). Electrochemical Methods for Catalyst Activity Evaluation. In J. Zhang (Ed.), *PEM Fuel Cell Electrocatalysts and Catalyst Layers* (pp. 547-607): Springer London.

Rabis, A., Rodriguez, P., & Schmidt, T. J. (2012). Electrocatalysis for Polymer Electrolyte Fuel Cells: Recent Achievements and Future Challenges. *ACS Catalysis, 2*(5), 864-890. doi: 10.1021/cs3000864

Ralph, T. R., Hards, G. A., Keating, J. E., Campbell, S. A., Wilkinson, D. P., Davis, M., . . . Johnson, M. C. (1997). Low Cost Electrodes for Proton Exchange Membrane Fuel Cells: Performance in Single Cells and Ballard Stacks. *Journal of The Electrochemical Society, 144*(11), 3845-3857. doi: 10.1149/1.1838101

Rand, D. A. J., & Woods, R. (1972). A Study of the Dissolution of Platinum, Palladium, Rhodium and Gold Electrodes in 1 M Sulphuric Acid by Cyclic Voltammetry. *Journal of Electroanalytical Chemistry and Interfacial Electrochemistry, 35*(1), 209-218. doi: 10.1016/S0022-0728(72)80308-5

Rinaldo, S. G., Stumper, J., & Eikerling, M. (2010). Physical Theory of Platinum Nanoparticle Dissolution in Polymer Electrolyte Fuel Cells. [Article]. *Journal of Physical Chemistry C, 114*(13), 5773-5785. doi: 10.1021/jp9101509

Rouya, E., Cattarin, S., Reed, M. L., Kelly, R. G., & Zangari, G. (2012). Electrochemical Characterization of the Surface Area of Nanoporous Gold Films. *Journal of The Electrochemical Society, 159*(4), K97-K102. doi: 10.1149/2.097204jes

Sacanna, S., Pine, D. J., & Yi, G.-R. (2013). Engineering Shape: The Novel Geometries of Colloidal Self-Assembly. *Soft Matter, 9*(34), 8096-8106. doi: 10.1039/c3sm50500f

Santos, E., & Schmickler, W. (2006). d-Band Catalysis in Electrochemistry. *ChemPhysChem, 7*(11), 2282-2285. doi: 10.1002/cphc.200600441

Sasaki, K., Zhang, L., & Adzic, R. R. (2008). Niobium Oxide-Supported Platinum Ultra-Low Amount Electrocatalysts for Oxygen Reduction. *Physical Chemistry Chemical Physics, 10*(1), 159-167. doi: 10.1039/b709893f

Satyapal, S. (2012). *FY 2012 Annual Progress Report*. U.S. Department of Energy Hydrogen and Fuel Cells Program.

Sawyer, D. T., Sobkowiak, A., & Roberts, J. L. (1995). *Electrochemistry for Chemists*: Wiley.

Senthil Kumar, S., & Phani, K. L. N. (2009). Exploration of Unalloyed Bimetallic Au–Pt/C Nanoparticles for Oxygen Reduction Reaction. *Journal of Power Sources, 187*(1), 19-24. doi: 10.1016/j.jpowsour.2008.10.121

Shao, M., Odell, J. H., Choi, S.-I., & Xia, Y. (2013). Electrochemical Surface Area Measurements of Platinum- and Palladium-Based Nanoparticles. *Electrochemistry Communications, 31*(0), 46-48. doi: 10.1016/j.elecom.2013.03.011

Shao, M., Peles, A., Shoemaker, K., Gummalla, M., Njoki, P. N., Luo, J., & Zhong, C.-J. (2010). Enhanced Oxygen Reduction Activity of Platinum Monolayer on Gold Nanoparticles. *The Journal of Physical Chemistry Letters, 2*(2), 67-72. doi: 10.1021/jz1015789

Shao, Y., Yin, G., & Gao, Y. (2007). Understanding and Approaches for the Durability Issues of Pt-Based Catalysts for PEM Fuel Cell. *Journal of Power Sources, 171*(2), 558-566. doi: 10.1016/j.jpowsour.2007.07.004

Shao, Y., Yin, G., Zhang, J., & Gao, Y. (2006). Comparative Investigation of the Resistance to Electrochemical Oxidation of Carbon Black and Carbon Nanotubes in Aqueous Sulfuric Acid Solution. *Electrochimica Acta, 51*(26), 5853-5857. doi: 10.1016/j.electacta.2006.03.021

Shen, P. K. (2008). PEM Fuel Cell Catalyst Layers and MEAs. In J. Zhang (Ed.), *PEM Fuel Cell Electrocatalysts and Catalyst Layers* (pp. 355-380): Springer London.

Sheng, W., Chen, S., Vescovo, E., & Shao-Horn, Y. (2011). Size Influence on the Oxygen Reduction Reaction Activity and Instability of Supported Pt Nanoparticles. *Journal of The Electrochemical Society, 159*(2), B96-B103. doi: 10.1149/2.009202jes

Shevchenko, E. V., Kortright, J., Talapin, D. V., Aloni, S., & Alivisatos, A. P. (2007). Quasi-ternary Nanoparticle Superlattices Through Nanoparticle Design. *Advanced Materials, 19*(23), 4183-4188. doi: 10.1002/adma.200701470

Skoog, D. A., Holler, F. J., & Crouch, S. R. (2007). *Principles of Instrumental Analysis*: Thomson Brooks/Cole.

Smith, J. N., Meadows, J., & Williams, P. A. (1996). Adsorption of Polyvinylpyrrolidone onto Polystyrene Latices and the Effect on Colloid Stability. *Langmuir, 12*(16), 3773-3778. doi: 10.1021/la950933m

Song, C., & Zhang, J. (2008). Electrocatalytic Oxygen Reduction Reaction. In J. Zhang (Ed.), *PEM Fuel Cell Electrocatalysts and Catalyst Layers* (pp. 89-134): Springer London.

Song, T., Jeon, Y., Samal, M., Han, H., Park, H., Ha, J., . . . Paik, U. (2012). A Ge Inverse Opal with Porous Walls as an Anode for Lithium Ion Batteries. *Energy Environ. Sci., 5*, 9028-9033. doi: 10.1039/c2ee22358a

Song, Y.-J., Oh, J.-K., & Park, K.-W. (2008). Pt Nanostructure Electrodes Pulse Electrodeposited in PVP for Electrochemical Power Sources. *Nanotechnology, 19*, 6. doi: 10.1088/0957-4484/19/35/355602

Song, Y.-Y., Zhang, D., Gao, W., & Xia, X.-H. (2005). Nonenzymatic Glucose Detection by Using a Three-Dimensionally Ordered, Macroporous Platinum Template. *Chem.--Eur. J., 11*, 2177-2182. doi: 10.1002/chem.200400981

Srinivasan, S., Manko, D. J., Koch, H., Enayetullah, M. A., & Appleby, A. J. (1990). Recent Advances in Solid Polymer Electrolyte Fuel Cell Technology with Low Platinum Loading Electrodes. *Journal of Power Sources, 29*(3–4), 367-387. doi: 10.1016/0378-7753(90)85011-Z

Stamenkovic, V., Mun, B. S., Mayrhofer, K. J. J., Ross, P. N., Markovic, N. M., Rossmeisl, J., . . . Nørskov, J. K. (2006). Changing the Activity of Electrocatalysts for Oxygen Reduction by Tuning the Surface Electronic Structure. *Angewandte Chemie International Edition, 45*(18), 2897-2901. doi: 10.1002/anie.200504386

Stamenkovic, V. R., Mun, B. S., Mayrhofer, K. J. J., Ross, P. N., & Markovic, N. M. (2006). Effect of Surface Composition on Electronic Structure, Stability, and Electrocatalytic Properties of Pt-Transition Metal Alloys: Pt-Skin versus Pt-Skeleton Surfaces. *Journal of the American Chemical Society, 128*(27), 8813-8819. doi: 10.1021/ja0600476

Steele, B. C. H., & Heinzel, A. (2001). Materials for Fuel-Cell Technologies. *Nature, 414*(6861), 345. doi: 10.1038/35104620

Stevens, D. A., Hicks, M. T., Haugen, G. M., & Dahn, J. R. (2005). Ex Situ and In Situ Stability Studies of PEMFC Catalysts: Effect of Carbon Type and Humidification on Degradation of the Carbon. *Journal of The Electrochemical Society, 152*(12), A2309-A2315. doi: 10.1149/1.2097361

Sun, S., Murray, C. B., Weller, D., Folks, L., & Moser, A. (2000). Monodisperse FePt Nanoparticles and Ferromagnetic FePt Nanocrystal Superlattices. *Science, 287*(5460), 1989-1992. doi: 10.1126/science.287.5460.1989

Sun, S., Zeng, H., Robinson, D. B., Raoux, S., Rice, P. M., Wang, S. X., & Li, G. (2003). Monodisperse MFe_2O_4 (M = Fe, Co, Mn) Nanoparticles. *Journal of the American Chemical Society, 126*(1), 273-279. doi: 10.1021/ja0380852

Sun, Y., Lu, J., & Zhuang, L. (2010). Rational Determination of Exchange Current Density for Hydrogen Electrode Reactions at Carbon-Supported Pt Catalysts. *Electrochimica Acta, 55*(3), 844-850. doi: 10.1016/j.electacta.2009.09.047

Suntivich, J., Xu, Z., Carlton, C. E., Kim, J., Han, B., Lee, S. W., . . . Shao-Horn, Y. (2013). Surface Composition Tuning of Au–Pt Bimetallic Nanoparticles for

Enhanced Carbon Monoxide and Methanol Electro-oxidation. *Journal of the American Chemical Society, 135*(21), 7985-7991. doi: 10.1021/ja402072r

Teranishi, T., Hosoe, M., Tanaka, T., & Miyake, M. (1999). Size Control of Monodispersed Pt Nanoparticles and Their 2D Organization by Electrophoretic Deposition. *The Journal of Physical Chemistry B, 103*(19), 3818-3827. doi: 10.1021/jp983478m

Thomas, S. C., Ren, X., Gottesfeld, S., & Zelenay, P. (2002). Direct Methanol Fuel Cells: Progress in Cell Performance and Cathode Research. *Electrochimica Acta, 47*(22–23), 3741-3748. doi: 10.1016/S0013-4686(02)00344-4

Topalov, A. A., Cherevko, S., Zeradjanin, A. R., Meier, J. C., Katsounaros, I., & Mayrhofer, K. J. J. (2014). Towards a Comprehensive Understanding of Platinum Dissolution in Acidic Media. *Chemical Science, 5*(2), 631-638. doi: 10.1039/c3sc52411f

Topalov, A. A., Katsounaros, I., Auinger, M., Cherevko, S., Meier, J. C., Klemm, S. O., & Mayrhofer, K. J. J. (2012). Dissolution of Platinum: Limits for the Deployment of Electrochemical Energy Conversion? *Angewandte Chemie International Edition, 51*(50), 12613-12615. doi: 10.1002/anie.201207256

Tremiliosi-Filho, G., Dall'Antonia, L. H., & Jerkiewicz, G. (2005). Growth of Surface Oxides on Gold Electrodes Under Well-Defined Potential, Time and Temperature Conditions. *Journal of Electroanalytical Chemistry, 578*(1), 1-8. doi: 10.1016/j.jelechem.2004.12.007

Tremiliosi-Filho, G., Jerkiewicz, G., & Conway, B. E. (1992). Characterization and Significance of the Sequence of Stages of Oxide Film Formation at Platinum Generated by Strong Anodic Polarization. *Langmuir, 8*(2), 658-667. doi: 10.1021/la00038a059

Ung, D., Tung, L. D., Caruntu, G., Delaportas, D., Alexandrou, I., Prior, I. A., & Thanh, N. T. K. (2009). Variant Shape Growth of Nanoparticles of Metallic Fe-Pt, Fe-Pd and Fe-Pt-Pd alloys. *CrystEngComm, 11*(7), 1309-1316. doi: 10.1039/b823290n

Urchaga, P., Baranton, S., Coutanceau, C., & Jerkiewicz, G. (2011). Electro-oxidation of COchem on Pt Nanosurfaces: Solution of the Peak Multiplicity Puzzle. *Langmuir, 28*(7), 3658-3663. doi: 10.1021/la202913b

Venkateswara Rao, C., Cabrera, C. R., & Ishikawa, Y. (2011). Graphene-Supported Pt–Au Alloy Nanoparticles: A Highly Efficient Anode for Direct Formic Acid Fuel Cells. *The Journal of Physical Chemistry C, 115*(44), 21963-21970. doi: 10.1021/jp202561n

Vidal-Iglesias, F. J., Solla-Gullón, J., Montiel, V., & Aldaz, A. (2012). Errors in the Use of the Koutecky–Levich Plots. *Electrochemistry Communications, 15*(1), 42-45. doi: 10.1016/j.elecom.2011.11.017

Vojislav, R. S., Bongjin Simon, M., Matthias, A., Karl, J. J. M., Christopher, A. L., Guofeng, W., . . . Nenad, M. M. (2007). Trends in Electrocatalysis on Extended and Nanoscale Pt-Bimetallic Alloy Surfaces. *Nature Materials, 6*(3), 241-247. doi: 10.1038/nmat1840

Wagner, F. T., Lakshmanan, B., & Mathias, M. F. (2010). Electrochemistry and the Future of the Automobile. *The Journal of Physical Chemistry Letters, 1*(14), 2204-2219. doi: 10.1021/jz100553m

Wang, C., Daimon, H., Onodera, T., Koda, T., & Sun, S. (2008). A General Approach to the Size- and Shape-Controlled Synthesis of Platinum Nanoparticles and Their Catalytic Reduction of Oxygen. *Angewandte Chemie International Edition, 47*(19), 3588-3591. doi: 10.1002/anie.200800073

Wang, J., Yin, G., Wang, G., Wang, Z., & Gao, Y. (2008). A Novel Pt/Au/C Cathode Catalyst for Direct Methanol Fuel Cells with Simultaneous Methanol Tolerance and Oxygen Promotion. *Electrochemistry Communications, 10*(6), 831-834. doi: 10.1016/j.elecom.2008.03.009

Wang, J. X., Inada, H., Wu, L., Zhu, Y., Choi, Y., Liu, P., . . . Adzic, R. R. (2009). Oxygen Reduction on Well-Defined Core−Shell Nanocatalysts: Particle Size, Facet, and Pt Shell Thickness Effects. *Journal of the American Chemical Society, 131*(47), 17298-17302. doi: 10.1021/ja9067645

Wang, X. D., Graugnard, E., King, J. S., Wang, Z. L., & Summers, C. J. (2004). Large-Scale Fabrication of Ordered Nanobowl Arrays. *Nano Letters, 4*(11), 2223-2226. doi: 10.1021/nl048589d

Wang, Y.-J., Wilkinson, D. P., & Zhang, J. (2011). Noncarbon Support Materials for Polymer Electrolyte Membrane Fuel Cell Electrocatalysts. *Chemical Reviews, 111*(12), 7625-7651. doi: 10.1021/cr100060r

Wang, Y., Chen, X., Zhang, J., Sun, Z., Li, Y., Zhang, K., & Yang, B. (2008). Fabrication of Surface-Patterned and Free-Standing ZnO Nanobowls. *Colloids and Surfaces A: Physicochemical and Engineering Aspects, 329*(3), 184-189. doi: 10.1016/j.colsurfa.2008.07.018

Watt-Smith, M. J., Friedrich, J. M., Rigby, S. P., Ralph, T. R., & Walsh, F. C. (2008). Determination of the Electrochemically Active Surface Area of Pt/C PEM Fuel Cell Electrodes Using Different Adsorbates. *Journal of Physics D: Applied Physics, 41*(17), 174004. doi: 10.1088/0022-3727/41/17/174004

Watt, I. M. (1997). *The Principles and Practice of Electron Microscopy*: Cambridge University Press.

Williams, D., & Carter, C. B. (2009). The Transmission Electron Microscope *Transmission Electron Microscopy* (pp. 3-22): Springer US.

Woods, R. (1974). Hydrogen Adsorption on Platinum, Iridium and Rhodium Electrodes at Reduced Temperatures and the Determination of Real Surface Area. *Journal of Electroanalytical Chemistry and Interfacial Electrochemistry, 49*(2), 217-226. doi: 10.1016/S0022-0728(74)80229-9

Xia, Y., Gates, B., Yin, Y., & Lu, Y. (2000). Monodispersed Colloidal Spheres: Old Materials with New Applications. *Advanced Materials, 12*(10), 693-713. doi: 10.1002/(sici)1521-4095(200005)12

Xiong, Y., Chen, J., Wiley, B., Xia, Y., Aloni, S., & Yin, Y. (2005). Understanding the Role of Oxidative Etching in the Polyol Synthesis of Pd Nanoparticles with Uniform Shape and Size. *Journal of the American Chemical Society, 127*(20), 7332-7333. doi: 10.1021/ja0513741

Xu, C., Wang, R., Chen, M., Zhang, Y., & Ding, Y. (2010). Dealloying to Nanoporous Au/Pt Alloys and their Structure Sensitive Electrocatalytic Properties. *Physical Chemistry Chemical Physics, 12*(1), 239-246. doi: 10.1039/b917788d

Xu, M., Lu, N., Xu, H., Qi, D., Wang, Y., & Chi, L. (2009). Fabrication of Functional Silver Nanobowl Arrays via Sphere Lithography. *Langmuir, 25*(19), 11216-11220. doi: 10.1021/la902196t

Yamamoto, K., Kolb, D. M., Kötz, R., & Lehmpfuhl, G. (1979). Hydrogen Adsorption and Oxide Formation on Platinum Single Crystal Electrodes. *Journal of Electroanalytical Chemistry and Interfacial Electrochemistry, 96*(2), 233-239. doi: 10.1016/S0022-0728(79)80380-0

Yan, S., & Zhang, S. (2012). Methanol Electrooxidation on Carbon Supported Au core – Pt shell Nanoparticles Synthesized by an Epitaxial Growth Method. *International Journal of Hydrogen Energy, 37*(12), 9636-9644. doi: 10.1016/j.ijhydene.2012.03.058

Yang, J., Chen, X., Yang, X., & Ying, J. Y. (2012). Stabilization and Compressive Strain Effect of AuCu Core on Pt Shell for Oxygen Reduction Reaction. *Energy & Environmental Science, 5*(10), 8976-8981. doi: 10.1039/c2ee22172a

Yang, M., Qu, F., Lu, Y., He, Y., Shen, G., & Yu, R. (2006). Platinum Nanowire Nanoelectrode Array for the Fabrication of Biosensors. *Biomaterials, 27*, 5944-5950. doi: 10.1016/j.biomaterials.2006.08.014

Yang, S., & Gao, L. (2006). Controlled Synthesis and Self-Assembly of CeO_2 Nanocubes. *J. Am. Chem. Soc., 128*, 9330-9331. doi: 10.1021/ja063359h

Ye, J., Van Dorpe, P., Van Roy, W., Borghs, G., & Maes, G. (2009). Fabrication, Characterization, and Optical Properties of Gold Nanobowl Submonolayer Structures. *Langmuir, 25*(3), 1822-1827. doi: 10.1021/la803768y

Yoon, M., Choi, J., & Cho, J. (2013). Multifunctional Colloids with Reversible Phase Transfer between Organic and Aqueous Media via Layer-by-Layer Assembly. *Chemistry of Materials, 25*(9), 1735-1743. doi: 10.1021/cm400207d

Yuan, X.-Z., & Wang, H. (2008). PEM Fuel Cell Fundamentals. In J. Zhang (Ed.), *PEM Fuel Cell Electrocatalysts and Catalyst Layers* (pp. 1-87): Springer London.

Zalitis, C. M., Kramer, D., & Kucernak, A. R. (2013). Electrocatalytic Performance of Fuel Cell Reactions at Low Catalyst Loading and High Mass Transport. [10.1039/C3CP44431G]. *Physical Chemistry Chemical Physics, 15*(12), 4329-4340. doi: 10.1039/c3cp44431g

Zellner, M. B., & Chen, J. G. (2005). Surface Science and Electrochemical Studies of WC and W_2C PVD Films as Potential Electrocatalysts. *Catalysis Today, 99*(3–4), 299-307. doi: 10.1016/j.cattod.2004.10.004

Zhang, H., Wang, X., Zhang, J., & Zhang, J. (2008). Conventional Catalyst Ink, Catalyst Layer and MEA Preparation. In J. Zhang (Ed.), *PEM Fuel Cell Electrocatalysts and Catalyst Layers* (pp. 889-916): Springer London.

Zhang, J., Ge, X., Wang, M., Yang, J., Wu, Q., Wu, M., & Xu, D. (2011). Colloidal Silver Deposition onto Functionalized Polystyrene Microspheres. *Polymer Chemistry, 2*(4), 970-974. doi: 10.1039/c0py00320d

Zhang, J., Jin, Y., Li, C., Shen, Y., Han, L., Hu, Z., . . . Liu, Z. (2009). Creation of Three-Dimensionally Ordered Macroporous Au/CeO_2 Catalysts with Controlled Pore Sizes and their Enhanced Catalytic Performance for Formaldehyde Oxidation. *Applied Catalysis B: Environmental, 91*(1–2), 11-20. doi: 10.1016/j.apcatb.2009.05.001

Zhang, J., Ma, H., Zhang, D., Liu, P., Tian, F., & Ding, Y. (2008). Electrocatalytic Activity of Bimetallic Platinum-Gold Catalysts Fabricated Based on Nanoporous Gold. *Physical Chemistry Chemical Physics, 10*(22), 3250-3255. doi: 10.1039/b718192b

Zhang, J., Sasaki, K., Sutter, E., & Adzic, R. R. (2007). Stabilization of Platinum Oxygen-Reduction Electrocatalysts Using Gold Clusters. *Science, 315*(5809), 220-222. doi: 10.1126/science.1134569

Zhang, M., Ngo, T. H., Rabiah, N. I., Otanicar, T. P., Phelan, P. E., Swaminathan, R., & Dai, L. L. (2013). Core–Shell and Asymmetric Polystyrene–Gold Composite Particles via One-Step Pickering Emulsion Polymerization. *Langmuir, 30*(1), 75-82. doi: 10.1021/la4041166

Zhang, Q., Yue, R., Jiang, F., Wang, H., Zhai, C., Yang, P., & Du, Y. (2013). Au as an Efficient Promoter for Electrocatalytic Oxidation of Formic Acid and Carbon Monoxide: a Comparison Between Pt-on-Au and PtAu Alloy Catalysts. *Gold Bulletin, 46*(3), 175-184. doi: 10.1007/s13404-013-0098-5

Zhao, D., & Xu, B.-Q. (2006). Enhancement of Pt Utilization in Electrocatalysts by Using Gold Nanoparticles. *Angewandte Chemie International Edition, 45*(30), 4955-4959. doi: 10.1002/anie.200600155

Zhou, W. P., Lewera, A., Larsen, R., Masel, R. I., Bagus, P. S., & Wieckowski, A. (2006). Size Effects in Electronic and Catalytic Properties of Unsupported Palladium Nanoparticles in Electrooxidation of Formic Acid. *J. Phys. Chem. B, 110*, 13393-13398. doi: 10.1021/jp061690h

Appendix A.

Assembly of Polystyrene Spheres

Other Methods Explored

Before employing the method described in this thesis for the assembly of bare and nanoparticle coated PS spheres, several other methods were explored. These included spin-casting and Langmuir-Blodgett assembly, among others. A method was sought, whereby a single layer of assembled spheres could be prepared on a substrate of interest and built upon with subsequent preparation of assembled spheres on top of the original layer to create multi-layer assemblies. Spin casting was well documented in literature for the assembly of PS spheres.(Cheung, Nikolić, Reinhardt, & Wang, 2006) This method though was not found to be useful for electrode preparation here, since assembly was generally limited to bare, single crystalline polished Si wafer substrates. Altering the surface energy and/or roughness of the Si wafer substrate (e.g., with a gold coating) or using any other substrate (e.g., highly ordered pyrolytic graphite) resulted in a low quality of assembly. Langmuir-Blodgett method was not known in literature for the assembly of PS spheres. With much effort, some decent quality single layer assemblies were formed. The method though was not reproducible and required a large volume of PS spheres for each assembly. This lack of reproducibility is now believed to be the result of a loss of PS spheres from the air-water interface (to the water sub-phase) upon pressure from the barriers of the Langmuir-Blodgett trough.

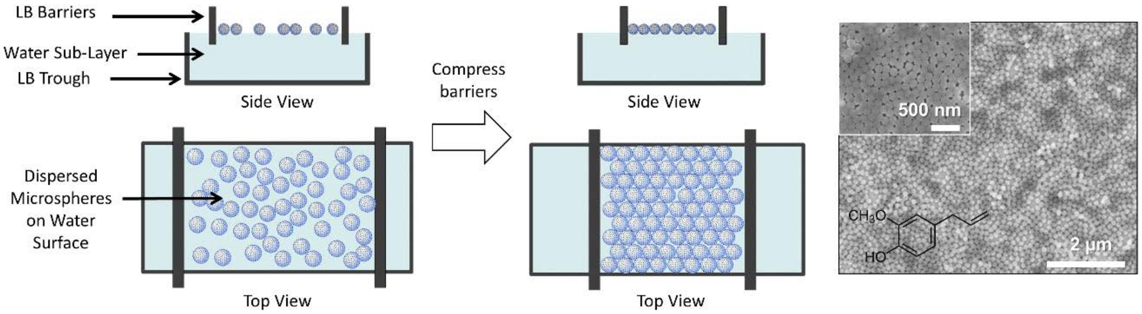

Figure A1. Schematic of a Langmuir-Blodgett (LB) assembly of PS spheres and a correponding SEM image of one resulting assembly. This assembly was prepared from an ~ 1 wt % dispersion of Pt NP decorated 180 nm diameter PS spheres in 1-BuOH and eugenol (~ 5 vol %, structure shown in inset).

Notes on the Air-Water Assembly Method Used

The air-water assembly method used in this thesis work for the assembly of bare and NP coated 500 nm diameter PS spheres is adapted from work reported by Sung et al.(Moon, et al., 2011) The main adaptation made to their method was the heating of the water sub-phase prior to dispersion of the PS spheres at the air-water interface. The procedure for the air-water assembly technique used here is as follows:

i) Bare or nanoparticle coated PS spheres were washed by centrifugation as per procedures in main text and dried in a vacuum desiccator until no solvent was visibly present. The PS spheres or PS@NPs were then dispersed in 1-BuOH at 1 wt% (based on the initial concentration of the PS spheres used, e.g.,, 2 wt% PS spheres, as specified by the manufacturer, were dilute one time in BuOH) with the assistance of sonication.

ii) The water bath was heated to 55°C on a hot plate without stirring (surface temperature was verified with an IR thermometer). Prior to filling with demineralized water, the Pyrex crystallizing dish was washed with soap and water and rinsed with acetone and demineralized water. The size of Pyrex crystallizing dish should be chosen to be just slightly larger than the substrate of interest to enable more efficient transfer of the assembly to the substrate (e.g., better coverage and less cracks).

iii) The warm water bath was removed from heat and placed onto a dark surface (this enables better viewing of the assembled spheres on the water surface). The 1-BuOH dispersions of the PS spheres were cast onto the warm water surface by gently transferring drops from a pipette to the air-water interface until the interface was filled. Filling of the air-water interface was indicated by aggregation of the PS spheres upon addition of a drop (as opposed to dispersion across the air-water interface).

iv) The water bath was then allowed to cool to <30°C and the assembly transferred from the air-water interface to the substrate of interest. In brief, the substrate was rinsed with ethanol and dipped into the water sub-phase. The substrate should have a small amount of residual ethanol on the surface to allow for clean passage into the water sub-phase (e.g., no deposition of PS spheres onto the substrate). The substrate was carefully removed from the water sub-phase through the PS sphere assembly with a scooping motion. The substrate is held at an ~45° angle (to the water surface) upon vertical exit of the sub-phase until the PS spheres begin to transfer to the substrate. The substrate is then tilted to be more parallel with the water surface (~35°) and removed vertically from the sub-phase.

v) After transfer from the air-water interface, the PS sphere assemblies were dried in a vacuum desiccator. After complete drying (e.g., no solvent visible), the assemblies could be rinsed with ethanol and used to transfer a second assembly of PS spheres from the air-water interface. This process can be repeated until the desired number of layers of assemblies have been transferred.

It is also worth noting here that PS@NPs assembled better (more close-packed) than the same spheres without NP coating. This was visible under SEM and upon visual inspection. The bare PS sphere assemblies displayed some opalescence with a color range of yellow to orange. The PS@NPs assemblies displayed more opalescence, with colors ranging from purple to green to orange. This improved assembly of PS@NPs is believed to be a result of the change in the electrostatic properties of the PS spheres due to the presence of NPs on the surface, though this has not been explicitly examined. The presence of PVP on the PS sphere surfaces is likely not the reason for improved packing though. This hypothesis was tested by incorporating PVP into the assembly process of bare PS spheres (e.g., preparing PS spheres with a coating of PVP in the same way PS@NPs were prepared). The assemblies created with these PS@PVP spheres were of the same quality as those prepared with bare PS spheres. The use of this assembly method in the assembly of 200 nm diameter PS spheres was also sought. It was found that the addition of HCl to the BuOH dispersion was required in order to keep the 200 nm diameter PS spheres at the surface, but no high quality assemblies were ever achieved (note that NaCl, as employed by Moon et al., did not work as an additive to keep these spheres at the water surface).

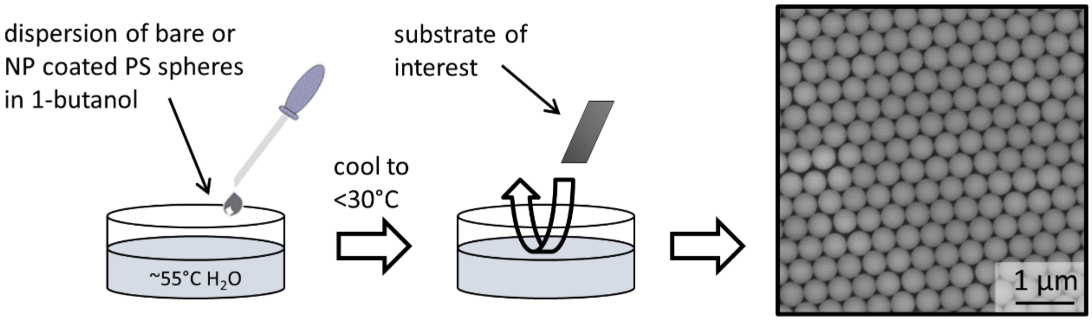

Figure A2. **Schematic of the air-water interface assembly method used in the assembly of bare and NP coated 500 nm diameter PS spheres.**

Appendix B.

Evaluation of Electrochemical Surface Area

Determining Electrochemical Surface Area

The electrochemical or real surface area ($\boldsymbol{A}_{ecsa}$) of an electrode is the surface area of an electrode which is accessible for electrochemical processes. Generally, the $\boldsymbol{A}_{ecsa}$ of an electrode is determined by studying the charged passed upon adsorption or desorption of a species onto the electrode during a cyclic voltammetry experiment. Examples of species that may be adsorbed or desorbed include Cu, CO, or H.(M. Shao, Odell, Choi, & Xia, 2013; Watt-Smith, Friedrich, Rigby, Ralph, & Walsh, 2008) The charge passed during adsorption or desorption (q_{ad}) is calculated as per Eq. 1 below. Experimentally, this is the area under the adsorption/desorption peak multiplied by the scan rate for a cyclic voltammetry scan. This value is then divided by the known amount of charge passed for a monolayer of adsorbed species (upon adsorption or desorption) per area squared (q_m) to determine $\boldsymbol{A}_{ecsa}$, as per Eq. 2.(Watt-Smith, et al., 2008)

$$q = \int I \, dt \tag{1}$$

$$\boldsymbol{A_{ecsa}} = \frac{\boldsymbol{q_{ad}}}{\boldsymbol{q_m}} \tag{2}$$

Platinum Electrochemical Surface Area

The electrochemical surface area of Pt can be calculated with good accuracy from studying the adsorption and desorption of H_{upd}. Adsorption of H_{upd} is limited to 1 monolayer thickness and the charge passed during adsorption and desorption of a monolayer of H_{upd} for polycrystalline Pt in sulfuric acid based electrolyte is established as 210 µC per cm^{-2}. Carbon monoxide stripping and Cu_{upd} are also commonly used. More information on determining the $\boldsymbol{A}_{ecsa}$ of Pt electrodes can be found in the introduction chapter (Section 1.3.3). (D. Chen, et al., 2011; Watt-Smith, et al., 2008)

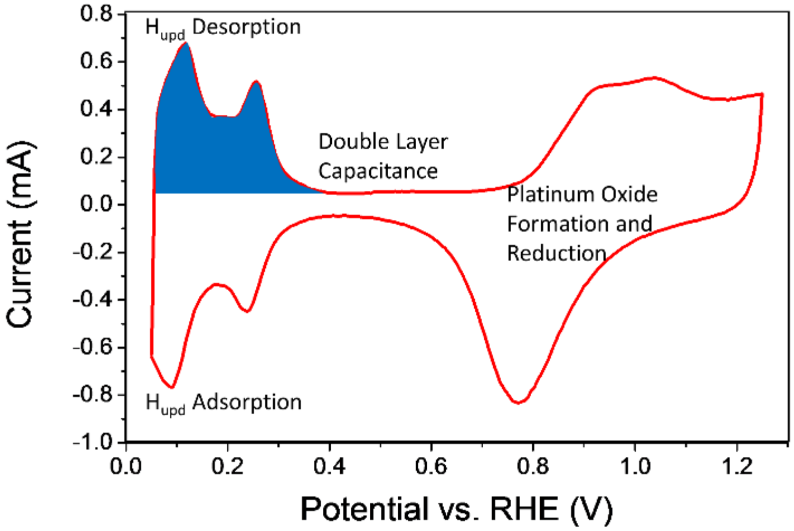

Figure B1. **Cyclic voltammetry scan of a Pt electrode with region highlighted for calculating q_{ad} of H_{upd} for determination of $A_{ecsa,Pt}$. Note that the adsorption peak could also be studied.**

Gold Electrochemical Surface Area

The electrochemical surface area of Au can be calculated from studying the charge passed upon reduction of Au oxide. The formation of Au oxide is not limited to monolayer coverage and so the q_m value is dependent on scan rate, upper potential and temperature during the CV experiment.(Tremiliosi-Filho, et al., 2005) These factors influence the amount of Au oxide that is formed/reduced. This variance in the amount of Au oxide formed/reduced introduces some error into the A_{ecsa} determination. Since the focus of this work was primarily on Pt, this error was not deemed to be of concern. When cycling to 1.8 V at a scan rate of $50 mVs^{-1}$ at room temperature, as was done in this work, the q_m value is reported to be 750 ± 30 µC per cm^2.(Rouya, et al., 2012; Tremiliosi-Filho, et al., 2005) This value reflects that ~ 2 monolayers of Au oxide is formed upon cycling to 1.8 V vs. RHE at 50 mVs^{-1} in 0.5 M H_2SO_4, as reflected in the q_{ox} value.(Rouya, et al., 2012; Tremiliosi-Filho, et al., 2005) Methods typically used for Pt electrodes, such as CO stripping or H_{upd} adsorption are not applicable to Au electrodes because of the different interfacial properties of Au, which does not allow for the use of these adsorbate species. Cu_{upd} can be used for Au A_{ecsa} determination, but was not sought here.(Rouya, et al., 2012)

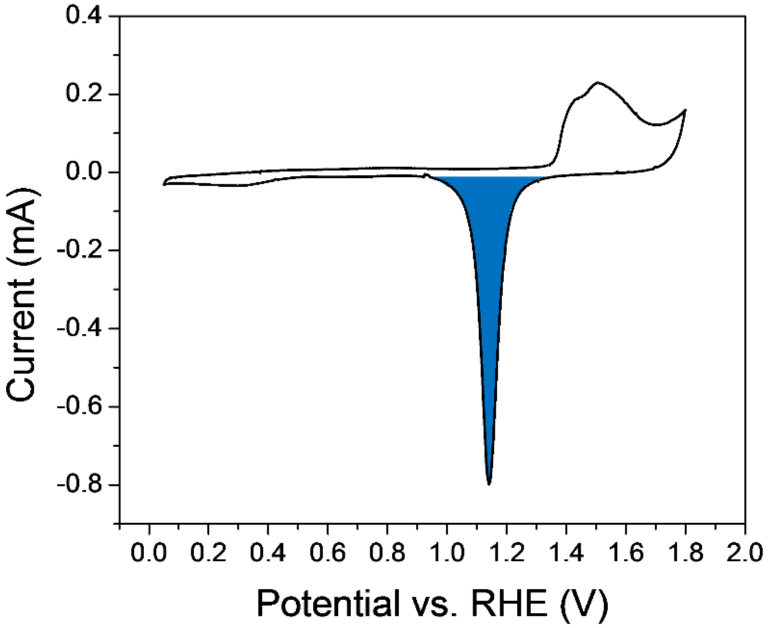

Figure B2. Cyclic voltammetry scan of a Au electrode with region highlighted for calculating q_{ad} of Au oxide (reduction) for determination of $A_{ecsa,Au}$. Note that only the reduction and not the formation peak is used.

Appendix C.

Additional Data for Chapter 3

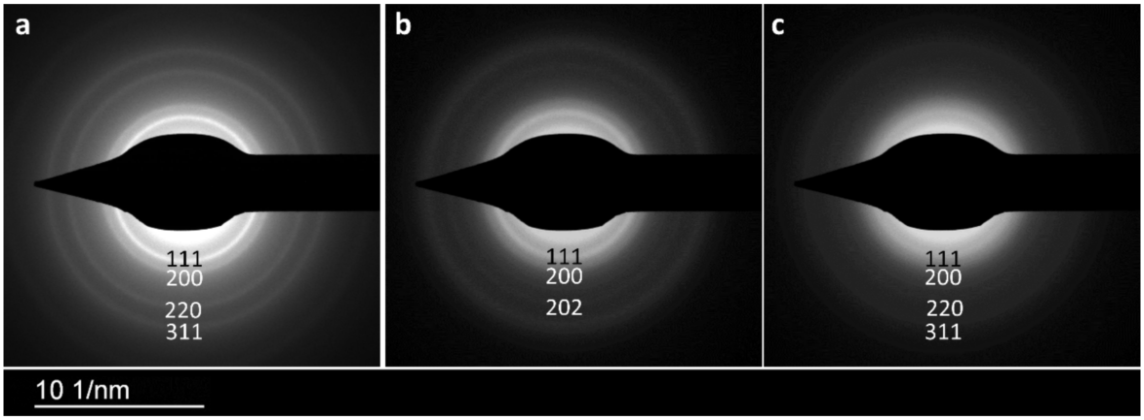

Figure C1. **Selected area electron diffraction patterns for: a) palladium, b) FePt alloy, and c) platinum NPs (scale bar below images). The d-spacing value for the FePt (111) plane is similar to that reported in literature for small FePt alloys NPs, suggesting that the FePt is an alloy although the NPs are not suspected to be single crystalline.(S. Sun, et al., 2000)**

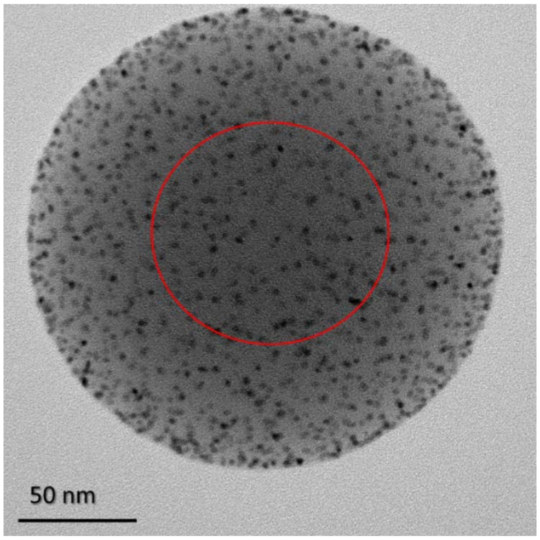

Figure C2. **TEM image of a Pt NP coated PS sphere with red circle indicating the central and outer region distinguished for quantification of NPs in shell.**

Appendix D.

Additional Data for Chapter 4

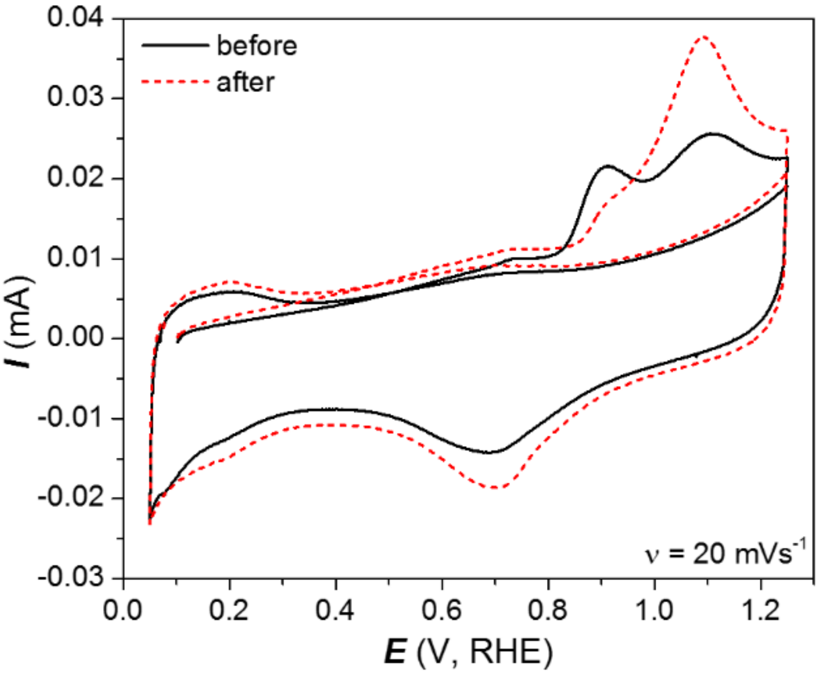

Figure D1. **CO oxidative stripping voltammetry profiles acquired before and after the electrochemical stability test by CV in 0.5 M H_2SO_4 after adsorption of CO onto the Pt surfaces.**

Table D1. **Optimal ICP-MS operating conditions for the analysis of Au@PtNP-OP samples.**

Operating Parameter	Value
Ar Plasma Coolant Flow Rate (L/min)	18.0
Ar Auxiliary Flow Rate (L/min)	1.8
Ar Nebulizer Flow Rate (L/min)	1.0
Ar Sheath Flow Rate (L/min)	0.02
R.F. Power (kW)	1.50
Sample Uptake Rate (μL/min)	300

Appendix E.

Additional Data for Chapter 5

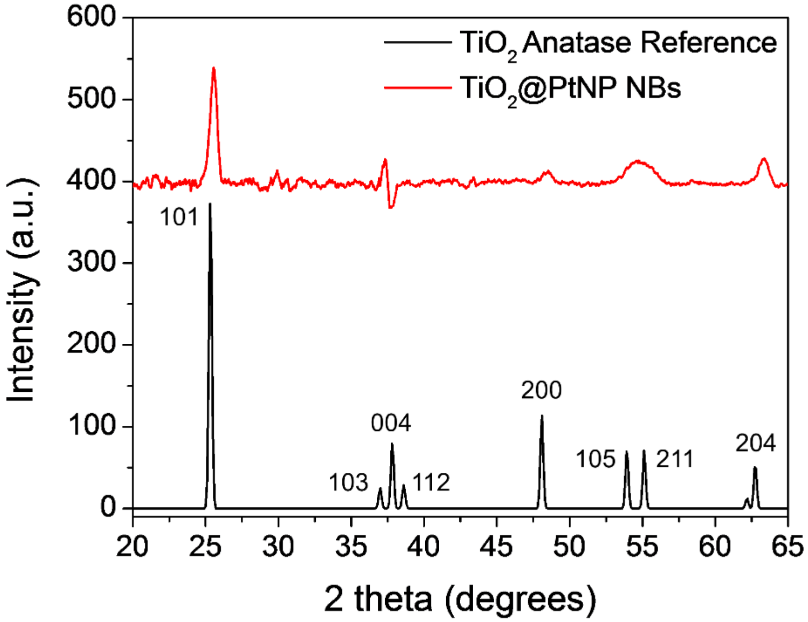

Figure E1. **X-ray diffraction pattern obtained for the TiO_2@PtNP NBs (background subtracted) after annealing at 450°C and anatase TiO_2 reference pattern (PDF 01-071-1166 21-1272). Note that overlap with the background diffraction pattern in the region between 35 and 40 degrees resulted in a high level of noise for this region. This overlap also makes the 103, 004 and 112 peaks for TiO_2 not visible in the XRD pattern of the TiO_2@PtNP NBs.**

The TiO_2@PtNP NB XRD sample was prepared by dispersing annealed NBs in EtOH (NBs removed from GC substrate by sonication in EtOH after annealing) and drop casting onto a glass cover slip. The background signal arose from the glass cover slip, as well as the underlying double-sided tape used to affix the sample to the XRD sample holder.

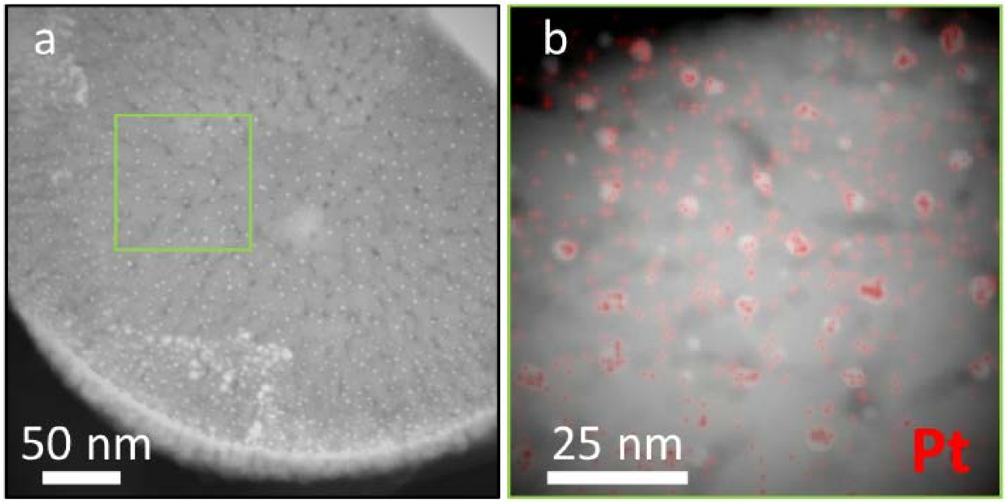

Figure E2. (a) Scanning TEM image and (b) elemental map of Pt (overlayed on the HAADF STEM image) aquired by EDS of a TiO_2@PtNP NB after annealing. The green box in (a) outlines the region over which the elemental map in (b) was aquired.

Appendix F.

List of Publications and Presentations

Peer-Reviewed Publications (during Ph.D. studies):

1. B. K. Pilapil, J. van Drunen, Y. Makonnen, D. Beauchemin, G. Jerkiewicz and B. D. Gates, “Platinum nanoparticle functionalized ultrathin ordered porous gold electrocatalysts: Towards highly effective platinum utilization in electrocatalysis”, Submitted.
2. A. W. Lee, B. K. Pilapil, H.-W. Ing and B. D. Gates “Microwave assisted formation of monoreactive perfluoroalkylsilane-based self-assembled monolayers”, Submitted.
3. B. K. Pilapil, M. C. P. Wang, M. T. Y. Paul, A. Nazemi and B. D. Gates, “Self-assembly of nanoparticles onto the surfaces of polystyrene spheres with a tunable composition and loading” Nanotechnology, Accepted (NANO-105201.R1)
4. J. van Drunen, B. K. Pilapil, Y. Makonnen, D. Beauchemin, B. D. Gates and G. Jerkiewicz, “Electrochemically active nickel foams as support materials for nanoscopic platinum electrocatalysts”, ACS Applied Materials and Interfaces, 6 (15), 12046-12061 (2014)
5. Iris I. Guo. I. Pekcevik, B. K. Pilapil, M. C. P. Wang, B. D. Gates, “Colloidal core-shell materials with spiky surfaces assembled from gold nanorods”, Chem. Commun., 50, 8157-8160 (2014)
6. M. Paul, B. Kinkead, and B. D. Gates, "Ordered porous gold electrodes to enhance the sensitivity of enzyme-based glucose sensors", Journal of The Electrochemical Society, 161 (2) B3103-B3106 (2014)
7. B. Kinkead, J. van Drunen, M. Paul, K. Dowling, G. Jerkiewicz, and B. D. Gates, “Platinum ordered porous electrodes: Developing a platform for fundamental electrochemical characterization”, Electrocatalysis 4 (3), 179-186 (2013)
8. J. van Drunen, B. Kinkead, M. C. P. Wang, B. D. Gates and G. Jerkiewicz, “Comprehensive structural, chemical and electrochemical properties of nickel-based metallic foams”, ACS Applied Materials and Interfaces 5 (14), 6712-6722 (2013)
9. B. Kinkead, A. Ali, J. C. Boyer and B. D. Gates, “Optically active nanoparticle coated polystyrene spheres”, Mater. Res. Soc. Symp. Proc., 1546, 6 pages (2013)

Select Presentations (during Ph.D. studies):

1. B. K. Pilapil, A. W. Lee and B. D. Gates, “Preparation and characterization of support@nanoparticle electrocatalytic nanobowls”, International Symposium on Electrocatalysis 2014, Whistler, BC (2014) Oral Presentation.
2. B. K. Pilapil, J. van Drunen, M. T. Y. Paul, Y. Makonnen, D. Beauchemin, G. Jerkiewicz and B. D. Gates, “Ordered porous electrocatalysts towards highly effective platinum utilization”, 97th Canadian Chemistry Conference and Exhibition, Vancouver, BC (2014) Oral Presentation.
3. B. Kinkead, and B. D. Gates, “Exploration of the electrocatalytic properties of platinum nanoparticle functionalized ordered porous gold electrodes”, 247th ACS National Meeting, Dallas, TX (2014) Oral Presentation.

4. B. Kinkead, A. A. Ali, Iris I Guo, J.-C. Boyer and B. D. Gates, “Multi-functional nanoparticle coatings on polystyrene spheres by design: Preparation and application to catalysis and sensing”, 247th ACS National Meeting, Dallas, TX (2014) Oral Presentation.
5. B. Kinkead J. van Drunen, M. T. Y. Paul, G. Jerkiewicz and B. D. Gates, “Ultrathin ordered porous platinum electrodes for electrocatalytic oxygen reduction and methanol oxidation”, 247th ACS National Meeting, Dallas, TX (2014) Oral Presentation.
6. B. Kinkead, I. Guo, A. Ali, J. C. Boyer, A. Nazemi and B. D. Gates, “Multipurpose microspheres with designer coatings of nanoparticles”, 2013 MRS Spring Meeting and Exhibit, San Francisco, CA (2013) Poster Presentation.
7. B. Kinkead, J. van Drunen, M. Paul , A. Nazemi, K. Dowling and B. D. Gates, “Ordered porous nanostructured thin films for ORR electrocatalysis”, 62nd Canadian Chemical Engineering Conference, Vancouver, BC (2012) Oral Presentation, Keynote.
8. B. Kinkead, J. van Drunen, K. Dowling, M. Paul and B. D. Gates, “Ordered porous nanostructured thin films of platinum for ORR electrocatalysis”, 95th Canadian Chemistry Conference and Exhibition, Calgary, AB (2012) Oral Presentation: Energy Futures Symposium.